UNIVERSITY OF CAPE TOWN

MASTERS THESIS

A tri-phasic continuum model for the numerical analysis of biological tissue proliferation using the Theory of Porous Media. Application to cardiac remodelling in rheumatic heart disease

Author:
Adam MOSAM

Supervisor:
Assoc. Prof. Sebastian SKATULLA

A dissertation submitted in fulfilment of the requirements for the degree of Master of Science in Engineering

in the

Computational Continuum Mechanics Research Group
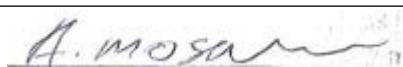Department of Civil Engineering

February 10, 2019

Declaration of Authorship

I, Adam MOSAM, declare that this thesis titled, "A tri-phasic continuum model for the numerical analysis of biological tissue proliferation using the Theory of Porous Media. Application to cardiac remodelling in rheumatic heart disease" and the work presented in it are my own. I confirm that:

- This work was done wholly or mainly while in candidature for a research degree at this University.

- Where any part of this thesis has previously been submitted for a degree or any other qualification at this University or any other institution, this has been clearly stated.

- Where I have consulted the published work of others, this is always clearly attributed.

- Where I have quoted from the work of others, the source is always given. With the exception of such quotations, this thesis is entirely my own work.

- I have acknowledged all main sources of help.

- Where the thesis is based on work done by myself jointly with others, I have made clear exactly what was done by others and what I have contributed myself.

- I know the meaning of plagiarism and declare that all the work in the document, save for that which is properly acknowledged, is my own. This thesis/dissertation has been submitted to the Turnitin module (or equivalent similarity and originality checking software) and I confirm that my supervisor has seen my report and any concerns revealed by such have been resolved with my supervisor.

Name: Adam Mosam (MSMADA002)

Signed:

Date: February 10, 2019

University of Cape Town

Abstract

Engineering and the Built Environment
Department of Civil Engineering

Master of Science in Engineering

A tri-phasic continuum model for the numerical analysis of biological tissue proliferation using the Theory of Porous Media. Application to cardiac remodelling in rheumatic heart disease

by Adam Mosam

This research is part of an on-going project aimed at describing the mechanotransduction of Rheumatic Heart Disease, in order to study and predict long-term effects of new therapeutic concepts to treat inflammatory heart diseases and ultimately, estimate their effectiveness to prevent heart failure. Attention is given to Rheumatic Heart Disease (RHD) - a valvular heart disease. RHD is a condition which is mostly common amongst poorer regions and mainly affects young people, of which claims approximately 250 000 lives per annum. The Theory of Porous Media (TPM) can represent the proliferative growth and remodelling processes related to RHD within a thermodynamically consistent framework and is additionally advantageous with application to biological tissue due to the ability to couple multiple constituents, such as tissue and blood.

The research presented will extend an existing biphasic TPM model for the solid cardiac tissue (solid phase) saturated in a blood and interstitial fluid (liquid phase) [25], to a triphasic model with inclusion of a third nutrient phase. This inclusion is motivated by the reason to constrain the volume of the liquid phase within the system in response to the description of growth, which is modelled through a mass exchange between the solid phase and liquid phase within the biphasic model. Although the nutrient phase acts as a source for growth, the proposed mass supply function used to correlate the deposition of sarcomeres in relation to growth is predominantly mechanically driven and bears no connection to any biochemical constituent, which therefore renders the nutrient phase as a physiologically arbitrary quantity. However, the provision of the nutrient phase is a platform for the inclusion of known constituents which actively contribute towards growth, of which may be explored in future research.

The triphasic model is applied to a full cardiac cycle of a left ventricle model, extracted from magnetic resonance imaging (MRI) scans of patients diagnosed with RHD.

Acknowledgements

Firstly, I would like to express my most sincere gratitude to Allah (SWT), the most gracious and the most merciful.

I would like to acknowledge my supervisor, Assoc. Prof. Sebastian Skatulla, for his great support and patience over the duration of this research project. Furthermore, I am grateful for the opportunities that he has presented to me and other students with a civil engineering background, in terms of being exposed to exciting, progressive and challenging areas of research.

To Prof. Tim Ricken and Prof. Ntobeko Ntusi, for being great sources of knowledge.

To my mother, sister, and the Mosam and Essack families, for always providing me with the support I needed.

I would also like extend my appreciation to all my peers, who became like family over the past few years.

Contents

List of Figures

List of Tables

Chapter 1

Introduction

1.1 Background

Medical advancements within the past century have occurred at a rapid rate. Doctors and medical researchers of today have a wide array of knowledge and tools available at their disposal, whether it be in the form of high precision instruments or computer software. Much of this advancement may be attributed to researchers from other fields, such as mathematics, computer science and engineering. The grandiose complexity of the human body has long fascinated scientists and engineers. This fascination has resulted in the popular growth of multidisciplinary fields in biomedical engineering and computational modelling. The study of the human heart is one such area of research which has become popular in recent times, through its relationship to solid mechanics. As such, computationally modelling the mechanics of the human heart will be of primary focus during this research study.

The progression of computing technology has led to faster, more powerful and robust systems, which are capable of handling the demanding computational requirements of biomechanical modelling. Similarly, with improvement in the domain of microscopic imaging, it is possible to characterize changes in molecular structure of a diseased organ. As a result, mathematical models may be developed to describe these changes and predict how certain conditions might evolve; for example, the description of tissue growth of a diseased heart.

Specifically, it is the field of continuum mechanics which is of significant importance in the domain of biomechanical modelling. Principles of continuum mechanics may be used to gain an improved understanding of biological systems, especially if they are able to take into account the interconnected mechanical, chemical and electrical mechanisms. These analytical models may be coupled with computational methods in order to help describe the mechanical environment through a healthy, injured or diseased state. Consequently, this may lead to advances in therapeutic and diagnostic procedures.

1.2 Problem Statement

Cardiovascular disease is the most prevalent cause of death globally, claiming 40% of all human mortality [62]. Even through significant medical advancement, approximately 25 million people suffer from heart failure, annually [88]. Unlike other types of tissue around the body, cardiac tissue is unique in the sense that it can rarely regenerate after being damaged [2]. Cardiac hypertrophy is a dominant manifestation of cardiovascular disease, and is usually driven through pressure or volume overload of the heart [38]. On the cellular level cardiac hypertrophy stems from a remodelling of the tissue composition and structure, whereas on the global organ level, this results in a dilated or thickened heart [20]. Understanding how changes in the micro properties

of cardiac tissue relate to changes in the heart as a whole, and how the activity of the heart is affected, is of great importance [20].

The Computational Continuum Mechanics (CCM) Research Group in the Department of Civil Engineering have long been involved in computational modelling of the human heart. Specifically, Rheumatic Heart Disease (RHD), a valvular heart disease resulting from rheumatic fever has been the primary focus. Rheumatic fever is a condition which is relatively uncommon within developed urban zones. This may be attributed to improved socio-economic living conditions and the availability of medical treatments and services [45]. However, amongst the developing countries around the world, RHD has become a major burden. The demographic results of RHD are especially alarming, where it is estimated that every year 250 000 deaths occur worldwide, with majority of those affected being young people. Due to the fact that the disease is isolated to poverty stricken and rising nations, little attention has been shed on this matter [45]. As a result, there is a large need for research into the disease in order to develop vaccines, treatments and management schemes. The CCM Research Groups main objective is to create a tool in the form of computational software for medical researchers that may provide certain forms of analysis and insight to patients suffering from the disease.

The CCM has developed an in-house cardiac mechanics software SESKA. Recently, an extension was made to SESKA in order to treat cardiac systems as bi-phasic entities (comprising of fluid and solid masses), as opposed to a classical continuum mechanics framework which assumes the domain to be a fully homogenised solid continua. This was done by implementing a framework based on the Theory of Porous Media (TPM), which is adequate in representing certain phenomena, such as tissue growth and remodelling, which are dominant mechanisms associated with RHD. Additionally, in relation to hard tissue, using a classical continuum mechanics framework is sufficient, however, with respect to soft tissue, a reduction towards single phase systems can be inaccurate and overly simplified due to the significant effect the fluid system has on the overall behaviour [49]. TPM has been utilised in describing soft tissue and multiphase systems in recent times, such as with the study of the liver in the work of Ricken and Bluhm [58]. With respect to modelling RHD infected hearts using TPM as a computational mechanics framework, the investigation is still in its infancy, of which validates the reason for continued research in the field.

1.3 Growth and remodelling proliferation in cardiac systems

The basis for modelling soft tissue and growth and remodelling proliferation, was established through the conception of an incompatible configuration and the multiplicative split of the deformation gradient into elastic and growth parts [47, 60]. This theory was first conceived in the work of Rodriguez et al. [60], whereby an adaptation of the theories employed in the field of finite plasticity, developed by Lee [40], was successfully conducted. Even though growth is still a fairly under represented area of research, there have been great strides made to characterise soft tissue in terms of growth laws, of which are highly dependent on numerous factors such as the type of stimuli (e.g. chemical or mechanical), or the mechanisms of growth evolution (e.g. isotropic or anisotropic growth).

Cardiac modelling is viewed as the benchmark for soft tissue modelling, with much attention being attracted to growth in arteries, with respect to cardiovascular disease, such as with ([24, 36]), and full scale heart modelling [20, 32, 52, 57]. In terms of

growth and remodelling with respect to the heart, two mechanisms of growth are generally modelled for, namely, concentric hypertrophy, which results from a pressure overload, and eccentric hypertrophy, which is stimulated through a volume overload of the heart. These conditions may be found in conjunction with valvular disease, as is the case in people suffering from rheumatic heart. Kerckhoffs et al. [32], developed a growth law which enabled the description of the mechanical and functional changes in hearts with mitral regurgitation and aortic stenosis. Due to a lack of knowledge, the characterisation of cardiac tissue growth in relation to biochemical stimulants, is not well understood. Hence, the studies which have been developed to model growth proliferation are mechanically driven, of which a common example is found in the growth laws formulated to model eccentric and concentric hypertrophy through stress and strain based laws, respectively, proposed by Goktepe et al. [20], and successfully implemented in various studies [57]. In the aforementioned studies, a growth factor, which is a scalar quantity that signifies the degree of growth, is introduced for a given deformation state. The rate of change of growth is characterised through a constitutive law which as mentioned, is either stress or strain driven depending on the growth type, and is dependent on the growth factor. A local iterative procedure, involving the constitutive growth law and a finite difference approximation of the first order material time derivative of the growth factor, is hence established in order to solve the system of equations [20, 57]. In addition, with respect to the evolution of growth, it is known that the myocardium of the heart comprises of a network of tissue fibres which are arranged in helical patterns. It is understood that, during hypertrophy, an extension or thickening of these fibres occurs [32]. Hence, growth related modelling of cardiac tissue generally makes use of transversely isotropic growth laws. In the work of Werner et al. [81], transversely isotropic and isotropic growth were initiated on circular discs, defined as a cardiac tissue material, of which was additionally modelled using the theory of porous media in conjunction with an adapted form of the growth law presented by Goktepe et al. [20]. In the work of Hopkins [25], the methods of computing the the growth and remodelling processes related to cardiac systems, correlated to those proposed by Werner et al. [81] and Goktepe et al. [20]. In this study, which build upon the work of Hopkins [25], an improved method of representing the growth evolution, through an alternate description of the growth Jacobian, proposed by Werner et al. [80], is adapted and applied.

In order to model a full cardiac cycle, various mathematical models in the form of constitutive laws, for example, need to be defined for the various stages of the heart beat. The description of the diastolic filling stage was modelled using a strain energy function proposed by Usyk et al. [73]. This strain energy function, which governs how the body mechanically behaves, is stipulated for a material that displays orthotropic, exponential and near incompressible behaviour [73]. Cardiac tissue is generally treated as near incompressible, which has been substantially proven through various studies, such as with Vossoughi and Patel [77], who validated this hypothesis through hydrostatic stress tests on samples of myocardial tissue. Contrary to this however, Yin et al. [86], suggested that due to the composition of the myocardium which contains an array of blood vessels, of which are distensible, a change in density of the myocardial tissue could be observed as the vessel fluid volume alters during the transition between different stress states. The idealisation of cardiac tissue being orthotropic in nature is founded on the premise that the muscle fibres that constitute the myocardium, are contained within sheets that are additionally separated by cleavage planes, which results in three independent behavioural planes [61]. This theory was validated through experimental tests performed by Dokos et al. [14], who conducted shear tests on pig hearts, and more recently by tests performed on tissue of the human myocardium by

Sommer et al. [69].

Moving on to the active mechanics, an active tension model developed by Guccione and McCulloch [22], is utilised in this study and is dependent on the calcium intracellular concentration, sarcomere length and time. The contraction stage is initiated through a depolarising wave which propagates through the myocardium and excites the calcium ions. Physiologically, this process occurs in a asynchronous manner, whereby the muscle tissue contracts differently in space and time. Active stress models which are coupled with electro-mechanical models such as the Eikonel diffusion equations and the bidomain equations, are able to produce the feature of asynchronous conduction [33]. However, for simplicity, a synchronous active tension model is assumed in this research. In terms of the ejection stage of the cardiac cycle, which describes the hemodynamic process of blood being pumped into the systemic circulatory system, a three element Windkessel model is used.

1.4   Theory of porous media

Amongst the many sectors of science and engineering, understanding the material composition of a medium is essential in terms of describing the manner in which it behaves. The system could comprise of several types of solid constituents, or it could be a single porous solid matrix which is saturated with a fluid, of which could furthermore be in the form of a gas or liquid. The response of each material is unique based on its own micro-structural and chemical composition. Consequently, each material would contain different motions, and in systems which are multiphasic, interaction forces would hence exist. Composite materials may be very heterogeneous in terms of the pore structure, and the location and degree of saturation, of which could almost be impossible to describe. A framework which is able to describe the behaviour of multi-constituent systems, whilst confronting the difficult task of representing the composition accurately, may be found in the Theory of Porous Media.

The Theory of Porous Media, TPM, is based on the Theory of Mixtures coupled with the volume fractions concept (see [13, 16]). Utilising the Mixture Theory, results in a framework which is capable of describing systems which comprise of multiple constituents, and is furthermore able to characterise the internal interactions between the constituents [59]. The volume fractions concept assumes that the solid skeleton forms the boundary domain of the system and that only the fluid, which occupies the pore spaces, may leave or enter the control space [13]. In addition, it is assumed that the fluid fully saturates the pore spaces and that all pore spaces are statistically averaged out over the control space. Hence, the geometrical structure of the pore spaces nor the spacial arrangement are considered [13]. Thus, the Mixtures theory, restricted by the concept of volume fractions, results in framework which operates from the macroscale whilst taking into account microscale properties. This is done through idealising the porous body as a "*smeared*" continua, whereby each constituent simultaneously occupies the entire control space, defined by the boundary of the solid skeleton [13, 16].

In the work of Ricken et al. [59], a triphasic TPM model was proposed of which was modelled to represent a solid constituent body saturated with water containing nutrients. Furthermore, the triphasic model was formulated in context of describing transversely isotropic biological soft tissue, with the inclusion of growth and remodelling proliferation. The framework was built upon from the balance equations of momentum, mass, angular momentum and energy, and the entropy inequality. This allowed the constitutive equations to be developed for the solid and fluid constituents.

The constitutive law for the description of growth was based on a stress and nutrient driven law, which was furthermore applied to the case of a healing soft tissue wound and the study of stent restenosis in arteries after angioplasty [59].

In the work of Hopkins [25] a biphasic TPM model was implemented to describe the condition of Rheumatic Heart Disease, RHD, and was applied to patient specific, 3D left ventricle models, segmented from CMR scans. In this work, cardiac tissue was modelled for and included similar constitutive relations to those presented in the work of Ricken et al. [59] with respect to the formation of stress and filter velocity laws.

1.5 Research aims and objectives

Research into developing the current TPM framework in SESKA is the main objective. Consequently, due to the TPM framework only being recently implemented, there are various aspects which need to be addressed, which entail improving and expanding the current model. As such, the details relating to the continuation of research in the field of TPM and cardiac modelling shall be briefly discussed below.

1.5.1 Triphasic model development with inclusion of growth

The application of TPM has thus far been implemented using a biphasic model, in which the medium constituents comprise of a solid and fluid phase. The biological tissue growth of the heart in relation to rheumatic heart disease (RHD), is accounted for through a mass exchange between the solid and fluid phases, with the fluid volume and mass decreasing and the corresponding properties of the solid phase hence increasing. Although the current implemented model seems to be working adequately, it is understood that a few problems could arise, due to the decrease in fluid volume not being entirely reflective of true conditions [25].

Mitigating the problem associated with the biphasic model could be realised by creating a triphasic model through introduction of a third nutrient phase [25]. The nutrient phase would thus contribute to the growth of the system, instead of the liquid phase. Analytical and numerical techniques would need to be investigated in order to characterise the nutrient phase and to also adjust the current configuration of the existing model to accommodate the triphasic system. As such, the triphasic model which will be implemented is based on a model proposed by Ricken et al. [59]. In addition, a more expansive and versatile model will be realised by adding another phase onto the existing biphasic model. In future this could facilitate the substitution of biochemical constituents with specific constitutive laws, in place of the nutrient and liquid quantities.

In terms of growth, a more efficient, and mathematically consistent method of expressing the growth evolution, of which is derived from the balance equation of mass and represented through the growth Jacobian, is available in the work of Werner [80], as compared to that implemented in the current biphasic model. Implementing this growth law will hence form the second major objective of this research.

A summary of the objectives for this research project are as follows:

- Research into the cell/molecular biology of proliferative processes of rheumatic heart disease.

- Development of a triphasic TPM framework, with the addition of a nutrient phase, in accordance with Ricken et al. [59].

- Implementation of the method of computing growth evolution, as prescribed by Werner [80].

- Analysis of segmented patient-specific left ventricle models.

1.6 Limitations

This research will encapsulate a study into the mechanical and thermodynamic description of a patient specific left ventricle model with respect to porous media theory. In addition, growth and remodelling proliferation will also be investigated in relation to the condition of Rheumatic Heart Disease (RHD). This will include the application of a strain driven growth law, developed to model dilated cardiomyopathy, DCM, in particular. A critical feature of RHD is the condition whereby the valves, of the left ventricle especially, are left in an impaired state [34]. Proceeding from this, the heart becomes susceptible to developing other conditions, such as DCM. However, a response towards DCM may be found with respect to either mitral or aortic regurgitation [34]. As such, It should be noted that the scope of this research is limited to modelling the standard description of DCM, and can therefore not differentiate between the effects brought upon by the aforementioned valvular diseases. In addition, regurgitation of the left ventricular valves results in blood flow through the valves during periods which the valves are meant to be closed. This research will hence not focus on that aspect of the disease, and will be left for future consideration. Finally, this research is focused primarily on the left ventricle, and will thus neglect all contributions from the right ventricle, atria, and the pericardium.

1.7 Thesis overview

Chapter 2 will provide a basic introduction into the physiology and function of the heart. The microstructral and macrostructural architecture of the myocardium will then be addressed, of which will be followed by a summary of the cardiac cycle. Finally, the pathophysiology of Rheumatic Heart Disease will be covered.

Chapter 3 will outline the derivation for a Theory of Porous Media framework. Insight into the volume fractions concept, kinematics of TPM, and the kinematics of finite growth, will be considered, of which will then lead to the formulation of the balance equations and the entropy inequality.

Chapter 4 will then review the general TPM framework developed in Chapter 3, and after evaluation of the entropy inequality, an adaptation towards the case of a rheumatic heart will be conducted with respect to a triphasic model. This will result in the formulation of the constitutive relations needed to characterise the solid and fluid constituents, and the growth law.

Chapter 5 will lay forth the constitutive laws needed to model the various phases of the cardiac cycle. This will entail a definition of the stress tensor for the passive filling and active contraction. The hemodynamics of the heart will then be discussed in relation to the ejection component of the heartbeat.

Chapter 6 will then constitute a description of the numerical framework for the triphasic TPM model, of which will include the weak formulations, details regarding boundary condition application, temporal dicretization techniques, and the implementation of the cardiac mechanics model. Finally a numerical example will be discussed.

Chapter 7 will then proceed by applying the proposed triphasic framework on a left ventricle model of a patient diagnosed with RHD.

Finally, Chapter 8 will provide concluding remarks based on the analysis of the results in the previous chapter. Recommendations will then be put forth.

Chapter 2

Cardiac Physiology

2.1 Structure of the heart

The heart is often described as being a muscular pump which distributes blood through three circulatory systems, namely; the coronary , the pulmonary and the systemic. The coronary circulation is the circulation of blood within the heart and aims to feed the components of the heart. The pulmonary and systemic circulations comprise of the blood being pumped to the lungs and rest of the body, respectively, of which is illustrated in Fig.(2.1). [43]
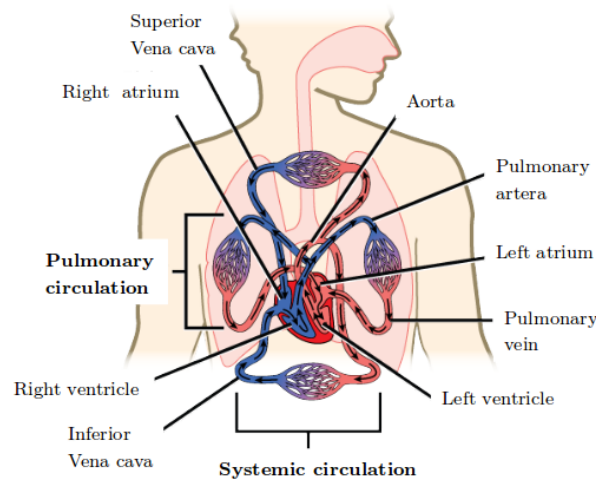
FIGURE 2.1: The illustration above depicts the various circulatory systems and components of the heart. [43, modified]

The heart is situated within the *thoracic cavity* and is suspended by an arrangement of vessels, enclosed by a fibrous sack, known as the *pericardium* [27]. The pericardium contains a lubricant which ensures smooth transitions during the hearts activity. Focusing on the heart itself, it may be viewed as being comprised of four chambers. The chambers consist of a left ventricle and atrium, and a right ventricle and atrium. The atria are known to receive blood whilst the ventricles are tasked with pumping. Deoxygenated blood flows into the right atrium through the *vena cava*, of which is part of the systemic circulation. The vena cava is split into the *superior vena cava* which is situated in the top half of the body, and the *inferior vena cava* which supplies the bottom half of the body. In addition, blood also enters the right atrium through the coronary circulation. The deoxygenated blood then passes through the *tricuspid valve*, of which only permits flow into the right venticle, and is then pumped into the pulmonary circulation through the *pulmonary valve*. Once the

blood is oxygenated through the lungs, it enters the left atrium, where it then fills the left ventricle. The *mitral valve* separates the left atrium and left ventricle and only permits flow in the direction of the aforementioned order of chambers. Lastly, oxygenated blood is pumped through the *aortic valve* into the systemic circulation where it is then expelled throughout the rest of the body. As illustrated in Fig.(2.3), the
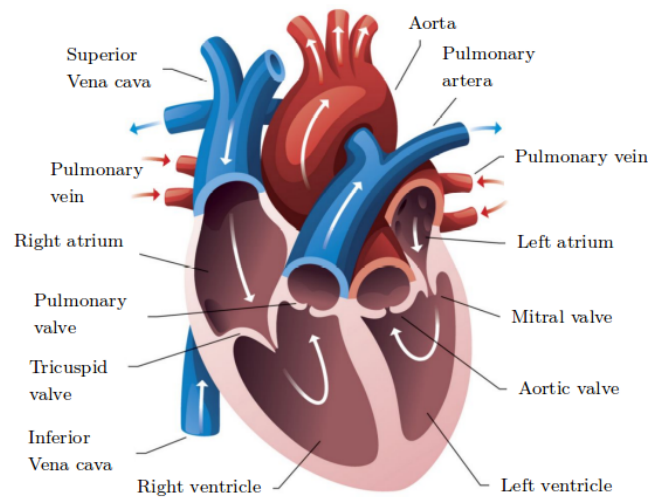
FIGURE 2.2: The illustration above depicts the various circulatory systems and components of the heart. [43, modified]

inner walls of the pericardium are adjacent to the outermost layer of the heart namely, the *epicardium*. The epicardium is one of three layers that makes up the muscle walls of the heart. The inner wall is defined as the *endocardium* while the central layer, which occupies the greatest volume of muscle, is known as the *myocardium*. The *base* of the heart is situated in the zone between the atria and ventricles and the *apex* is positioned at the bottom where the left ventricle and right ventricle converge. [27]
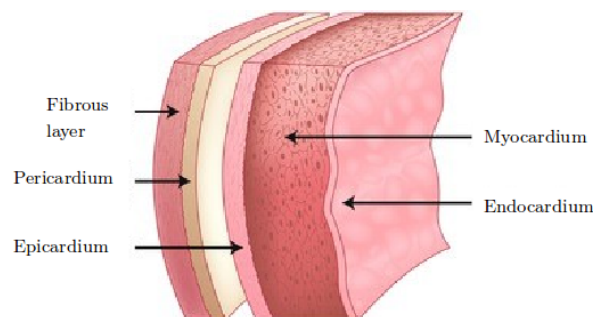
FIGURE 2.3: Cross-sectional view of the heart muscle. [71, modified]

2.1.1 Macro-structure of the myocardium

The human heart is made up of a network of muscle fibres arranged in helical patterns that collectively form sheets separated by cleavage planes. Consequently, this arrangement of muscle fibres results in the cardiac tissue being orthotropic with respect to its mechanical behaviour [61]. As such, understanding the configuration of the muscle fibres is of great significance with respect to modelling the mechanical and electrical

properties of cardiac systems. For example, it is well documented that cardiac muscle conducts electrical pulses anisotropically, showing greater levels of conduction across the fibre direction [6]. In addition, changes in the configuration of the fibres can provide important information with regard to certain conditions related to the heart [61].

The fibre bundles change in orientation between the base and apex, and across the myocardium. In Fig.(2.4), the muscle fibres have been illustrated with respect to the left ventricle [30]. As such, it may be noted that the fibre directions are orientated in opposite directions between the endocardium and epicardium. The approximate angles of the fibres at the endocardium and epicardium, according to literature (see e.g. [56, 61]), are in the range of 50° to 70° and -15° to -65°, respectively.
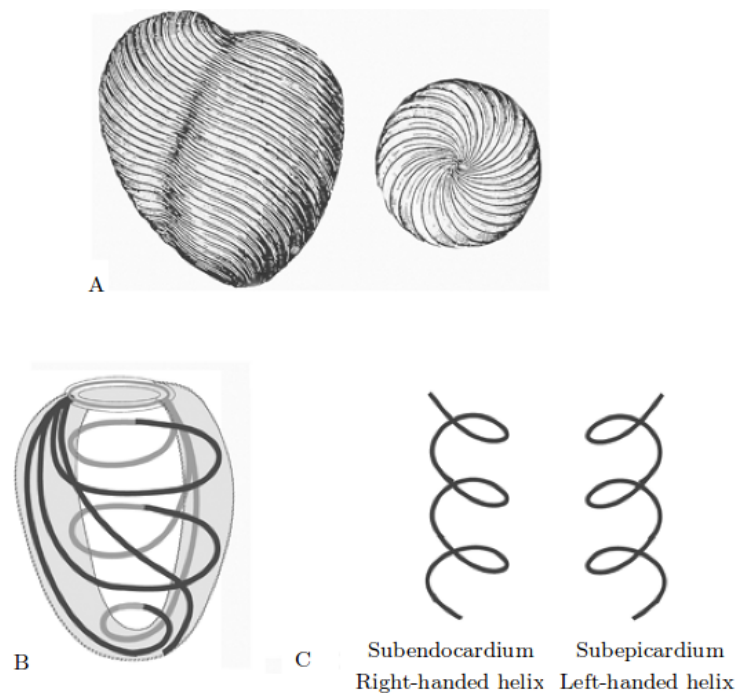
FIGURE 2.4: Helical structure of the myocardium. [30, modified]

2.1.2 Micro-structure of the myocardium

The myocardium, which accounts for majority of the muscle of the heart, is made up of a series of *myocytes* and connective tissue. Among the group of myocytes, *cardiac myocytes* or *cardiomyocytes* occupy most of the myocardial mass. However, 70% of the cells within the myocardium are composed of nanomyocytes which are additionally made up of *vascular smooth muscle*, *endothelial cells*, and *fibroblasts*. The fibroblasts help produce and maintain the connective tissue fibres that are partly responsible for the stiffness and tensile strength properties of the heart tissue. In addition, the connective tissue fibres are comprised of the *endomysium*, which surrounds each cardiomyocyte, the *perimysium*, which encompasses groups of myocytes, and the *epimysium*, which surrounds the whole muscle. [30]

Although there are several types of cardiomyocytes, *working myocytes* are associated primarily with muscle contraction. Working myocytes are cells which are comprised of cross-striates *myofibrils*, *mitochondria* and a central nucleus. Separating

the cells are *intercalated discs*, which transversely cut across the planes of the myofibres. The intercalated discs provides bonds between the various cardioymyocyte cells through strong links and also contains pores which help alleviate internal electrical resistance. Fig.(2.5) illustrates the structure of a working myocyte. [30]
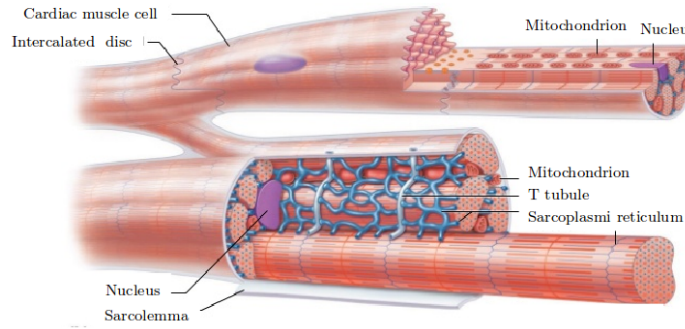
FIGURE 2.5: Anatomy of a cardiomyocyte. [26, modified]

The myofibrils, which are the contractile proteins, fill majority of the space within the cardimyocyte. The myofibrils may be further discomposed into a series of contractile entities called *sarcomeres*, which may be defined as the region between two bands known as *Z - lines* (see Fig.(2.6)) and furthermore represents the smallest functional units within the muscle. The Z - lines are anchored by *thin filaments* which are comprised of the protein: actin. *Thick filaments*, which contain myosin (a protein that helps dictate the displacement of muscle cells), reside within the sarcomeres and are centrally fixed by a protein arrangement known as an *M - line*. The length of the two thick filaments which occupy the space on either side of the M - line is called the *A - band* and consequently, the region between two consecutive A - bands is named the *I - band*. [27]
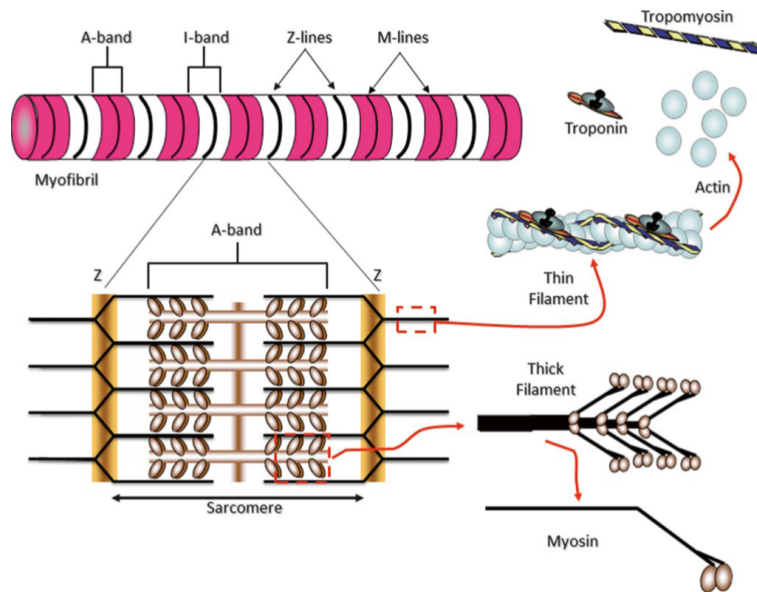
FIGURE 2.6: Composition of a sarcomere. [27]

2.2 Cardiac cycle

The function of the heart may be well understood through an interpretation of the mechanisms involved during a full cardiac cycle, and how these mechanisms correlate to the electrical activity of the heart. The cardiac cycle is often represented through the *Wiggers diagram*, of which is depicted in Fig.(2.7). The Wiggers diagram conveys the left ventricular pressure, left atrial pressure and the aortic pressure. Although the diagram excludes the properties of the right ventricle and atrium, it is known that the pressure and volume changes, and the timing of the different stages during the cycle, correlate closely to those of the left side of the heart. [34]
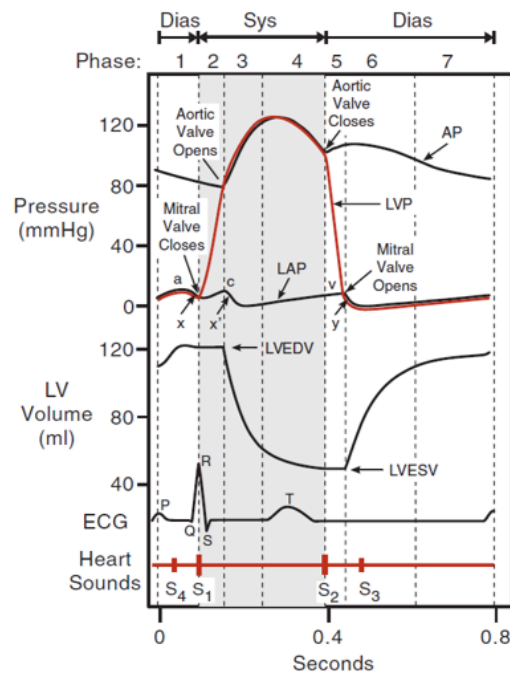
FIGURE 2.7: Composition of a sarcomere. [34]

Referring to Fig.(2.7), a full cardiac cycle is defined as the mechanisms involved at the onset of the P-wave in the electrocardiogram (ECG) till it passes through to the next P-wave. The cardiac cycle is often viewed to comprise of two stages: *systole* and *diastole*. Systole represents the stages of the cardiac cycle associated with isovolumetric contraction and ejection, whilst Diastole refers to the diastolic filling and the isovolumetric relaxation stages. The four aforementioned stages account for a complete cardiac cycle and may be easily represented in a pressure-volume graph (shown in Fig.(2.8)), which provides an alternate form to that shown in Fig.(2.7). [34]

As mentioned, the myocytes of the cardiac tissue are arranged in helical patterns. As such, during the onset of systole (start of the isovolumetric contraction stage), a pressure build-up is initiated in the left ventricle whilst the muscle fibres contract. Once the pressure within the left ventricle increases beyond that of the left atrium, the aortic valve is forced open, which hence allows an ejection of blood out of the ventricle. Since the pressure within the ventricle is greater than that of the atrium during systole, the mitral valve remains closed. During isovolumetric relaxation, and hence the start of diastole, the ventricular myocytes begin to relax, which consequently results in a decrease in ventricular pressure. When the pressure in the ventricles reduces below
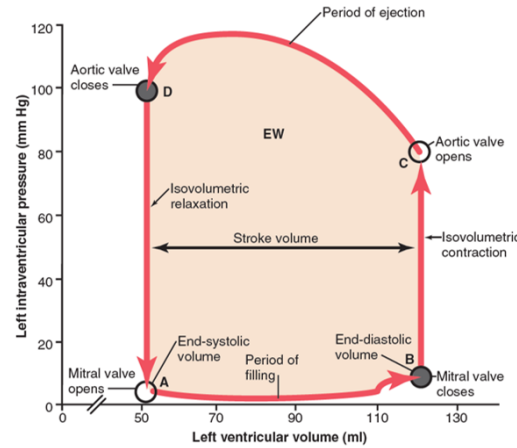
FIGURE 2.8: Ventricular pressure-volume curve associated with a complete cardiac cycle. [23]

that of the atrium, the mitral valve opens, and blood hence flows into the ventricle. In contrast, the change of pressure between the ventricle and atrium during diastole results in the aortic valve been closed for the duration of this phase. [27]

Referring to Fig.(2.8), the *end diastolic volume* (EDV) is the maximum volume attained at the end of the diastolic filling stage. Similarly, the *end systolic volume* (ESV) is the ventricular volume at the end of the ejection phase. Finally, the difference in volume between the ESV and EDV represents the *stroke volume* (SV). [34]

2.3 Rheumatic heart disease

Rheumatic heart disease (RHD) is a chronic heart condition which is caused by a series of attacks of *rheumatic fever* [45]. Acute rheumatic fever (ARF) is an autoimmune response to an infection with *Streptococcus pyogenes*, of which usually manifests in the form of fever, arthritis and cardiac valvular disease. Valvular dysfunction is the critical feature of RHD whereby the valves of the left ventricle are most commonly left in a state of permanent damage or complete failure [23, 45]. The right side of the heart is usually less affected due to the lower pressures enveloped [23]. Although uncommon, the disease is especially prevalent in developing countries which pose high levels of poverty. Penicillin has been found to be reliable in treating cases of ARF, however due to demographic factors, general treatment and management schemes are difficult to implement [45].

Rheumatic heart disease has a large impact on valvular function. In a healthy heart, with normal functioning valves, blood flow generates low pressure gradients within the valve and the flow is entirely one-directional. With abnormal functioning valves, these characteristics may become compromised, which may hence hinder the hearts ability to perform adequately [34]. The initial lesions which affect the valves as a result of ARF generally form on adjoining valve leaflets, which causes the leaflets to bond together. In addition, the free edges of the leaflets, which usually possess flexible material characteristics, often become stiff bundles of scar tissue [23].

When valve leaflets are bonded to each other to an extent whereby it restricts the flow of blood through the opening, the valve is said to be *stenosed*. In addition, when the free edges of the leaflets become rigid to a point in which they loose their ability to close, hence allowing a backflow of blood, this is termed *regurgitation* [23]. In both

aforementioned conditions, a maladaptive expansion of the muscle walls of the left ventricle, termed *hypertrophy*, is induced as a result of an increased workload [23, 30]. The hypertrophy of the ventricle may either be in the form of concentric or eccentric growth, whereby cardiomyocytes are added in parallel (increase in thickness) or in series (elongation of the tissue), respectively [53]. The two forms of sarcomere growth are dependent on whether the heart is subjected to a pressure or volume overload, as depicted in Fig.(2.9), which illustrates the mechanisms related to cardiac hypertrophic growth and remodelling.
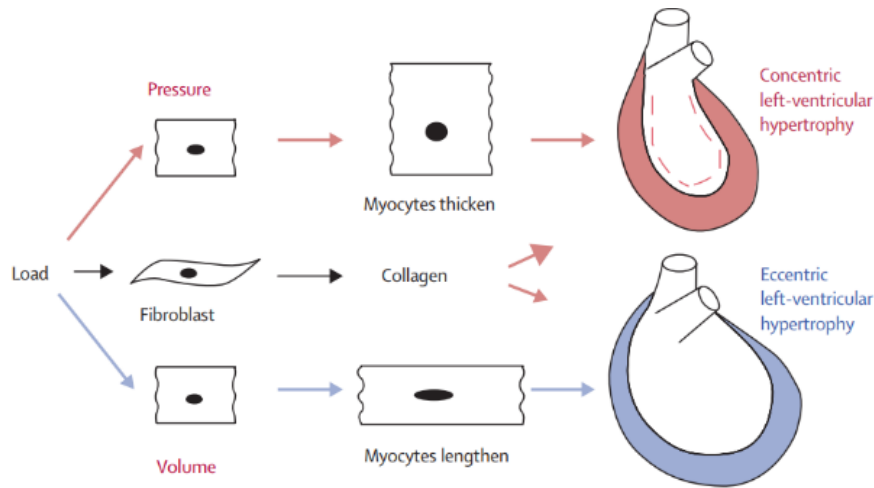
FIGURE 2.9: Eccentric and concentric cardiac hypertrophy of the left ventricle. [53, modified]

Within this study, attention will be focused on the case of eccentric hypertrophy (also known as dilated cardiomyopathy). Hence, the following section will consist of a description of eccentric hypertrophy and the, physiological changes and alterations in the pressure-volume curves, associated with it. In addition, valvular disease (associated with RHD) which may result in a dilated heart, will also be covered.

2.3.1 Dilated cardiomyopathy

Dilated cardiomyopathy, DCM, is a condition which is characterised by a dilated left ventricle. It may be caused by coronary or valvular disease and usually results in degraded myocardial muscle fibres. Consequently, the weakened muscle fibres has adverse effects on the pumping capacity of the heart, whereby the heart experiences a decrease in the end systolic pressure and vascular stiffness. Therefore, due to the dilation of the ventricular cavity, which additionally has a reduced pumping output, the ESV and EDV increases, but with a decreased SV. In addition, with a decrease in vascular stiffness, the slope of the pressure volume curve, at the point of EDV, namely, the *end diastolic pressure volume relationship* (EDPVR), reduces. The pressure volume curve which applies to the general case of DCM, is shown in Fig.(2.10). [1]

In terms of valvular disease associated with RHD, a dilated heart is commonly preceded by valvular regurgitation. As such, the conditions pertaining to mitral and aortic regurgitation will hence be discussed.

In mitral regurgitation, blood flows back into the left atrium during ejection, due to the impaired valve leaflets. Since the mitral valve is never entirely closed, a true IVC and IVR phase does not exist. Mitral regurgitation results in a volume overload of the
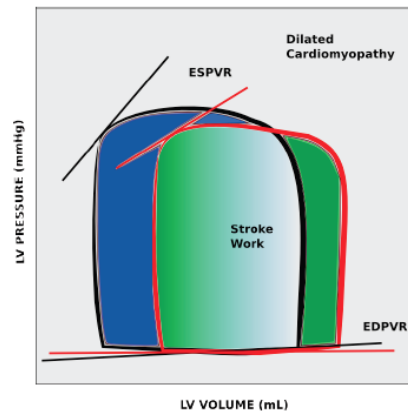
FIGURE 2.10: Pressure volume curve of a heart with dilated cardiomy-
opathy. [1]

ventricular cavity with a reduced pumping capacity. Hence the pressures enveloped
reduce during ejection. The effect of this is an increased EDV and SV. [34]

In the case of aortic valve regurgitation, blood is allowed to enter back into the
ventricles at the beginning of diastole. Similar to mitral regurgitation, this results in
there being no true IVR phase. An increase in blood in the ventricles before diastolic
filling results in an expanded starting volume. During filling, blood continuously enters
the ventricles from the aorta, which hence greatly increases the EDV. As such , the
pumping capacity becomes elevated to account for the increased load. A depiction of
the pressure volume curves associated with mitral and aortic regurgitation are present
in Fig.(2.11). [34]
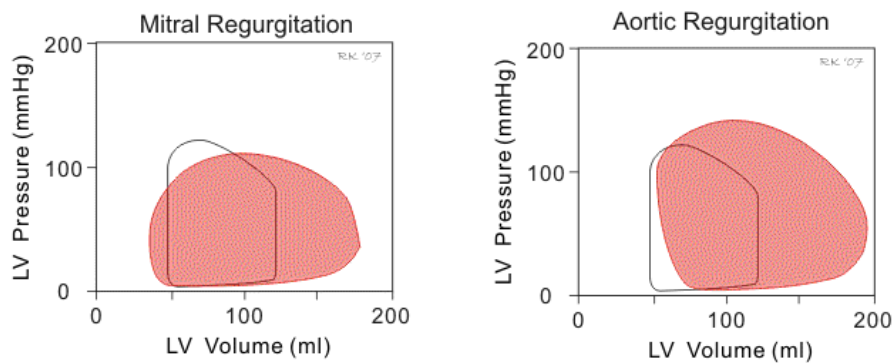
FIGURE 2.11: Pressure volume curve of a heart with valvular disease:
(left) Mitral regurgitation, (right) Aortic regurgitation. [34]

Chapter 3

Theory of Porous Media

In order to determine the behaviour of a porous system, which may be partly or fully saturated with a pore fluid, the Theory of Porous Media (TPM) may be used as a suffient framework to model such systems. The basis of TPM stems from the Theory of Mixtures, volume fractions concept, and the mechanical and thermodynamic balance equations, see e.g. De Boer [13] and Ehlers [17]. Hence, TPM may be used to accommodate multiphaisic porous bodies which consist of constituents with various mechanical or thermodynamic properties.

With regard to certain solid structures, such as concrete or steel, the effect of the porosity may be seen as negligible when considering it's structural performance. In addition, the constituents which fill these pore spaces, e.g. air or water, are also viewed to not contribute much to the overall behaviour. Therefore, when considering these materials, it is common practice and adequate to an acceptable level of accuracy, to treat them as homogeneous, single phase bodies. However, certain materials such as biological tissue, are greatly influenced by the fluid saturating the pore spaces. The fluid may have adverse effects on the permeability, stress and growth and remodelling mechanisms, which subsequently may be all interconnected. Thus, the inclusion of these pore fluids during the analysis of biological tissue is crucial in terms of generating accurate models.

Porous bodies have a huge array of considerations to take into account, for example regarding the material properties, individual motions of the particles pertaining to each constituent, various interaction forces, and description of the pore localization. Describing these quantities may present itself as an overwhelming and impossible task. However, with the use of the theory of mixtures, coupled with the volume fractions concept, a far simpler approach is available. This concept is based on homogenizing and statistically distributing the constituent components over the control space of the body, of which results in a "*smeared*" model. Therefore, this method proceeds from the macro scale, with all the micro-level quantities being averaged and cast into macro-quantities.

In the following sections, an illustration of all the basic principles behind TPM will be presented.

3.1 Volume Fraction Concept

In the framework of TPM, a solid porous skeleton is saturated with pore fluids, which constitute the κ constituents of the control space. As mentioned, the following method employs a smeared continua, whereby the constituent components are averaged out over the control space, of which applies to all geometric and mechanical properties related to each constituent, such as the stress and motion. With respect to the mixture theory and volume fractions concept, it is assumed that each phase occupies the entire domain of the control space and exists simultaneously amongst the other phases.

A visual representation of the volume fractions concept is displayed in Fig.(3.1). The control space in the reference configuration, at time t=t$_0$, is defined by B$_{0S}$ and

theory of mixtures

dv

homogenised model

dv$^{\text{Solid}}$

dv$^{\text{Fluid}}$

micro structure

concept of volume fractions
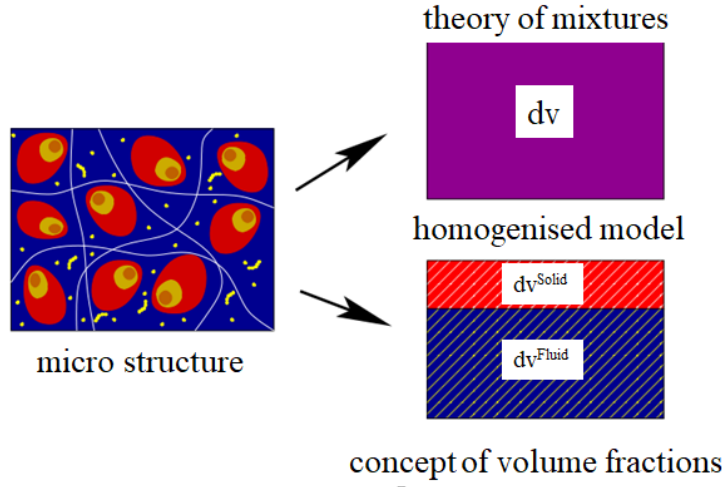
FIGURE 3.1: Illustration of the volume fraction concept and mixture theory. [35, modified]

bordered by the surface ∂B$_{0S}$. Similarly, in the spatial configuration at time t, the volume of the control space is given by B$_S$ and with surface area ∂B$_S$. The boundaries of the control space are given in terms of the solid skeleton as it is assumed that the pore fluid lies within the domain of the solid constituent, see De Boer [13].

The *volume fraction* may be defined as the local volume portion which belongs to the individual constituents φ^α, with α being one of the κ constituents. Consequently, in the reference configuration, the volume fraction is given by

$$n^\alpha_{0\alpha} = n^\alpha_{0\alpha}\left(\mathbf{X}_\alpha,\ t = t_0\right) \tag{3.1}$$

and is represented in terms of the material position $\mathbf{X}_\alpha$. The partial volume V$^\alpha_0$ pertaining to the individual constituent φ^α in the reference configuration is given by

$$V^\alpha_0 = \int_{B_{0S}} n^\alpha_{0\alpha}\, dV_{0\alpha} = \int_{B_{0S}} dV^\alpha_{0\alpha} \tag{3.2}$$

with the partial volume element dV$^\alpha_0$ and the real volume element dV$^\alpha_{0\alpha}$ being related by the following condition:

$$n^\alpha_{0\alpha}\, dV_{0\alpha} = dV^\alpha_{0\alpha} \tag{3.3}$$

The volume of the reference configuration may hence be given by

$$V_0 = \int_{B_{0S}} dV_{0\alpha} = \sum_{\alpha=1}^{\kappa} V^\alpha_0 = \int_{B_{0S}} \sum_{\alpha=1}^{\kappa} dV^\alpha_{0\alpha} = \int_{B_{0S}} \sum_{\alpha=1}^{\kappa} n^\alpha_{0\alpha}\, dV_{0\alpha} \tag{3.4}$$

By making use of Eq.(3.1) and Eq.(3.2), Eq.(3.4) hence allows the following conclusion to be drawn in relation to the volume fraction $n^\alpha_{0\alpha}$:

$$dV_{0\alpha} = \sum_{\alpha=1}^{\kappa} n^\alpha_{0\alpha}\, dV_{0\alpha} \tag{3.5}$$

which finally leads to expression of the *saturation condition*:

$$\sum_{\alpha=1}^{\kappa} \mathrm{n}_{0\alpha}^{\alpha} = 1 \tag{3.6}$$

which states that the summation of the volume fractions of the constituents is equal to unity. This condition is important in the formulation of TPM and will be extensively used in the chapters to follow.

In the spatial configuration the volume fraction may be defined in terms of the spatial position $\mathbf{x}$ and time t, such that

$$\mathrm{n}^{\alpha} = \mathrm{n}^{\alpha}(\mathbf{x}, \text{ t}) \tag{3.7}$$

Similar to Eq.(3.4) the partial volume of the control space in the actual configuration is postulated by

$$V = \int_{\mathrm{B_S}} \mathrm{dv} = \int_{\mathrm{B_{0S}}} \sum_{\alpha=1}^{\kappa} \mathrm{n}^{\alpha} \, \mathrm{dv} \tag{3.8}$$

which results in the saturation condition of the spatial configuration:

$$\sum_{\alpha=1}^{\kappa} \mathrm{n}^{\alpha} = 1 \tag{3.9}$$

Eq.(3.6) and Eq.(3.9) proves that the saturation condition must always be fulfilled.

The total mass of the entire system, consisting of κ constituents in the reference and spatial configuration, is respectively given by

$$\mathrm{M}_0 = \sum_{\alpha=1}^{\kappa} \mathrm{M}_0^{\alpha} = \int_{\mathrm{B_{0S}}} \sum_{\alpha=1}^{\kappa} \rho_{0\alpha}^{\alpha} \, \mathrm{dV}_{0\alpha}, \quad \mathrm{M} = \sum_{\alpha=1}^{\kappa} \mathrm{M}^{\alpha} = \int_{\mathrm{B_S}} \sum_{\alpha=1}^{\kappa} \rho^{\alpha} \, \mathrm{dv} \tag{3.10}$$

whereby $\rho_{0\alpha}^{\alpha}$ and ρ^{α} are the partial densities in the respective configurations and are furthermore defined as

$$\rho_{0\alpha}^{\alpha} = \rho_{0\alpha}^{\alpha}\left(\mathbf{X}_{\alpha}, \text{ t} = \mathrm{t}_0\right), \quad \rho^{\alpha} = \rho^{\alpha}(\mathbf{x}, \text{ t}) \tag{3.11}$$

The real density may be defined as the density over the entire control space, of which is given by

$$\rho_{0\alpha}^{\alpha\mathrm{R}} = \rho_{0\alpha}^{\alpha\mathrm{R}}\left(\mathbf{X}_{\alpha}, \text{ t} = \mathrm{t}_0\right), \quad \rho^{\alpha\mathrm{R}} = \rho^{\alpha\mathrm{R}}(\mathbf{x}, \text{ t}) \tag{3.12}$$

in the reference and spatial configuration, respectively. The expression for the partial mass may be now be expressed in the form

$$\mathrm{M}_0^{\alpha} = \int_{\mathrm{B_{0S}}} \rho_{0\alpha}^{\alpha} \, \mathrm{dV}_{0\alpha} = \int_{\mathrm{B_{0S}}} \rho_{0\alpha}^{\alpha\mathrm{R}} \, \mathrm{dV}_{0\alpha}^{\alpha}, \quad \mathrm{M}^{\alpha} = \int_{\mathrm{B_S}} \rho^{\alpha} \, \mathrm{dv} = \int_{\mathrm{B_S}} \rho^{\alpha\mathrm{R}} \, \mathrm{dv}^{\alpha} \tag{3.13}$$

which hence allows the relationship between the real and partial to be defined as

$$\rho_{0\alpha}^{\alpha} = \mathrm{n}_{0\alpha}^{\alpha} \rho_{0\alpha}^{\alpha\mathrm{R}}, \quad \rho^{\alpha} = \mathrm{n}^{\alpha} \rho^{\alpha\mathrm{R}} \tag{3.14}$$

From a physical aspect, the real densities represent the true densities on the macro-scale. In comparison to the mixture theory, the compressibility of the material may be defined using the volume fractions concept to either define a compressible condition ($\rho^{\alpha\mathrm{R}} \neq$ const.) or an incompressible condition ($\rho^{\alpha\mathrm{R}} = \rho_{0\alpha}^{\alpha\mathrm{R}} =$ const.), see De Boer [13].

3.2 Kinematics

The saturated porous solid will be idealized as a statistically distributed immiscible mixture comprising of constituents φ^α with particles $\mathbf{X}_\alpha$. In the reference configuration, the material particles of each constituent $\mathbf{X}_\alpha \in \mathbf{B}_S$ are independent of one another and hence occupy different spatial positions. However, making use of the concept of superimposed continua, it is postulated that each particle of the current configuration, at an arbitrary time t, simultaneously occupies the same spatial point $\mathbf{x}$ as the rest of the κ constituent particles, see [13] and [17]. Due to the constituents having different material points at t_0 it may deduced that each individual constituent has its own kinematic equation of motion

$$\mathbf{x} = \mathcal{X}_\alpha(\mathbf{X}_\alpha, t) \tag{3.15}$$

of which may also be termed as the *Lagrange* description of motion. With $\mathcal{X}_\alpha$ being unique and continuous, the inverse mapping of Eq.(3.15) exists in the form of the *Eulerian* description of motion:

$$\mathbf{X}_\alpha = \mathcal{X}_\alpha^{-1}(\mathbf{x}, t) \tag{3.16}$$

of which may only be true if the mathematical condition of a non-zero *Jacobian*, which may be expressed as the determinant of the *deformation gradient* $\mathbf{F}_\alpha$, is satisfied for each constituent:

$$\mathbf{F}_\alpha = \frac{\partial \mathcal{X}_\alpha}{\partial \mathbf{X}_\alpha}, \qquad J_\alpha = \det \mathbf{F}_\alpha \neq 0 \tag{3.17}$$

An illustration of the kinematic framework used within TPM is shown in Fig.(3.2). Following from Eq.(3.15), it may be observed that each constituent possesses its own velocity and acceleration field. In the Lagrangian configuration, these are stated as

$$\mathbf{x}_\alpha' = \frac{\partial \mathcal{X}_\alpha(\mathbf{X}_\alpha, t)}{\partial t}, \qquad \mathbf{x}_\alpha'' = \frac{\partial^2 \mathcal{X}_\alpha(\mathbf{X}_\alpha, t)}{\partial t^2} \tag{3.18}$$

From Eq.(3.16), the velocity and acceleration fields may be arranged in the Eulerian setting, such that

$$\mathbf{x}_\alpha' = \mathbf{x}_\alpha'(\mathbf{x}, t), \qquad \mathbf{x}_\alpha'' = \mathbf{x}_\alpha''(\mathbf{x}, t) \tag{3.19}$$

The set of motion functions shown in Eq.(3.19) differ from those in Eq.(3.18) in the sense that they are dependent on time t and the spatial position $\mathbf{x}$. Therefore, in the Eulerian configuration, the motion of a particle is not only governed by time but also on the path followed through space. This results in the following relationship, with respect to an arbitrary scalar-value function $\Gamma(\mathbf{x}, t)$:

$$(\Gamma)_\alpha' = \frac{\partial \Gamma}{\partial t} + \mathrm{grad}\Gamma \cdot \mathbf{x}_\alpha' \tag{3.20}$$

of which is often referred to as the *material time derivative*. The operator "grad$(\cdot)$" shown above, denotes the partial derivative of $(\cdot)$ with respect to the spatial position. Similarly, Grad$(\cdot)$ is defined as the partial derivative with respect to the material position.

For problems involving a multiphase coupling of a porous solid and $\kappa - 1$ fluids, one would generally continue from a Lagrangian description of the solid phase, with the solid displacement vector $\mathbf{u}_S$ being the unknown variable. However, with respect to the fluid phases, greater ease is found by adopting the Eulerian setting and by using
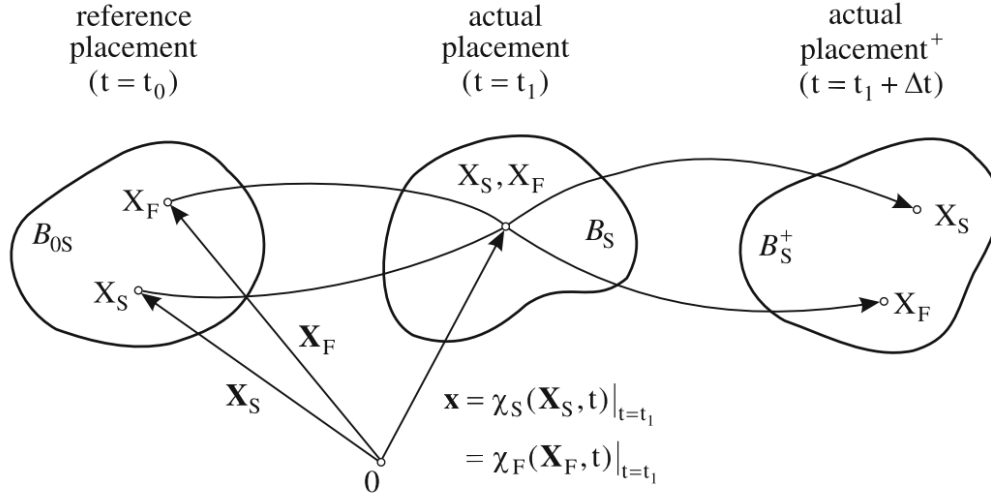
FIGURE 3.2: Illustration of the motion of a solid and fluid constituent in a porous body. [58]

the relative velocity between each respective fluid phase and the solid skeleton [17]:

$$\mathbf{u}_\text{S} = \mathbf{x} - \mathbf{X}_\text{S}, \qquad \mathbf{w}_{\beta\text{S}} = \mathbf{x}'_\beta - \mathbf{x}'_\text{S} \tag{3.21}$$

Using Eq.$(3.17)_1$ and the operator's introduced in Eq.(3.20), an alternate form of the deformation gradient and its inverse may be given by

$$\mathbf{F}_\alpha = \frac{\partial \mathbf{x}}{\partial \mathbf{X}_\alpha} = \text{Grad}_\alpha \mathbf{x}, \qquad \mathbf{F}_\alpha^{-1} = \frac{\partial \mathbf{X}_\alpha}{\partial \mathbf{x}} = \text{grad} \mathbf{X}_\alpha \tag{3.22}$$

Using Eq.$(3.18)_1$, the *spatial velocity gradient* may be written as

$$\mathbf{L}_\alpha = \frac{\partial \mathbf{x}'_\alpha}{\partial \mathbf{x}} \tag{3.23}$$

The spatial velocity gradient could also alternatively be written as

$$\mathbf{L}_\alpha = \frac{\partial \mathbf{x}'_\alpha}{\partial \mathbf{x}} = \frac{\partial \mathbf{x}'_\alpha}{\partial \mathbf{X}_\alpha} \frac{\partial \mathbf{X}_\alpha}{\partial \mathbf{x}} = \frac{1}{\partial t} \left(\frac{\partial \mathbf{x}}{\partial \mathbf{X}_\alpha} \right) \frac{\partial \mathbf{X}_\alpha}{\partial \mathbf{x}} = (\mathbf{F}_\alpha)'_\alpha \mathbf{F}^{-1}{}_\alpha \tag{3.24}$$

which then leads to the time derivative of the deformation gradient:

$$(\mathbf{F}_\alpha)'_\alpha = \mathbf{L}_\alpha \mathbf{F}_\alpha \tag{3.25}$$

The spatial velocity gradient may be decomposed into its symmetric and skew-symmetric parts, such that the symmetric part

$$\mathbf{D}_\alpha = \frac{1}{2} \left[\frac{\partial \mathbf{x}'_\alpha}{\partial \mathbf{x}} + \left(\frac{\partial \mathbf{x}'_\alpha}{\partial \mathbf{x}} \right)^\text{T} \right] \tag{3.26}$$

produces the *rate of deformation tensor* and the skew-symmetric part

$$\mathbf{W}_\alpha = \frac{1}{2} \left[\frac{\partial \mathbf{x}'_\alpha}{\partial \mathbf{x}} - \left(\frac{\partial \mathbf{x}'_\alpha}{\partial \mathbf{x}} \right)^\text{T} \right] \tag{3.27}$$

results in the *vorticity tensor* As shown by Eq.$(3.22)_1$, the deformation gradient is a tangent map that transports particles between the reference and current configuration.

For later usage, the mapping of surface and volume elements of the solid skeleton shall be defined. The surface element in the reference configuration dA_S with unit normal $\mathbf{n}_0$ may be related to the surface element in the current configuration da_S with unit normal $\mathbf{n}$ by

$$\mathbf{n}\,da_S = J_S \mathbf{F}_S^{-T} \mathbf{n}_0 \, dA_S \tag{3.28}$$

and the relationship between the volume elements is given by

$$dv_S = J_S \, dV_S \tag{3.29}$$

The *right Cauchy Green tensor* may be defined as

$$\mathbf{C}_S = \mathbf{F}_S^{T} \mathbf{F}_S \tag{3.30}$$

whereby the *Green tensor* may then be expressed as

$$\mathbf{E}_S = \frac{1}{2}(\mathbf{F}_S^{T}\mathbf{F}_S - 1) = \frac{1}{2}(\mathbf{C}_S - 1) \tag{3.31}$$

3.2.1 Kinematics of Growth

Growth is an aspect of living matter which has intrigued an array of researches from a variety of disciplines for many years. The connection between growth and the environment acting on a living body is a fascinating feature due the fact that they both influence each other [3]. This feature has led to the categorization of growth in two distinct types in the field of biomechanics, namely; growth-induced microenvironmental changes, and mechanically-induced microstructural changes [37]. The first type of growth related phenomena revolves around how the biological conditions of a system can trigger a mechanical response, which may be in the form of growth-induced structural instabilities, stresses and strains [42]. Such studies have been performed in plant physiology [5, 74], applied mathematics [21], and biomechanics [29]. The rapid development of computational modelling and the use of numerical methods such as the finite element method, has made analysing and predicting growth-induced changes more robust and has hence benefited researches in recent times [37]. In addition computational growth modelling has provided clinical researches with a new tool to better understand how certain diseases may progress, such as in the case of tumor growth[50], and the narrowing of airways due to asthma [48]. [37]

The second growth type is one which has been extensively applied to biological soft tissue, and is more centred on studying the mechanisms that result in growth, and how these mechanisms influence the biology of the system [47]. The forces which stimulate growth and the appearance of the grown system are closely related, for example, a body which grows unbounded in all directions, termed volume growth, would presumably be caused by an isotropic force such as a pressure load. An example of this is present within the study of the effects of hypertension on arterial walls [24, 36]. In contrast, growth that arises within a surface, referred to as area growth, would be caused by planar mechanisms, of which finds application in the study of artificial skin repair and regrowth procedures [67, 70]. Lastly, anisotropic growth which occurs along a specific direction would be assumed to be initiated by a load of equivalent form, such as fibre stretch for example. Anisotropic growth has been used in research related to growth of muscle fibres associated with limb lengthening procedures [89]. As discussed in Chapter 2, cardiac tissue is comprised of muscle fibres

which are helically arranged within the myocardium. Hence, it is general convention that eccentric and concentric hypertrophy of the myocardium is conceptualized and modelled as a thickening or lengthening of the muscle fibres (see [20, 57]). As such, this research study makes use of an anisotropic growth function to model the growth and remodelling processes of a left ventricle system. [37]

The subsequent sections will follow discussions based on the mathematical description of growth and its incorporation within a continuum mechanics framework.

Continuum modelling of growth

Mathematical descriptions of finite growth was first integrated within the framework of continuum mechanics by Skalak et al. [64]. However, the kinematic description of growth in this work resulted in incompatibilities with respect to the mapping between the various configurations [80]. This is due to the fact that with growth, the idea of the reference configuration becomes obscure. A method which avoids this issue is presented in context of finite crystal plasticity, developed by Lee [40] and which was later adapted to model growth by Rodriguez et al. [60]. This kinematic approach employs a multiplicatively split deformation gradient $\mathbf{F}_S$ into an elastic part $\mathbf{F}_{Se}$, and a growth part $\mathbf{F}_{Sg}$: [47]

$$\mathbf{F}_S = \mathbf{F}_{Se}\mathbf{F}_{Sg} \tag{3.32}$$

This results in the formation of a stress free intermediate configuration, whereby the deformation resulting parts are captured within the elastic zone (between the intermediate and actual configuration). As such, the kinematics of finite growth, which includes the composition of the various configurations, is illustrated in Fig. (3.3).
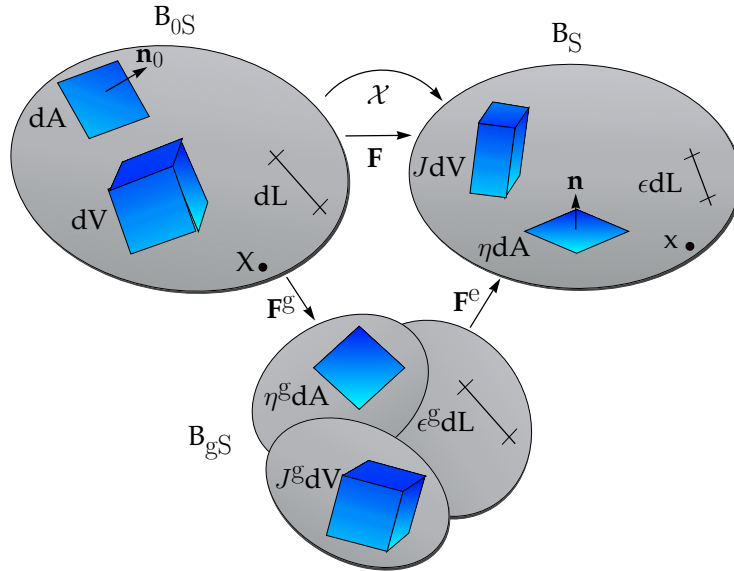
FIGURE 3.3: Illustration of the kinematics of growth, which includes the stress free (intermediate) configuration.

Following the description of the multiplicative decomposition of $\mathbf{F}_S$, the same principle may be applied to the Jacobian whereby it's comprised of an elastic part, which translates into volume change due to deformation, and an irreversible growth part, which causes a volume change due to deposited matter: [37]

$$J_S = J_{Se}J_{Sg} \tag{3.33}$$

whereby the components comply with the following conditions:

$$J_{Se} = \det(\mathbf{F}_{Se}), \quad J_{Sg} = \det(\mathbf{F}_{Sg}) \tag{3.34}$$

With $\mathbf{n}_0$ being the unit normal to the surface in the reference configuration, the total stretch ϵ in the actual configuration, in the direction of $\mathbf{n}_0$, is given by

$$\epsilon = \|\mathbf{F}_S\,\mathbf{n}_0\| = \epsilon_e\epsilon_g \tag{3.35}$$

where ϵ_e and ϵ_g represents the stretch components, in similar analogy to the previous quantities. In relation to cardiac tissue growth, ϵ_g would hence represent the stretch caused by a generation of sarcomeres in relation to a maladaptive response to a pressure or volume overload [20]. The elastic and growth parts of the Cauchy Green stress tensor are defined as

$$\mathbf{C}_{Se} = \mathbf{F}_{Se}^T\mathbf{F}_{Se}, \quad \mathbf{C}_{Sg} = \mathbf{F}_{Sg}^T\mathbf{F}_{Sg} \tag{3.36}$$

In Table (7.6), $\mathbf{F}_{Sg}$ and it's inverse are defined for volume, surface and fibre, growth types. The expressions are given in terms of the growth multiplier ϑ, of which differs for each growth type. This section merely introduces the basic framework employed for finite growth. However, a detailed description of how growth is modeled in this study, which includes the constitutive laws needed to characterized the rate of growth, is covered in Sec.(4.4.3).

TABLE 3.1: Expressions for the growth part of the deformation gradient $\mathbf{F}_{Sg}$, and its inverse $\mathbf{F}_{Sg}^{-1}$, for volume and fibre growth types.

Quantity	Growth type	
	Volume	fibre
ϑ	J_{Sg}	ϵ_g
$\mathbf{F}_{Sg}$	$\vartheta^{\frac{1}{3}}\mathbf{I}$	$\mathbf{I} + (\vartheta - 1)\mathbf{n}_0 \otimes \mathbf{n}_0$
$\mathbf{F}_{Sg}^{-1}$	$\vartheta^{-\frac{1}{3}}\mathbf{I}$	$\mathbf{I} + \left(\frac{1}{\vartheta} - 1\right)\mathbf{n}_0 \otimes \mathbf{n}_0$

It should be noted that the expressions of $\mathbf{F}_{Sg}$, complies with the condition given in Eq. (3.34). In addition, the inverse of $\mathbf{F}_{Sg}$ for fibre growth can't be derived directly. However, an expression is able to be developed using the Sherman-Morrison formula.

It is apparent that $\mathbf{F}_{Sg}$, for the volume growth type, results in a function of isotropic nature, characterized by the identity matrix $\mathbf{I}$, scaled up by the degree of growth, whereby growth occurs equally along all three directions. For fibre growth, it is clear that $\mathbf{F}_{Sg}$ is formulated in a way that results in growth not occurring in the directions other than the fibre direction, whereby only the fibre direction is trivially scaled up by ϑ.

3.3 Balance Equations

If a body is disturbed in any manner, such as in the case of an exerted force, or applied temperature differential, for example, then the following laws may be used to describe the behaviour of the body. The balance equations consist of the; balance of mass, balance of momentum, balance of moment of momentum and the balance of energy. In addition, the latter aforementioned balance equation and the entropy inequality

will form part of the first and second laws of thermodynamics, and are pivotal in formulating the theoretical framework for the Theory of Porous Media.

3.3.1 Balance of Mass

The mass M^α of each constituent φ^α may be postulated as the volume integral of the density ρ^α.

$$M^\alpha = \int_{B_\alpha} \rho^\alpha dv \tag{3.37}$$

With the inclusion of mass exchange between constituents, the rate of change of mass within the closed system domain may be expressed as

$$(M^\alpha)'_\alpha = \int_{B_\alpha} \hat{\rho}^\alpha dv \tag{3.38}$$

In order to ensure that the mass of the body is conserved the following condition should be satisfied

$$\sum_{\alpha=1}^{\kappa} \hat{\rho}^\alpha \overset{!}{=} 0 \tag{3.39}$$

Making use of the transport theorem

$$(dv)'_\alpha = \text{div}(\mathbf{x}'_\alpha)dv \tag{3.40}$$

and by equating Eq.(3.38) to the material time derivative of Eq.(3.37), the final global form of the balance of mass is obtained and given by

$$\int_{B_\alpha} \hat{\rho}^\alpha dv = \int_{B_\alpha} [(\rho^\alpha)'_\alpha + \rho^\alpha \text{div}(\mathbf{x}'_\alpha)]dv \tag{3.41}$$

3.3.2 Balance of Momentum

The derivation of the balance of momentum firstly begins with the equation shown below, which states that the material time derivative of momentum is equal to the sum of all external forces $\mathbf{k}^\alpha$ and internal interaction forces between all constituents:

$$(\mathbf{l}^\alpha)'_\alpha = \mathbf{k}^\alpha + \int_{B_\alpha} \hat{\mathbf{p}}^\alpha dv \tag{3.42}$$

In Eq.(3.42) $\mathbf{l}^\alpha$ defines the linear momentum (also referred to as the translational momentum) and is expressed as

$$\mathbf{l}^\alpha = \int_{B_\alpha} \rho^\alpha \mathbf{x}'_\alpha dv \tag{3.43}$$

and $\mathbf{k}^\alpha$ being expanded as

$$\mathbf{k}^\alpha = \int_{B_\alpha} \rho^\alpha \mathbf{b}^\alpha dv + \int_{\partial B_\alpha} \mathbf{t}^\alpha da \tag{3.44}$$

with $\mathbf{b}^\alpha$ and $\mathbf{t}^\alpha$ denoting the body force and surface traction, respectively. Using Cauchy's theorem, the surface integral of $\mathbf{t}^\alpha$ may be cast in the following forms:

$$\int_{\partial B_\alpha} \mathbf{t}^\alpha da = \int_{\partial B_\alpha} \mathbf{T}^\alpha \mathbf{n} da = \int_{\partial B_\alpha} \mathbf{T}^\alpha d\mathbf{a} \tag{3.45}$$

whereby the Cauchy stress tensor $\mathbf{T}^\alpha$ and the surface normal vector in the current configuration $\mathbf{n}$ have been utilized. Considering the divergence theorem, Eq.(3.45) may be transformed into the volume integral form shown below

$$\int_{\partial B_\alpha} \mathbf{T}^\alpha \mathbf{n}\,\mathrm{da} = \int_{B_\alpha} \mathrm{div}\mathbf{T}^\alpha \mathrm{dv} \tag{3.46}$$

By virtue of Eq.(3.43), Eq.(3.44) and Eq.(3.46), the balance equation of momentum Eq.(3.42), may be expressed in the following global form:

$$\int_{B_\alpha} (\rho^\alpha \mathbf{x}''_\alpha + \hat{\rho}^\alpha \mathbf{x}'_\alpha)\mathrm{dv} = \int_{B_\alpha} (\mathrm{div}\mathbf{T}^\alpha + \rho^\alpha \mathbf{b}^\alpha)\mathrm{dv} + \int_{B_\alpha} \hat{\mathbf{p}}^\alpha \mathrm{dv} \tag{3.47}$$

3.3.3 Balance of Moment of Momentum

The third and final mechanical balance equation focuses on the moment of momentum (also referred to as the angular or rotational momentum) of a body and that resulting from external forces. For a non-polar partial body, the balance equation of moment of momentum, determined about the reference position 0, for each constituent φ^α is represented by

$$(\mathbf{h}^\alpha_{(0)})'_\alpha = \mathbf{m}^\alpha_{(0)} + \int_{B_\alpha} \mathbf{x} \times \hat{\mathbf{p}}^\alpha \,\mathrm{dv} \tag{3.48}$$

with $\hat{\mathbf{p}}$ providing the exchange of momentum that results from the interaction forces between phases, and $\times$ being the cross product operator. The moment of momentum of the body $\mathbf{h}^\alpha_{(0)}$ and it's material time derivative are given by

$$\mathbf{h}^\alpha_{(0)} = \int_{B_\alpha} \mathbf{x} \times \rho^\alpha \mathbf{x}'_\alpha \,\mathrm{dv} \tag{3.49}$$

$$(\mathbf{h}^\alpha_{(0)})'_\alpha = \int_{B_\alpha} \mathbf{x} \times (\rho^\alpha \mathbf{x}''_\alpha + \hat{\rho}^\alpha \mathbf{x}'_\alpha) \,\mathrm{dv} \tag{3.50}$$

With the expression of the momentum of the external forces $\mathbf{m}^\alpha_{(0)}$

$$\mathbf{m}^\alpha_{(0)} = \int_{B_\alpha} \mathbf{x} \times \rho^\alpha \mathbf{b}^\alpha \,\mathrm{dv} + \int_{\partial B_\alpha} \mathbf{x} \times \mathbf{T}^\alpha \,\mathrm{da} \tag{3.51}$$

and making use of the divergence theorem

$$\int_{\partial B_\alpha} \mathbf{x} \times \mathbf{T}^\alpha \,\mathrm{da} = \int_{B_\alpha} \mathbf{x} \times \mathrm{div}\mathbf{T}^\alpha + \mathbf{I} \times \mathbf{T}^\alpha \,\mathrm{dv} \tag{3.52}$$

the balance equation of moment of momentum may finally be given by

$$\int_{B_\alpha} \mathbf{x} \times \underbrace{\left[\mathrm{div}\mathbf{T}^\alpha + \rho^\alpha(\mathbf{b}^\alpha - \mathbf{x}''_\alpha) - \hat{\rho}^\alpha \mathbf{x}'_\alpha + \hat{\mathbf{p}}^\alpha\right]}_{=0} \,\mathrm{dv} = \int_{B_\alpha} \mathbf{I} \times \mathbf{T}^\alpha \,\mathrm{dv} \tag{3.53}$$

in which the balance equation of momentum Eq.(3.47) has been used. As a result, Eq.(3.53) allows for the following conclusion to be drawn in relation to the Cauchy stress tensor

$$\mathbf{T}^\alpha = (\mathbf{T}^\alpha)^\mathrm{T}. \tag{3.54}$$

3.3.4   Balance of Energy

The balance equation of energy, which is commonly known as the first law of thermodynamics, plays a large role in representing the thermo-mechanical effects of porous materials. This is facilitated through the coupling of thermal and mechanical properties. In the equation below, which defines the balance equation of energy with respect to a multiphasic body, the rate of internal energy E^α and kinetic energy K^α is equivalent to the rate of mechanical energy W^α, thermal energy Q^α and the sum of the local energy supply $\hat{e}^\alpha$:

$$(E^\alpha)'_\alpha + (K^\alpha)'_\alpha = W^\alpha + Q^\alpha + \int_{B_\alpha} \hat{e}^\alpha \, dv \tag{3.55}$$

All the components may be defined as follows:

$$E^\alpha = \int_{B_\alpha} \rho^\alpha \hat{\varepsilon}^\alpha \, dv, \quad K^\alpha = \int_{B_\alpha} \frac{1}{2} \rho^\alpha \mathbf{x}'_\alpha \cdot \mathbf{x}'_\alpha \, dv, \tag{3.56}$$

$$W^\alpha = \int_{B_\alpha} \mathbf{x}'_\alpha \cdot \rho^\alpha \mathbf{b}^\alpha \, dv + \int_{B_\alpha} \mathbf{x}'_\alpha \cdot \mathbf{T}^\alpha \, dv, \quad Q^\alpha = \int_{B_\alpha} \rho^\alpha r^\alpha \, dv + \int_{B_\alpha} \mathbf{q}^\alpha \, dv \tag{3.57}$$

Within the above equations, $\hat{\varepsilon}^\alpha$ is the specific internal energy for each constituent, $r^\alpha = r^\alpha(\mathbf{x}, t)$ being the partial energy source and $\mathbf{q}^\alpha = \mathbf{q}^\alpha(\mathbf{x}, t)$ representing the partial heat flux vector. The material time derivative of the components of Eq.(3.56) yield the following:

$$(E^\alpha)'_\alpha = \int_{B_\alpha} \left[\rho^\alpha (\varepsilon^\alpha)'_\alpha + \hat{\rho}^\alpha \varepsilon^\alpha \right] dv, \quad (K^\alpha)'_\alpha = \int_{B_\alpha} (\rho^\alpha \mathbf{x}''_\alpha + \frac{1}{2} \hat{\rho}^\alpha \mathbf{x}'_\alpha) \cdot \mathbf{x}'_\alpha \, dv \tag{3.58}$$

By applying the chain rule and the divergence theorem to Eq.(3.57), Eq.(3.55) may be manipulated to the global form:

$$\int_{B_\alpha} \left[\rho^\alpha (\varepsilon^\alpha)'_\alpha + \hat{\rho}^\alpha \varepsilon^\alpha \right] dv + \int_{B_\alpha} (\rho^\alpha \mathbf{x}''_\alpha + \frac{1}{2} \hat{\rho}^\alpha \mathbf{x}'_\alpha) \cdot \mathbf{x}'_\alpha \, dv$$

$$= \int_{B_\alpha} \left[\mathrm{div}\mathbf{T}^\alpha + \rho^\alpha (\mathbf{b}^\alpha) \cdot \mathbf{x}'_\alpha + \mathbf{T}^\alpha \cdot \mathbf{L}^\alpha \right] dv + \int_{B_\alpha} \left[\rho^\alpha r^\alpha - \mathrm{div}\mathbf{q}^\alpha \right] dv + \int_{B_\alpha} \hat{e}^\alpha \, dv \tag{3.59}$$

or in its local form:

$$\rho^\alpha (\varepsilon^\alpha)'_\alpha + \hat{\rho}^\alpha (\varepsilon^\alpha + \frac{1}{2} \mathbf{x}'_\alpha \cdot \mathbf{x}'_\alpha)$$

$$= \left[\mathrm{div}\mathbf{T}^\alpha + \rho^\alpha (\mathbf{b}^\alpha - \mathbf{x}''_\alpha) \right] \cdot \mathbf{x}'_\alpha + \mathbf{T}^\alpha \cdot \mathbf{L}^\alpha + \rho^\alpha r^\alpha - \mathrm{div}\mathbf{q}^\alpha + \hat{e}^\alpha \tag{3.60}$$

Substituting Eq.(3.47) and by considering the symmetry of Cauchy stress tensor Eq.(3.54), which allows the use of the symmetrical part of the spatial velocity gradient $\mathbf{L}_\alpha$, Eq.(3.60) may be written as

$$\rho^\alpha (\varepsilon^\alpha)'_\alpha - \mathbf{T}^\alpha \cdot \mathbf{L}^\alpha - \rho^\alpha r^\alpha + \mathrm{div}\mathbf{q}^\alpha = \hat{e}^\alpha - \hat{\mathbf{p}}^\alpha \cdot \mathbf{x}'_\alpha - \hat{\rho}^\alpha (\varepsilon^\alpha - \frac{1}{2} \mathbf{x}'_\alpha \cdot \mathbf{x}'_\alpha) \tag{3.61}$$

By summing Eq.(3.60) over all κ constituents, the single phase balance equation of energy is produced:

$$
\begin{aligned}
&\sum_{\alpha=1}^{\kappa} \left[\rho^\alpha (\varepsilon^\alpha)'_\alpha - \mathbf{T}^\alpha \cdot \mathbf{L}^\alpha - \rho^\alpha r^\alpha + \mathrm{div}\mathbf{q}^\alpha \right] \\
&= \sum_{\alpha=1}^{\kappa} \left[\hat{e}^\alpha - \hat{\mathbf{p}}^\alpha \cdot \mathbf{x}'_\alpha - \hat{\rho}^\alpha (\varepsilon^\alpha - \frac{1}{2}\mathbf{x}'_\alpha \cdot \mathbf{x}'_\alpha) \right]
\end{aligned}
\tag{3.62}
$$

With respect to the local energy supply, the following condition needs to be met in order to fulfil *Truesdell's* third metaphysical principle:

$$
\sum_{\alpha=1}^{\kappa} \hat{e}^\alpha \overset{!}{=} 0
\tag{3.63}
$$

In light of the entropy inequality, which will be discussed in the next section, the Helmholtz free energy function will be introduced and cast into the balance equation of energy Eq.(3.61). The Helmholtz free energy function $\psi^\alpha = \psi^\alpha(\mathbf{x}, t)$, and its material time derivative are respectively defined as

$$
\psi^\alpha = \varepsilon^\alpha - \theta^\alpha \eta^\alpha
\tag{3.64}
$$

$$
(\psi^\alpha)'_\alpha = (\varepsilon^\alpha)'_\alpha - \eta^\alpha (\theta^\alpha)'_\alpha - (\eta^\alpha)'_\alpha \theta^\alpha
\tag{3.65}
$$

where $\eta^\alpha = \eta^\alpha(\mathbf{x}, t)$ and $\theta^\alpha = \theta^\alpha(\mathbf{x}, t)$ represent the partial specific entropy and the partial temperature, respectively. Substituting the specific internal energy ε^α and its material time derivative $(\varepsilon^\alpha)'_\alpha$ into Eq.(3.61), and by using Eq.(3.64) and Eq.(3.65), yields the desired local form of the balance equation of energy:

$$
\begin{aligned}
&\rho^\alpha \left[(\psi^\alpha)'_\alpha + \eta^\alpha (\theta^\alpha)'_\alpha + (\eta^\alpha)'_\alpha \theta^\alpha \right] - \mathbf{T}^\alpha \cdot \mathbf{L}^\alpha - \rho^\alpha r^\alpha + \mathrm{div}\mathbf{q}^\alpha \\
&= \hat{e}^\alpha - \hat{\mathbf{p}}^\alpha \cdot \mathbf{x}'_\alpha - \hat{\rho}^\alpha \left[(\psi^\alpha + (\eta^\alpha)'_\alpha \theta^\alpha) - \frac{1}{2}\mathbf{x}'_\alpha \cdot \mathbf{x}'_\alpha \right]
\end{aligned}
\tag{3.66}
$$

3.3.5 Entropy Inequality

The first law of thermodynamics, as discussed in the last section in the form of the balance equation of energy, determines the transfer of energy associated with a thermodynamic system. It doesn't however specify the direction of this transfer. As such, it is the second law of thermodynamics which aims at addressing this matter. The second law of thermodynamics, a concept greatly developed through the works of Clausius [8], is based on the quantity of entropy, and may be expressed in the form of the entropy inequality shown in Eq.(3.67).

$$
\sum_{\alpha=1}^{\kappa} (\mathrm{H}^\alpha)'_\alpha \geq \sum_{\alpha=1}^{\kappa} \left[\int_{\mathrm{B}_\alpha} \frac{1}{\theta^\alpha} \rho^\alpha r^\alpha \, \mathrm{dv} - \int_{\partial \mathrm{B}_\alpha} \frac{1}{\theta^\alpha} \mathbf{q}^\alpha \cdot \mathrm{d}\mathbf{a} \right]
\tag{3.67}
$$

The entropy H^α is expressed as the the volume integral of the specific energy η over the body, of which its derivate may be denoted as follows:

$$
(\mathrm{H}^\alpha)'_\alpha = (\int_{\mathrm{B}_\alpha} \rho^\alpha \eta^\alpha \, \mathrm{dv})'_\alpha = \int_{\mathrm{B}_\alpha} \left[\rho^\alpha (\eta^\alpha)'_\alpha + \hat{\rho}^\alpha \eta^\alpha \right] \, \mathrm{dv}
\tag{3.68}
$$

Applying the divergence theorem on the surface integral term within Eq.(3.67) and inserting Eq.(3.68), leads to

$$m \sum_{\alpha=1}^{\kappa} \int_{B_\alpha} \left[\rho^\alpha (\eta^\alpha)'_\alpha + \hat{\rho}^\alpha \eta^\alpha \right] \, dv \geq \sum_{\alpha=1}^{\kappa} \int_{B_\alpha} \left[\frac{1}{\theta^\alpha} \rho^\alpha r^\alpha - \text{div} \left(\frac{1}{\theta^\alpha} \mathbf{q}^\alpha \right) \right] \, dv \qquad (3.69)$$

Rearranging the local balance equation of energy Eq.(3.66) with respect to $\rho^\alpha r^\alpha$ and after simplification the following is yielded:

$$\sum_{\alpha=1}^{\kappa} \frac{1}{\theta^\alpha} \{ -\rho^\alpha ((\psi^\alpha)'_\alpha + \eta^\alpha (\theta^\alpha)'_\alpha) - \hat{\rho}^\alpha (\psi^\alpha - \frac{1}{2} \mathbf{x}'_\alpha \cdot \mathbf{x}'_\alpha) + \mathbf{T}^\alpha \cdot \mathbf{D}^\alpha$$

$$+ \hat{e}^\alpha - \hat{\mathbf{p}}^\alpha \cdot \mathbf{x}'_\alpha - \frac{1}{\theta^\alpha} \mathbf{q}^\alpha \text{grad} \theta^\alpha \} \geq 0 \qquad (3.70)$$

Chapter 4

Constitutive Modelling for a Triphasic System

So far in Chapter 3, the application of TPM was addressed in a general basis that could facilitate a broad scope of problems in relation to the number of constituents and kinematic properties, for example. In order to create a TPM framework needed for this study an adaptation of the mechanical and thermodynamic balance equations, encountered in Sec.(3.3), will be performed. As such, specific assumptions will be applied to the balance equations in order to capture the physiological features of the human heart.

In relation to a cardiac and triphasic TPM model, three phases will be incorporated which will include a solid, liquid and nutrient phase. The solid phase φ^{S} will represent the cardiac tissue, and the liquid φ^{L} and nutrient φ^{N} phases will represent the blood saturating the pores of the solid tissue and the various biochemical constituents contained in the blood which are involved in the processes of growth and remodelling, respectively. Even though there are a vast number biochemical components involved in tissue growth, such as the role of hormones in mechanotransduction [44], the inclusion of these is beyond the scope of this study. As such, it makes sense to lump these components into one nutrient constituent in order to simplify the problem.

4.1   Model Assumptions

For the case of the human heart comprising of a porous solid skeleton saturated with blood, material incompressibility may be assumed for the entire system, of which is analogous with literature regarding the nature of biological tissue [58]. This results in all constituents being treated as incompressible. The real densities of the phases would therefore remain constant, however, the partial densities would still be subject to change in relation to changes in volume fractions. As a result, for the triphasic model the following relations are valid:

$$\rho^{\alpha\mathrm{R}} = \rho_{0\alpha}^{\alpha\mathrm{R}} = \text{const.}, \quad \left(\rho^{\alpha\mathrm{R}}\right)'_{\alpha} = 0 \tag{4.1}$$

The mass supply function for the nutrient phase $\hat{\rho}^{\mathrm{N}}$ accounts for the increase in mass of the solid phase and an equivalent reduction in mass of the nutrient phase. Mass exchange is included solely between the nutrient and solid phase, whereby the rate of change of density for the liquid phase is assumed to be negligible. Hence, the mass supply functions may be defined as

$$\hat{\rho}^{\mathrm{N}} = -\hat{\rho}^{\mathrm{S}}, \quad \hat{\rho}^{\mathrm{L}} = 0 \tag{4.2}$$

From Sec.(3.2) it was deduced that all constituents may have independent motions. However, in relation to the liquid and nutrient phases, they are both assumed to be contained within the blood. Hence, this allows for simplification of the motion functions between the aforementioned phases. The motion function of the nutrient phase $\mathcal{X}_N(\mathbf{X}_N, t)$ would thus be equivalent to that of the liquid phase $\mathcal{X}_L(\mathbf{X}_L, t)$. As a result, the motion functions of the liquid and nutrient phases will hence be represented in terms of a general fluid phase $\mathcal{X}_F(\mathbf{X}_F, t)$, as shown below:

$$\mathcal{X}_L(\mathbf{X}_L, t) = \mathcal{X}_N(\mathbf{X}_N, t) = \mathcal{X}_F(\mathbf{X}_F, t) \tag{4.3}$$

This assumption furthermore renders the spatial velocities for the liquid and nutrient phases as equivalent, such that

$$\mathbf{x}'_L(\mathbf{x}, t) = \mathbf{x}'_N(\mathbf{x}, t) = \mathbf{x}'_F(\mathbf{x}, t) \tag{4.4}$$

In addition, all body forces will be neglected and a quasi-static approach will be adopted, which results in all acceleration terms for the phases to be ignored:

$$\mathbf{b} = \mathbf{0}, \quad \mathbf{x}''_\alpha = \mathbf{0} \tag{4.5}$$

Furthermore, the mass exchange term which contributes to momentum, shown in Eq.(3.47), will be neglected due to the insignificant amount of momentum generated from the exchange of mass between the phases:

$$\hat{\rho}^\alpha \mathbf{x}'_\alpha = \mathbf{0} \tag{4.6}$$

The temperature difference between all the phases will be treated as negligible, as it is assumed that there is no differential temperatures within the saturated tissue comprising of the solid skeleton and blood. Hence this allows a uniform temperature and flux distribution:

$$\theta^\alpha = \theta = \text{const.}, \quad \mathbf{q}^\alpha = \mathbf{q} = \text{const.} \tag{4.7}$$

4.2 Adaptation of the Balance Equations

Considering the assumptions and restriction of mass supply terms presented in Sec.(4.1) the balance of mass and momentum, shown in Sec.(3.3.1) and (3.3.2) respectively, may be adapted to form the field equations required to model the proliferative process of growth and remodelling of cardiac tissue. Starting with the balance equation of mass, the local form of Eq.(3.41) may be rewritten in the form shown below for all constituents:

$$\left(n^\alpha \rho^{\alpha R}\right)'_\alpha + n^\alpha \rho^{\alpha R} \text{div} \mathbf{x}'_\alpha = \hat{\rho}^\alpha \tag{4.8}$$

Making use of Eq.(4.1)$_2$, the chain rule and the condition $\text{div}\mathbf{x}'_\alpha = \mathbf{D}_\alpha : \mathbf{I}$, Eq.(4.8) may be written as

$$\left(n^\alpha\right)'_\alpha + n^\alpha \mathbf{D}_\alpha : \mathbf{I} = \frac{\hat{\rho}^\alpha}{\rho^{\alpha R}}, \tag{4.9}$$

which may be further displayed for each constituent φ^α

$$\left(n^S\right)'_S + n^S \mathbf{D}_S : \mathbf{I} = \frac{\hat{\rho}^S}{\rho^{SR}}, \quad \left(n^L\right)'_L + n^L \mathbf{D}_L : \mathbf{I} = 0 \quad \left(n^N\right)'_N + n^N \mathbf{D}_N : \mathbf{I} = \frac{\hat{\rho}^N}{\rho^{NR}}, \tag{4.10}$$

such that the mass supply term for the liquid phase is neglected. The adapted forms of the balance equations of momentum for the mixture and for each constituent yields

$$\text{div}\mathbf{T}^{\text{SLN}} = \mathbf{0}, \quad \text{div}\mathbf{T}^{\text{S}} + \hat{\mathbf{p}}^{\text{S}} = \mathbf{0}$$
$$\text{div}\mathbf{T}^{\text{L}} + \hat{\mathbf{p}}^{\text{L}} = \mathbf{0}, \quad \text{div}\mathbf{T}^{\text{N}} + \hat{\mathbf{p}}^{\text{N}} = \mathbf{0}$$
(4.11)

whereby the sum of the interaction forces $\hat{\mathbf{p}}^{\alpha}$ is zero and the abbreviation $\mathbf{T}^{\text{SLN}}$ represents the sum of the Cauchy stress tensor's of each constituent.

4.3   Adaptation of the Entropy Inequality

Unlike the theory of mixtures, which is a closed framework that has an equivalent amount of unknowns and field equations, the theory of porous media differs in the sense that it is constrained by the saturation condition, which stems from the volume fractions concept, see Sec.(3.1). This results in an additional field equation. Therefore an additional scalar quantity needs to be introduced in the form the *Lagrange multiplier* λ, which may be interpreted as a type of reaction force [58].

The Lagrange multiplier is introduced as a quantity by means of the entropy inequality. This results in the first adaptation made to the entropy inequality, which makes use of the material time derivative of the saturation condition:

$$\left(n^{\text{S}} + n^{\text{L}} + n^{\text{N}}\right)'_{\text{S}} = 0$$
(4.12)

The material time derivative of the saturation condition is zero due to the fact that the theory of porous media employs a closed thermodynamic framework. This therefore provides a platform for the inclusion of the Lagrange multiplier through multiplication with Eq.(4.12):

$$\lambda \left(n^{\text{S}} + n^{\text{L}} + n^{\text{N}}\right)'_{\text{S}} = 0$$
(4.13)

Equation (4.13) may be simplified further by firstly evaluating the material time derivative of the liquid volume fraction with respect to the solid motion:

$$\left(n^{\text{L}}\right)'_{\text{S}} = \frac{\partial n^{\text{L}}}{\partial t} + \frac{\partial n^{\text{L}}}{\partial \mathbf{x}_{\text{S}}}\frac{\partial \mathbf{x}_{\text{S}}}{\partial t} = \dot{n}^{\text{L}} + \text{grad}\, n^{\text{L}} \cdot \mathbf{x}'_{\text{S}}$$
(4.14)

Similarly, the material time derivative of the liquid volume fraction may be determined with respect the liquid phase:

$$\left(n^{\text{L}}\right)'_{\text{L}} = \dot{n}^{\text{L}} + \text{grad}\, n^{\text{L}} \cdot \mathbf{x}'_{\text{L}}$$
(4.15)

By rearranging Eq.(4.14) and Eq.(4.15) and equating them to each other, the following equation is produced:

$$\left(n^{\text{L}}\right)'_{\text{S}} = \left(n^{\text{L}}\right)'_{\text{L}} - \text{grad}\, n^{\text{L}} \cdot \left(\mathbf{x}'_{\text{L}} - \mathbf{x}'_{\text{S}}\right) = \left(n^{\text{L}}\right)'_{\text{L}} - \text{grad}\, n^{\text{L}} \cdot \mathbf{w}_{\text{LS}}$$
(4.16)

where $\mathbf{w}_{\text{LS}}$ is the relative velocity between the liquid and solid, namely the *seepage velocity*. Equations (4.14) to (4.16) may be solved for using the nutrient volume fraction, which similarly leads to

$$\left(n^{\text{N}}\right)'_{\text{S}} = \left(n^{\text{N}}\right)'_{\text{N}} - \text{grad}\, n^{\text{N}} \cdot \mathbf{w}_{\text{NS}}$$
(4.17)

By substituting Eq.(4.16) and Eq.(4.17) in Eq.(4.13) and by noting that $\mathbf{w}_{\text{LS}} = \mathbf{w}_{\text{NS}} = \mathbf{w}_{\text{FS}}$ (see Eq.(4.4)), the final form of Eq.(4.13) required for the entropy inequality is

determined:

$$\lambda \left[\left(n^S \right)_S' + \left(n^L \right)_L' + \left(n^N \right)_N' - \mathbf{w}_{FS} \cdot \left(\operatorname{grad} n^L + \operatorname{grad} n^N \right) \right] = 0 \qquad (4.18)$$

The second addition to the entropy inequality also comes in the form of a Lagrange multiplier, introduced for each constituent through the balance of mass from Eq.(4.9):

$$\lambda^\alpha \left[\left(n^\alpha \right)_\alpha' + n^\alpha \mathbf{D}_\alpha : \mathbf{I} - \frac{\hat{\rho}^\alpha}{\rho^{\alpha R}} \right] = 0 \qquad (4.19)$$

The modification of the entropy inequality through the addition of the terms presented in Eq.(4.18) and Eq.(4.19) will hence result in an adequate equation system that includes a sufficient amount of unknown variables. The entropy inequality and the Lagrange multipliers will be further elaborated on in the following section.

4.4 Evaluation of the Entropy Inequality

With the addition of the Lagrange multiplier λ the set of unknown variables may now be represented by

$$\mathcal{U} = \left\{ \mathbf{u}_S, \, n^S, \, n^N, \lambda \right\} \qquad (4.20)$$

Noting that the liquid volume fraction may be determined through the saturation condition. The constitutive quantities may be defined as

$$\mathcal{C} = \left\{ \mathbf{T}^\alpha, \, \hat{\mathbf{p}}^S, \, \hat{\mathbf{p}}^L, \, \hat{\rho}^S \right\} \qquad (4.21)$$

Noting that further assumptions need to be implemented in order to close the equation system. Considering the treatment of the entropy inequality in analogy to Coleman and Noll [10] the set of free process variables are chosen:

$$\mathcal{P} = \left\{ \mathbf{C}_S, \, J_L, \, J_N, \, n^\alpha, \, \mathbf{w}_{FS}, \, \operatorname{grad} n^L, \, \operatorname{grad} n^N \right\} \qquad (4.22)$$

The dependencies of the the Helmholtz free energy functions are as follows:

$$\psi^S = \psi^S \left\{ \mathbf{C}_{Se}, \, n^S \right\}, \quad \psi^L = \psi^L \left\{ J_L, \, n^L \right\}, \quad \psi^N = \psi^N \left\{ J_N, \, n^N \right\} \qquad (4.23)$$

For later use, the term $\rho^\alpha (\psi^\alpha)_\alpha'$ in Eq.(3.70) will be substituted with the following expressions for each constituent:

$$
\begin{aligned}
\rho^S (\psi^S)_S' &= 2 n^S \rho^{SR} \mathbf{F}_S \frac{\partial \psi^S}{\partial \mathbf{C}_S} \mathbf{F}_S^T : \mathbf{D}_S + n^S \rho^{SR} \frac{\partial \psi^S}{\partial n^S} \left(n^S \right)_S', \\
\rho^L (\psi^L)_L' &= n^L \rho^{LR} J_L \frac{\partial \psi^L}{\partial J_L} \mathbf{I} : \mathbf{D}_L + n^L \rho^{LR} \frac{\partial \psi^L}{\partial n^L} \left(n^L \right)_L', \\
\rho^N (\psi^N)_N' &= n^N \rho^{NR} J_N \frac{\partial \psi^N}{\partial J_N} \mathbf{I} : \mathbf{D}_N + n^N \rho^{NR} \frac{\partial \psi^N}{\partial n^N} \left(n^N \right)_N'
\end{aligned} \qquad (4.24)
$$

with the identity $(J^\alpha)_\alpha' = J^\alpha \mathbf{I} : \mathbf{D}_\alpha$ being used.

In addition, regarding the composition of the entropy inequality which will be shown in the following equation, lumping of the nutrient and liquid phases into a general fluid phase will be done in order to simplify the expressions. As such, the following relationships will be used:

$$\varphi^L + \varphi^N = \varphi^F, \quad n^L + n^N = n^F, \quad \hat{\mathbf{p}}^L + \hat{\mathbf{p}}^N = \hat{\mathbf{p}}^F \qquad (4.25)$$

As stated in Sec.(4.3) the methods used to create a closed equation system have been linked to the entropy inequality through addition of the material time derivative of the saturation condition Eq.(4.10) and the balance equation of mass Eq.(4.11), both multiplied with the respective Lagrange multipliers. The expanded form of the entropy inequality from Eq.(3.70), coupled with Eq.(4.10) and Eq.(4.11), may be written as follows:

$$\mathbf{D}_{\mathrm{S}} \cdot \left\{ \mathbf{T}^{\mathrm{S}} - 2\mathrm{n}^{\mathrm{S}}\rho^{\mathrm{SR}}\mathbf{F}_{\mathrm{S}}\frac{\partial\psi^{\mathrm{S}}}{\partial\mathbf{C}_{\mathrm{S}}}\mathbf{F}_{\mathrm{S}}^{\mathrm{T}} + \lambda^{\mathrm{S}}\mathrm{n}^{\mathrm{S}}\mathbf{I} \right\} + \mathbf{D}_{\mathrm{L}} \cdot \left\{ \mathbf{T}^{\mathrm{L}} - \mathrm{n}^{\mathrm{L}}\rho^{\mathrm{LR}}\mathrm{J}_{\mathrm{L}}\frac{\partial\psi^{\mathrm{L}}}{\partial\mathrm{J}_{\mathrm{L}}}\mathbf{I} + \lambda^{\mathrm{L}}\mathrm{n}^{\mathrm{L}}\mathbf{I} \right\}$$

$$+\mathbf{D}_{\mathrm{N}} \cdot \left\{ \mathbf{T}^{\mathrm{N}} - \mathrm{n}^{\mathrm{N}}\rho^{\mathrm{NR}}\mathrm{J}_{\mathrm{N}}\frac{\partial\psi^{\mathrm{N}}}{\partial\mathrm{J}_{\mathrm{N}}}\mathbf{I} + \lambda^{\mathrm{N}}\mathrm{n}^{\mathrm{N}}\mathbf{I} \right\} - \left(\mathrm{n}^{\mathrm{S}}\right)'_{\mathrm{S}}\left\{ \lambda - \lambda^{\mathrm{S}} + \mathrm{n}^{\mathrm{S}}\rho^{\mathrm{SR}}\frac{\partial\psi^{\mathrm{S}}}{\partial\mathrm{n}^{\mathrm{S}}} \right\}$$

$$- \left(\mathrm{n}^{\mathrm{L}}\right)'_{\mathrm{L}}\left\{ \lambda - \lambda^{\mathrm{L}} + \mathrm{n}^{\mathrm{L}}\rho^{\mathrm{LR}}\frac{\partial\psi^{\mathrm{L}}}{\partial\mathrm{n}^{\mathrm{L}}} \right\} - \left(\mathrm{n}^{\mathrm{N}}\right)'_{\mathrm{N}}\left\{ \lambda - \lambda^{\mathrm{N}} + \mathrm{n}^{\mathrm{N}}\rho^{\mathrm{NR}}\frac{\partial\psi^{\mathrm{N}}}{\partial\mathrm{n}^{\mathrm{N}}} \right\}$$

$$-\hat{\rho}^{\mathrm{N}}\left\{ \left(\psi^{\mathrm{N}} - \frac{1}{2}\mathbf{x}'_{\mathrm{F}} \cdot \mathbf{x}'_{\mathrm{F}} + \frac{\lambda^{\mathrm{N}}}{\rho^{\mathrm{NR}}} \right) - \left(\psi^{\mathrm{S}} - \frac{1}{2}\mathbf{x}'_{\mathrm{S}} \cdot \mathbf{x}'_{\mathrm{S}} + \frac{\lambda^{S}}{\rho^{\mathrm{SR}}} \right) \right\}$$

$$-\mathbf{w}_{\mathrm{FS}} \cdot \left\{ \hat{\mathbf{p}}^{\mathrm{F}} - \lambda\mathrm{grad}\,\mathrm{n}^{\mathrm{F}} \right\} \geq 0$$

(4.26)

In compliance with standard procedure, the entropy inequality should be satisfied for an arbitrary set of process variables $\mathcal{P}$, as stated in Eq.(4.22). The parts of the entropy inequality which contain fixed variables and derivatives of the terms in $\mathcal{P}$ are energy preserving and may be deemed the free available quantities, of which comprise of

$$\mathcal{A} = \left\{ \mathbf{D}_{\alpha},\ (\mathrm{n}^{\alpha})'_{\alpha} \right\} \tag{4.27}$$

The rest of the parts of Eq.(4.26) which contain values of $\mathcal{P}$ contribute to the dissipative mechanism, and are hence non energy preserving and greater than zero. All terms which comprise of the free available quantities do not add to the dissipation and are therefore assumed to be equal to zero. As such, according to Ricken and Bluhm [58] the entropy inequality may be fulfilled if the following structure is observed:

$$\mathbf{D}_{\mathrm{S}} \cdot \underbrace{\{(...)\}}_{=0} + \mathbf{D}_{\mathrm{L}} \cdot \underbrace{\{(...)\}}_{=0} + \mathbf{D}_{\mathrm{N}} \cdot \underbrace{\{(...)\}}_{=0}$$
$$- \left(\mathrm{n}^{\mathrm{S}}\right)'_{\mathrm{S}} \underbrace{\{(...)\}}_{=0} - \left(\mathrm{n}^{\mathrm{L}}\right)'_{\mathrm{L}} \underbrace{\{(...)\}}_{=0} - \left(\mathrm{n}^{\mathrm{N}}\right)'_{\mathrm{N}} \underbrace{\{(...)\}}_{=0} + \underbrace{\mathcal{D}is}_{\geq 0} \geq 0 \tag{4.28}$$

The dissipation mechanism may hence be written as

$$\mathcal{D}is = -\hat{\rho}^{\mathrm{N}}\left\{ \left(\psi^{\mathrm{N}} - \frac{1}{2}\mathbf{x}'_{\mathrm{F}} \cdot \mathbf{x}'_{\mathrm{F}} + \frac{\lambda^{\mathrm{N}}}{\rho^{\mathrm{NR}}} \right) - \left(\psi^{\mathrm{S}} - \frac{1}{2}\mathbf{x}'_{\mathrm{S}} \cdot \mathbf{x}'_{\mathrm{S}} + \frac{\lambda^{S}}{\rho^{\mathrm{SR}}} \right) \right\}$$
$$-\mathbf{w}_{\mathrm{FS}} \cdot \left\{ \hat{\mathbf{p}}^{\mathrm{F}} - \lambda\mathrm{grad}\,\mathrm{n}^{\mathrm{F}} \right\} \geq 0 \tag{4.29}$$

Using the the expressions containing the free available quantities $\mathcal{A}$ in Eq.(4.26) results in the formulation of the Lagrange multipliers associated with the balance of mass λ^{α}:

$$\lambda^{\alpha} = \lambda + \mathrm{n}^{\alpha}\rho^{\alpha\mathrm{R}}\frac{\partial\psi^{\alpha}}{\partial\mathrm{n}^{\alpha}} \tag{4.30}$$

the Cauchy stress tensors may be defined as follows:

$$\mathbf{T}^{\mathrm{S}} = 2\mathrm{n}^{\mathrm{S}}\rho^{\mathrm{SR}}\mathbf{F}_{\mathrm{S}}\frac{\partial\psi^{\mathrm{S}}}{\partial\mathbf{C}_{\mathrm{S}}}\mathbf{F}_{\mathrm{S}}^{\mathrm{T}} - \lambda\mathrm{n}^{\mathrm{S}}\mathbf{I} - \left(\mathrm{n}^{\mathrm{S}}\right)^{2}\rho^{\mathrm{SR}}\frac{\partial\psi^{\mathrm{S}}}{\partial\mathrm{n}^{\mathrm{S}}}\mathbf{I},$$

$$\mathbf{T}^{\mathrm{L}} = \mathrm{n}^{\mathrm{L}}\rho^{\mathrm{LR}}\mathrm{J}_{\mathrm{L}}\frac{\partial\psi^{\mathrm{L}}}{\partial\mathrm{J}_{\mathrm{L}}}\mathbf{I} - \lambda\mathrm{n}^{\mathrm{L}}\mathbf{I} - \left(\mathrm{n}^{\mathrm{L}}\right)^{2}\rho^{\mathrm{LR}}\frac{\partial\psi^{\mathrm{L}}}{\partial\mathrm{n}^{\mathrm{L}}}\mathbf{I}, \tag{4.31}$$

$$\mathbf{T}^{\mathrm{N}} = \mathrm{n}^{\mathrm{N}}\rho^{\mathrm{NR}}\mathrm{J}_{\mathrm{N}}\frac{\partial\psi^{\mathrm{N}}}{\partial\mathrm{J}_{\mathrm{N}}}\mathbf{I} - \lambda\mathrm{n}^{\mathrm{N}}\mathbf{I} - \left(\mathrm{n}^{\mathrm{N}}\right)^{2}\rho^{\mathrm{NR}}\frac{\partial\psi^{\mathrm{N}}}{\partial\mathrm{n}^{\mathrm{N}}}\mathbf{I}$$

which are extracted using Eq.(4.26) and Eq.(4.30). Regarding the dissipation mechanism, the following condition should be applied to the interaction force of the lumped fluid phase $\mathbf{p}^{\mathrm{F}}$ and the nutrient mass supply function $\hat{\rho}^{\mathrm{N}}$, in order to result in a valid entropy inequality:

$$\hat{\mathbf{p}}^{\mathrm{F}} = \lambda\mathrm{grad}\,\mathrm{n}^{\mathrm{F}} - \mathbf{S}^{\mathrm{F}}\mathbf{w}_{\mathrm{FS}}, \quad \hat{\rho}^{\mathrm{N}} = \delta^{\mathrm{N}}(\Psi^{\mathrm{S}} - \Psi^{\mathrm{N}}) \tag{4.32}$$

where the terms $\mathbf{S}^{\mathrm{F}}$ and $(\Psi^{\mathrm{S}} - \Psi^{\mathrm{N}})$ are defined as

$$\mathbf{S}^{\mathrm{F}} = \alpha_{\mathrm{F0}}\left[\alpha_{\mathrm{F1}}\mathbf{I} + (1 - \alpha_{\mathrm{F1}})\mathbf{M}\right]^{-1} + \alpha_{\mathrm{F2}}\mathbf{I},$$

$$\Psi^{\mathrm{S}} - \Psi^{\mathrm{N}} = \left(\psi^{\mathrm{S}} - \frac{1}{2}\mathbf{x}_{\mathrm{S}}' \cdot \mathbf{x}_{\mathrm{S}}' + \frac{\lambda^{S}}{\rho^{\mathrm{SR}}}\right) - \left(\psi^{\mathrm{N}} - \frac{1}{2}\mathbf{x}_{\mathrm{F}}' \cdot \mathbf{x}_{\mathrm{F}}' + \frac{\lambda^{N}}{\rho^{\mathrm{NR}}}\right) \tag{4.33}$$

with $\mathbf{M}$ being a positive structural tensor. In addition, the scaling parameters δ^{N} and $\alpha_{\mathrm{F}\{0,1,2\}}$ need to be greater than or equal to zero in order to fulfil the entropy inequality conditions [58].

4.4.1 Stress

The Cauchy stress tensors shown in Eq.(4.31) may be modified by applying certain assumptions (see [58]), such as

$$\frac{\partial\psi^{\mathrm{L}}}{\partial\mathrm{n}^{\mathrm{L}}} = \frac{\partial\psi^{\mathrm{N}}}{\partial\mathrm{n}^{\mathrm{N}}} = 0, \quad \frac{\partial\psi^{\mathrm{L}}}{\partial\mathrm{J}_{\mathrm{L}}} = \frac{\partial\psi^{\mathrm{N}}}{\partial\mathrm{J}_{\mathrm{N}}} = 0 \tag{4.34}$$

In addition, the Cauchy stress tensor for the solid phase is also postulated to depend on the derivative of ψ_{S} with respect to the deformation (represented through the right Cauchy green tensor $\mathbf{C}_{\mathrm{S}}$) and the solid volume fraction n^{S}. However going forward, the dependence of $\mathbf{T}^{\mathrm{S}}$ on the solid volume fraction will be neglected [80]. By adding the Cauchy stress tensor's of the liquid and nutrient phases and by taking into account the aforementioned assumptions, the following is yielded:

$$\mathbf{T}^{\mathrm{S}} = 2\mathrm{n}^{\mathrm{S}}\rho^{\mathrm{SR}}\mathbf{F}_{\mathrm{S}}\frac{\partial\psi^{\mathrm{S}}}{\partial\mathbf{C}_{\mathrm{S}}}\mathbf{F}_{\mathrm{S}}^{\mathrm{T}} - \lambda\mathrm{n}^{\mathrm{S}}\mathbf{I} = \mathbf{T}_{\mathrm{E}}^{\mathrm{S}} - \lambda\mathrm{n}^{\mathrm{S}}\mathbf{I}, \quad \mathbf{T}^{\mathrm{F}} = \mathbf{T}^{\mathrm{L}} + \mathbf{T}^{\mathrm{N}} = -\lambda\mathrm{n}^{\mathrm{F}}\mathbf{I} \tag{4.35}$$

with $\mathbf{T}_{\mathrm{E}}^{\mathrm{S}}$ representing the effective solid Cauchy stress, and with the relationships of the fluid constituent Eq.(4.25) being used.

The total Cauchy stress tensor, which is obtained through addition of $\mathbf{T}^{\mathrm{S}}$ and $\mathbf{T}^{\mathrm{F}}$, is given by

$$\mathbf{T} = \mathbf{T}_{\mathrm{E}}^{\mathrm{S}} - \lambda\mathbf{I} \tag{4.36}$$

Consequently, the first and second Piola-Kirchhoff stress tensors may be respectively given by

$$\mathbf{S} = \mathrm{J}_{\mathrm{S}}\mathbf{F}_{\mathrm{S}}^{-1}\mathbf{T}\mathbf{F}_{\mathrm{S}}^{\mathrm{T}-1}, \quad \mathbf{P} = \mathbf{F}_{\mathrm{S}}\mathbf{S} \tag{4.37}$$

In Chapter 5 the strain energy function of the solid constituent will be postulated as being a function of the elastic Cauchy green tensor $\mathbf{C}_{\mathrm{Se}}$. In order to preserve the dependency in terms of $\mathbf{C}_{\mathrm{S}}$, the following formulation is used: [80]

$$\mathbf{C}_{\mathrm{Se}} = \mathbf{F}_{\mathrm{Sg}}^{\mathrm{T\text{-}1}} \mathbf{C}_{\mathrm{S}} \mathbf{F}_{\mathrm{Sg}}^{-1} \tag{4.38}$$

4.4.2 Filter Velocity and Permeability

The motions of the solid and fluid phases are related to the interaction forces via $\hat{\mathbf{p}}^{\mathrm{F}} = -\hat{\mathbf{p}}^{\mathrm{S}}$. The expanded expression of $\hat{\mathbf{p}}^{\mathrm{F}}$, shown in Eq.(4.32), with inclusion of Eq.(4.33), results in

$$\hat{\mathbf{p}}^{\mathrm{F}} = \lambda \mathrm{grad}\, n^{\mathrm{F}} - \alpha_{\mathrm{F0}} \left[\alpha_{\mathrm{F1}} \mathbf{I} + (1 - \alpha_{\mathrm{F1}}) \mathbf{M} \right]^{-1} \cdot \mathbf{w}_{\mathrm{FS}} \tag{4.39}$$

where α_{F2} is set to zero. As stated, $\mathbf{M}$ is a second order tensor which is related to the fibre direction of the cardiac tissue $\mathbf{f}$ in the spatial configuration and may also be expressed as $\mathbf{f} \otimes \mathbf{f}$. α_{F1} is the parameter which dictates the level of isotropy of the flow, and ranges from fully isotropic when $\alpha_{\mathrm{F1}} = 1$ to the transversely isotropic state where $\alpha_{\mathrm{F1}} = 0$. By adding the liquid and nutrient balance of momentum equations to each other, to form the fluid balance of momentum, and by substituting Eq.(4.39) and the equation for the fluid Cauchy stress tensor Eq.(4.35)$_2$, the following is produced

$$\mathrm{div}\left(-\lambda n^{\mathrm{F}} \mathbf{I}\right) + \lambda \mathrm{grad}\, n^{\mathrm{F}} - \alpha_{\mathrm{F0}} \mathbf{M}^{-1} \cdot \mathbf{w}_{\mathrm{FS}} = \mathbf{0} \tag{4.40}$$

assuming a transversely isotropic state. Rearranging Eq.(4.40) and by using the relation

$$\mathrm{div}\left(-\lambda n^{\mathrm{F}} \mathbf{I}\right) = -\lambda \mathrm{grad}\, n^{\mathrm{F}} - n^{\mathrm{F}} \mathrm{grad}\, \lambda \tag{4.41}$$

results in the expression of the filter velocity $n^{\mathrm{F}} \mathbf{w}_{\mathrm{FS}}$

$$n^{\mathrm{F}} \mathbf{w}_{\mathrm{FS}} = \frac{\left(n^{\mathrm{F}}\right)^2}{\alpha_{\mathrm{F0}}} \mathbf{M} \mathrm{grad}\, \lambda \tag{4.42}$$

Transferring the filter velocity to the reference configuration using the relations

$$n^{\mathrm{F}} \mathbf{w}_{\mathrm{FS0}} = n^{\mathrm{F}} J_{\mathrm{S}} \mathbf{F}_{\mathrm{S}}^{-1} \mathbf{w}_{\mathrm{FS}}, \quad \mathbf{M} = \mathbf{F}_{\mathrm{S}} \mathbf{M}_0 \mathbf{F}_{\mathrm{S}}^{\mathrm{T}}, \quad \mathrm{grad}\, \lambda = \mathrm{Grad}\, \lambda \mathbf{F}_{\mathrm{S}}^{-1} \tag{4.43}$$

results in

$$n^{\mathrm{F}} \mathbf{w}_{\mathrm{FS0}} = \frac{\left(n^{\mathrm{F}}\right)^2}{\alpha_{\mathrm{F0}}} J_{\mathrm{S}} \mathbf{M}_0 \mathrm{Grad}\, \lambda \tag{4.44}$$

In order to characterize the parameter α_{F0} the following relationships which involve either, the initial Darcy permeability $k_{0\mathrm{S}}^{\mathrm{F}}(\mathrm{m/s})$ and the specific weight $\gamma^{\mathrm{FR}}(\mathrm{N/m}^3)$ or the intrinsic solid permeability $k_{0\mathrm{S}}^{\mathrm{F}}(\mathrm{m}^2)$ and the effective shear viscosity $\mu^{\mathrm{FR}}(\mathrm{Ns/m}^2)$, may be applied such that

$$\frac{\left(n^{\mathrm{F}}\right)^2}{\alpha_{\mathrm{F0}}} = \left(\frac{n^{\mathrm{F}}}{1 - n_{0\mathrm{S}}^{\mathrm{S}}}\right)^m \frac{k_{0\mathrm{S}}^{\mathrm{F}}}{\gamma^{\mathrm{FR}}} = \left(\frac{n^{\mathrm{F}}}{1 - n_{0\mathrm{S}}^{\mathrm{S}}}\right)^m \frac{k_{0\mathrm{S}}^{\mathrm{F}}}{\mu^{\mathrm{FR}}} \tag{4.45}$$

where m is a dimensionless constant, see also Eipper [18], Ricken [58], Ehlers et al. [15] and the citations therein.

4.4.3 Mass Supply and Kinematics of Growth

The proposed method of representing growth proliferation in cardiac tissue is based on that presented in the work of Werner [80]. This growth evolution model will hence be combined with a strain driven growth law, developed by Goktepe et al. [20], in order to model the condition of dilated cardiomyopathy, DCM. Starting with the balance equation of mass for the solid phase

$$(\rho^S)'_S + \rho^S \mathrm{div}\, \mathbf{x}'_S = \hat{\rho}^S \tag{4.46}$$

where the relation $J_S \, \mathrm{div}\, \mathbf{x}'_S = (J_S)'_S$, may be substituted in (4.46), which results in

$$\frac{\partial \rho^S}{\partial t} + \rho^S \frac{1}{J_S} \frac{\partial J_S}{\partial t} = \hat{\rho}^S \tag{4.47}$$

$$\rightarrow \frac{1}{\rho^S}\left(\partial \rho^S - \hat{\rho}^S \partial t\right) = -\frac{1}{J_S}\partial J_S \tag{4.48}$$

$$\rightarrow \ln \rho^S - \int \frac{\hat{\rho}^S}{\rho^S}dt = \ln \frac{1}{J_S} + \ln c = \ln \frac{c}{J_S} \tag{4.49}$$

with c being the constant of integration

$$\frac{c}{J_S} = \rho^S \exp\left(-\int \frac{\hat{\rho}^S}{\rho^S}dt\right) \tag{4.50}$$

At the beginning of the cardiac cycle, at time t_0, during which the heart is at rest and there is no deformation (hence $J_S = 1$), no change in density ($\rho^S = \rho^S_{0S}$), and no growth ($\hat{\rho}^S = 0$), the constant of integration c is found to equate to: $c = \rho^S_{0S}$. As such, Eq. (4.49), may be rewritten as

$$J_S = \underbrace{\frac{\rho^S_{0S}}{\rho^S}}_{J_{Se}} \underbrace{\exp\left(\int \frac{\hat{\rho}^S}{\rho^S}dt\right)}_{J_{Sg}} \tag{4.51}$$

with the growth part being

$$J_{Sg} = \exp\left(\int \frac{\hat{\rho}^S}{\rho^S}dt\right) \tag{4.52}$$

Using a finite difference approximation, and by discretising the equation above with respect to the nth and $(n+1)^{th}$ time step:

$$J_{Sg}^{n+1} = \underbrace{\exp\left(\sum_{n=1}^{n}\left(\frac{\hat{\rho}^S}{\rho^S}\right)^n \Delta t^n\right)}_{J_{Sg}^n} \cdot \underbrace{\exp\left(\left(\frac{\hat{\rho}^S}{\rho^S}\right)^{n+1} \Delta t^{n+1}\right)}_{\Delta J_{Sg}^{n+1}} \tag{4.53}$$

J_{Sg} may be updated every iteration via the following equation:

$$J_{Sg}^{n+1} = J_{Sg}^n \Delta J_{Sg}^{n+1} \tag{4.54}$$

The mass supply function $\hat{\rho}^S$ is postulated by

$$\hat{\rho}^S = \hat{\rho}^{max}\hat{\rho}^{lim} \tag{4.55}$$

where $\hat{\rho}^{max}$ (kg/(s m^3)) denotes the maximum mass exchange rate. The strain dependent part of the growth is given by [20]

$$\hat{\rho}^{\text{lim}} = \begin{cases} \left(\frac{J_{Sg}^{\text{max}} - J_{Sg}}{J_{Sg}^{\text{max}} - 1}\right)^{\gamma} (\epsilon_e - \epsilon_{\text{max}}) & \text{if } J_{Sg} < J_{Sg}^{\text{max}} \ \& \ \epsilon_e > \epsilon_{\text{max}} \\ 0 & \text{if } J_{Sg} \geq J_{Sg}^{\text{max}} \ \text{or} \ \epsilon_e \leq \epsilon_{\text{max}} \end{cases} \qquad (4.56)$$

with J_{Sg}^{max} being the maximum growth factor, which acts to limit the amount of growth as J_{Sg} tends towards it, of which is additionally controlled by the parameter γ. As discussed in Sec.(3.2.2), ϵ_e represents the elastic part of the cardiomyocite stretch. ϵ_{min} is the minimum stretch needed for growth to be activated, below which; $\hat{\rho}^S = 0$. With reference to Sec.(3.2.2), which introduced the concept of finite growth, the equation above was chosen to model fibre growth, and specifically for the physiological condition of cardiac dilation, see Chapter 2. Furthermore, Eq.(4.56) was selected to represent the rate of change of density of the system, and is analogous to that proposed by Goktepe et al. [20]. However, within the framework developed by Goktepe et al. [20], the growth multiplier, or for the case of fibre growth, the growth Jacobian J_{Sg}, is treated as an unknown and is solved iteratively till the system of equations are kinematically balanced. Within TPM however, an expression which allows for the explicit formulation of J_{Sg} is presented in Eq.(4.53), as proposed by Werner [80]. The issue with the proposed growth law, as shown by Eq.(4.53) and Eq.(4.56), is that there is interdependence between the growth multiplier J_{Sg}, and the constitutive law which dictates the rate of growth $\hat{\rho}^S$. In order overcome this the following simplified adaptation is proposed

$$J_{Sg}^{n+1} = J_{Sg}\left(\left(\underline{\hat{\rho}}^S\right)^{n+1}, \left(n^S\right)^{n+1}\right) \qquad (4.57)$$

With J_{Sg} in the current time step being defined in terms of the current solid volume fraction n^S and $\underline{\hat{\rho}}^S$, which is consequently postulated as

$$\left(\underline{\hat{\rho}}^S\right)^{n+1} = \underline{\hat{\rho}}^S(J_{Sg}^n, \mathbf{u}^{n+1}) \qquad (4.58)$$

and which is calculated from Eq.(4.56), with the exception that J_{Sg} from the previous time step is used. Finally, $\hat{\rho}^S$ for the (n+1) time step, is defined as

$$\left(\hat{\rho}^S\right)^{n+1} = \hat{\rho}^S\left(J_{Sg}^{n+1}, \mathbf{u}^{n+1}\right) \qquad (4.59)$$

Chapter 5

Cardiac Mechanics

With the description the hearts physiology discussed in Chapter 2, this chapter will hence focus on the mathematical models used to characterize the mechanics and hemo-dynamics of a left ventricle system. As such, the passive and active models used in this research, and the incorporation of the Theory of Porous Media, will be discussed.

5.1 Diastolic Filling

When the mitral valve reopens at the onset of the diastolic filling stage, blood is allowed to enter the ventricular cavity. It is assumed that, during this phase, the heart does not exert any force but rather deforms and behaves in a passive manner. This section will entail laying forth some of the key aspects related to the treatment of myocardial tissue with respect to development of the constitutive theory needed to model a left ventricular system during the passive filling stage. Characteristics such as, the assumption of material incompressibility and the orthotropic nature of cardiac tissue, will be discussed.

5.1.1 Material incompressibility

As discussed in Chapter 4, incompressibility is assumed for all three phases of the left ventricle. With respect to the treatment of the solid phase, this is analogous to the current trend in cardiac mechanics as stated by Usyk et al. [73] and may be further motivated through the work performed by Vossoughi and Patel [77]. Tests were conducted on samples of myocardial tissue in order to measure the volumetric strains through application of a hydrostatic stress. It was hence concluded that the assumption of idealizing cardiac tissue as near incompressible was valid. However, as suggested by Yin et al.[86], cardiac tissue may be viewed as being slightly compressible. Due to the myocardium being comprised of a vast array of blood vessels, of which are distensible, a reduction in volume of the fluid within these vessels may be seen to take place as the level of stress increases during the hearts activity [86].

5.1.2 Orthotropic material behaviour

Regarding modelling of the myocardium, isotropy, transverse isotropy and orthotropy may be considered, according to Usyk et al. [73]. In the case of isotropy, there is no dominant material direction, with transverse isotropy the material is aligned along one direction, and with the orthotropy case, the material fibres would differ across three orthogonal directions. As discussed in Sec. (2.1.1.), the myocardium is made up of muscle fibres that are arranged in a way which results in it being orthotropic in terms of the mechanical behaviour [30]. Work done by Dokos et al. [14] demonstrated through a series of shear tests performed on a passive ventricular myocardium of a

pig hearts, showed that tissue displayed different shear properties along the three principle material directions. In this research, an orthotropic model was adopted. An illustration of the myocardium which includes the three principle material directions, namely, the sheet axis ($\mathbf{s}$), fibre axis ($\mathbf{f}$) and axis of the normal to the sheet plane ($\mathbf{n}$), is shown in Fig.(5.1).
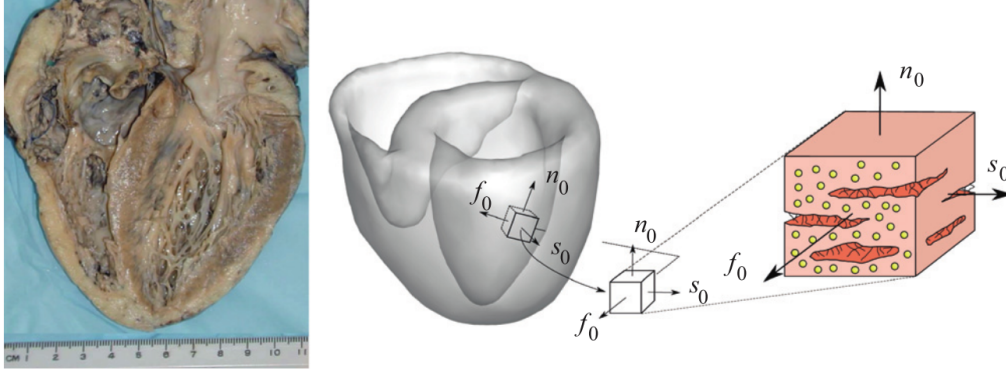

FIGURE 5.1: Architecture of the myocardium which displays the three orthogonal material directions: the sheet axis ($\mathbf{s}$), fibre axis ($\mathbf{f}$) and axis of the normal to the sheet plane ($\mathbf{n}$). [20]

5.1.3 Constitutive modelling

Continuing from Chapter 4, which ended by deriving the constitutive relations for the second Piola-Kirchhoff stress tensor $\mathbf{S}$, which was furthermore expressed in terms of the strain energy function ψ^{S}, this section will aim to develop the rest of the constitutive relations needed fully describe the stress of the material. Considering the near incompressible and orthotropic nature of myocardial tissue, the following strain energy function which describes the mechanical behaviour of cardiac systems during the passive filling stage, developed by Usyk et al. [73], has been adopted as part of this research.

The passive strain energy of the left ventricle may be expressed in terms of an additive function of the orthotropic and exponential behaviour of the heart, $W_{\mathrm{exp\text{-}ortho}}$, and the near incompressibility condition, W_{comp}, of which is related by [41]

$$\psi^{\mathrm{S}} = W_{\mathrm{exp\text{-}ortho}} + W_{\mathrm{comp}} \tag{5.1}$$

and may be expanded in the form

$$\psi^{\mathrm{S}} = \mathrm{A}\frac{\left(e^{\mathrm{Q}} - 1\right)}{2} + \mathrm{A}_{\mathrm{comp}}\left[\mathrm{J_S} \cdot \ln \mathrm{J_S} - \mathrm{J_S} + 1\right] \tag{5.2}$$

with the two groups of terms corresponding to $W_{\mathrm{exp\text{-}ortho}}$ and W_{comp}, respectively. In Eq. (5.2), the term A refers to the stiffness factor and $\mathrm{A}_{\mathrm{comp}}$ is a coefficient which mediates the level of compressibility of the myocardial tissue. The exponent Q, which is expressed in Eq. (5.5), controls the orthotropic component by making use of the elastic part of the green strain tensor $\mathbf{E}_{\mathrm{Se}}$ and the structural tensors; $\mathbf{M}_{\mathrm{f}}$, $\mathbf{M}_{\mathrm{s}}$ and $\mathbf{M}_{\mathrm{n}}$:

$$\begin{aligned} \mathrm{Q} = {} & a_1(\mathrm{tr}(\mathbf{M}_{\mathrm{f}}\mathbf{E}_{\mathrm{Se}}))^2 + a_2(\mathrm{tr}(\mathbf{M}_{\mathrm{s}}\mathbf{E}_{\mathrm{Se}}))^2 + a_3(\mathrm{tr}(\mathbf{M}_{\mathrm{n}}\mathbf{E}_{\mathrm{Se}}))^2 \\ & + a_4(\mathrm{tr}(\mathbf{M}_{\mathrm{f}}\mathbf{E}_{\mathrm{Se}}^2)) + a_5(\mathrm{tr}(\mathbf{M}_{\mathrm{s}}\mathbf{E}_{\mathrm{Se}}^2)) + a_6(\mathrm{tr}(\mathbf{M}_{\mathrm{n}}\mathbf{E}_{\mathrm{Se}}^2)) \end{aligned} \tag{5.3}$$

a_i represents material parameters, of which may are determined through a combination of *bi-axial* and *tri-axial* tests [56]. The stuctural tensors may be redefined as

$$\mathbf{M}_f = \mathbf{f} \otimes \mathbf{f}, \quad \mathbf{M}_s = \mathbf{s} \otimes \mathbf{s}, \quad \mathbf{M}_n = \mathbf{n} \otimes \mathbf{n} \tag{5.4}$$

whereby the directions; $\mathbf{f}$, $\mathbf{s}$ and $\mathbf{n}$, represent the fibre direction, sheet direction and the sheet normal direction, respectively.

As stated in Eq. (4.35), the dependence of the Cauchy stress tensor is set to the derivative of the solid porous skeleton with respect to deformation, and the solid volume fraction. However, the inclusion of the solid volume fraction was neglected. The effect of the change in n^S with respect to the solid energy function is however accounted for as a stiffening coefficient to the strain energy function ψ^S, of which is postulated by [80]

$$\psi^S = \left(\frac{n^S}{n^S_{0S}} \right)^n \psi^S \tag{5.5}$$

where n^S_{0S} represents the reference solid volume fraction and n is denoted as a density-elasticity exponent which controls the level of stiffening given by the fraction $\left(\frac{n^S}{n^S_{0S}} \right)$ [80].

Following from Eq. (4.37) in Chapter 4, the second Piola-Kirchhoff stress tensor $\mathbf{S}$ is expressed as

$$\mathbf{S} = 2 \frac{\partial \psi^S}{\partial \mathbf{C}_S} - \lambda J_S \mathbf{C}_S^{-1} \tag{5.6}$$

However, due to the fact that the strain energy function is dependent on the elastic part of the deformation (expressed through $\mathbf{E}_{Se}$), the following pull-back operation was introduced in order to relate the stress-free configuration to the reference configuration, from which the elastic second Piola-Kirchhoff stress tensor $\mathbf{S}_E$ is postulated by

$$\mathbf{S}_E = 2 \frac{\partial \psi^S}{\partial \mathbf{C}_S} = 2 \mathbf{F}_{Sg}^{-1} \frac{\partial \psi^S}{\partial \mathbf{C}_{Se}} \mathbf{F}_{Sg}^{T-1} \tag{5.7}$$

of which Eq. (4.38) was made use of. Hence Eq. (5.6), may be rewritten as

$$\mathbf{S} = 2 \mathbf{F}_{Sg}^{-1} \frac{\partial \psi^S}{\partial \mathbf{C}_{Se}} \mathbf{F}_{Sg}^{T-1} - \lambda J_S \mathbf{C}_S^{-1} \tag{5.8}$$

5.2 Isovolumetric contraction and relaxation

The last three phases of the cardiac cycle, namely; the isovolumetric contraction, ejection and isovolumetric relaxation, is termed the *active contraction* stage, and usually results in the muscle fibres contracting which as a result causes the ventricular pressure within the cavity to increase due to the accumulated strain energy developed. During isovolumetric contraction and relaxation the heart, which are phases during the cycle characterized by a closed thermodynamic system whereby all the valves are closed and no blood is allowed to enter or exit the cavity, the heart experiences no change in cavity volume [30].

Apart from the diastolic filling stage, whereby the heart behaves in a passive manner, the isovolumetric contraction and relaxation, and ejection stages result in the muscle fibres engaging in an active response of physical and electro-mechanical behaviour. This response is facilitated through a contraction of sarcomeres which is time dependent on a calcium Ca^{2+} ion concentration [22]. Calcium ions occupy a pivotal role in the excitation-contraction coupling of muscle tissue and additionally regulates

many metabolic reaction processes which take place during the hearts activity [4]. What triggers this spontaneous activation of calcium ions is a propagating depolarizing wave, in the form of an electrical pulse [33]. These electrical pulses are initiated within the myocardium, which in turn, opens calcium ion channels [30]. This increase in calcium concentration is what results in the sarcomeres to rapidly contract and hence provides the ventricle with an adequate energy supply to eject blood beyond the valves and against the resistance of the various circulatory systems [33].

Studies have been performed to model the electro-physiological effects of the heart at the microscopic level, such as at the cellular level [63, 68], and on the macroscopic tissue level [51, 66]. With respect to whole heart modelling, integrated electro-mechanical models of the whole heart have been developed. As such, these models employ methods that assume a asynchronous, anisotropic wave, which hence means that the wave propagation through the heart differs in time and space. The Eikonel diffusion equation and the bidomain equations are two models which may be used to describe such systems, as stated by Kerckhoffs et al. [31]. Within this research a simplified approach was adopted whereby synchronous wave propagation was assumed. This assumption therefore leads to concurrent fibre contraction, with respect to time, throughout the whole domain of the heart, of which is given by the *active stress model*, developed by Guccione and McCulloch [22].

5.2.1 Active stress model

As stipulated by Guccione and McCulloch [22], the sarcomere length and the calcium ion concentration were found to be the most significant factors in relation to active contraction. As such, the active tension, given by as stipulated by Guccione and McCulloch [22], is postulated by

$$T_A = T_{max} \frac{Ca_0^2}{Ca_0^2 + ECa_{50}^2} C_t \qquad (5.9)$$

with T_{max} representing the maximum tension developed. Ca_0 and ECa_{50} denote the intracellular calcium ion concentration at peak value, and at 50 percent of the peak contraction force, respectively. l is the sarcomere length, and lastly, C_t is the time transient, which is defined as

$$C_t = \frac{1}{2} \left(1 - \cos \omega(l,t) \right) \qquad (5.10)$$

ω is expressed as a piece-wise equation over three stages, such that; the first stage occurs over the period during which the time is equal to zero till the time needed for the tension to reach T_{max}, the second is during the time period over which the the tension reduces to zero from the maximum value, and finally, the third equation describes the period at which there is no contraction: [56]

$$\omega(l,t) = \begin{cases} \pi \frac{t\text{-}u}{t_0} & \text{if } 0 \leq t < t_0 \\ \pi \frac{t\text{-}u-t_0}{t_r} & \text{if } 0 \leq t_0 < t < t_0 + t_r \\ 0 & \text{if } t \geq t_0 + t_r \end{cases} \qquad (5.11)$$

t_0 is the time at which the active tension reaches T_{max}, t is the current time, u is the depolarization time and t_r is the time needed for the tension to reduce to zero. t_r may be defined as a linear equation, and is given by

$$t_r = ml + b \qquad (5.12)$$

of which varies in relation to the sarcomere length l, and is additionally defined by the two constants, m and b. ECa_{50} is defined as

$$ECa_{50} = \begin{cases} \dfrac{[Ca_0]_{max}}{\sqrt{\exp[B(l-l_0)]-1}} & \text{if } l > l_0 \\ 0 & \text{if } l \leq l_0 \end{cases} \qquad (5.13)$$

Ca_0 is the maximum intracellular calcium ion concentration, l_0 is the sarcomere length when the heart is in a state of rest and during which there is no active tension, and B is a constant which moderates the level of the peak tension-length relation. The sarcomere length l, of which is shown in Eq. (5.14), is expressed in terms of the elastic green strain tensor $\mathbf{E}_{Se}$ and l_R, which is the sarcomere-rest length:

$$l = l_R\sqrt{2E_{ff}+1}, \quad E_{ff} = tr(\mathbf{M}_f\mathbf{E}_{Se}) \qquad (5.14)$$

E_{ff} represents the fibre strain. The total second Piola-Kirchhoff stress tensor $\mathbf{S}$, during the active contraction stage, is expressed as a summation of the passive stress (given in Eq.(5.8)) and the stress which arises solely due to the active tension:

$$\mathbf{S} = \mathbf{S}_P + \mathbf{S}_A \qquad (5.15)$$

The elastic part of the active second Piola-Kirchhoff stress tensor $\mathbf{S}_{Ae}$, which is expressed in terms of the component of the active tension T_A in the fibre direction $\mathbf{f}$, is postulated as

$$\mathbf{S}_{Ae} = T_A\mathbf{M}_f \qquad (5.16)$$

As was done with the elastic part of the passive stress in Eq.(5.7) and Eq.(5.8), the following pull-back back operation is used to transfer the stress from the intermediate to the reference configuration:

$$\mathbf{S}_A = \mathbf{F}_{Sg}^{-1}\mathbf{S}_{Ae}\mathbf{F}_{Sg}^{T-1} \qquad (5.17)$$

5.3 Ejection

The ejection phase of the cardiac cycle is associated with blood being pumped out of the ventricles and into the various circulatory systems, as was discussed in Chapter 2. It is well understood that cardiac function is greatly affected by the hemodynamics of the arterial system. The hemodynamics is defined as the description of blood flow within the circulatory system, and may be influenced by various physical factors, such as; blood vessel length and radius, blood viscosity, and the functioning of the heart valves, for example [34].

The hemodynamics of the human body may be modelled using various methods, such as with lumped models [55, 83], and tube models [7, 54]. Lumped models, of which are commonly referred to as Windkessel models, is the model which has been used as part of this research study and will be further discussed hereon. The Windkessel model comprises of differential equations which describe the dynamic properties of the aortic pressure and blood flow in relation to parameters such as, the arterial compliance, resistance through the circulatory systems and the general inertia of the blood [11]. Due to the fact that Windkessel models are based on a discrete distribution of parameters, it is hence not adequate in providing input with regard to certain phenomena, such as with wave transmission and blood flow distribution [82]. However, it is suitable and non constraining model with respect to modelling ventricular function. There currently exists three Windkessel models, namely; two element, three

element and four element, models. This research employs a three element Windkessel model. Consequently, the former two models will be elaborated on in the following sections.

5.3.1 Two element Windkessel model

The two element Windkessel model is best described in relation to the analogy of an electrical circuit. In the circuit shown in Fig.(5.2), there are two parameters which form the basis of the two element Windkessel model, namely, the arterial compliance C, which acts as a capacitor, and the resistance of blood flow through the various blood vessels, R, as illustrated by the resistor [11]. The resistance R, may be expressed using the following relationship [11]:

$$R = \frac{P}{I_3} \tag{5.18}$$

With P representing the pressure difference of the circulatory system, which hence drives the flow of blood, and I_3 being the blood flow current through the resistor. The arterial compliance C, may be determined through the equation [11]

$$I_2 = C\frac{dP}{dt} \tag{5.19}$$

With I_2 being the flow through the capacitor, shown in Fig.(5.2), and t being time.
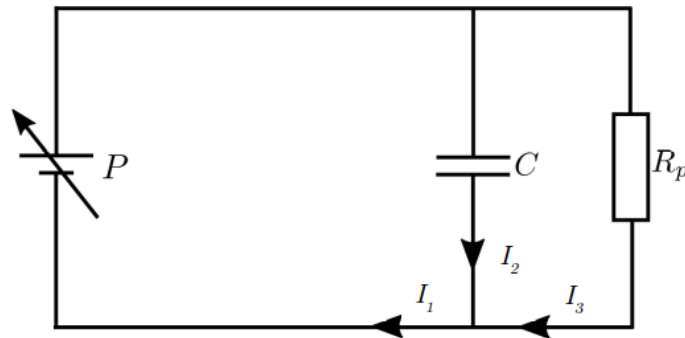

FIGURE 5.2: An illustration of a two element Windkessel model. [56]

Using Kirchhoff's law, the blood flow I_1, may be determined using the equation below:

$$I_1 = I_2 + I_3 \tag{5.20}$$

As such, a differential equation may be formed using the expressions of I_2 and I_3, of which leads to

$$I_1 = \frac{P}{R} + C\frac{dP}{dt} \tag{5.21}$$

Solving Eq. (5.21) would require an iterative scheme. However, for the condition where the heart is in a state of relaxation, during diastole when the valves remain closed, it may be assumed that there is negligible flow of blood within the body, hence I = 0. During this period, the following expression may be generated [11]

$$P = P_d \exp\left[-\frac{(t\text{-}t_d)}{RC}\right] \tag{5.22}$$

Where P_d represents the blood pressure at the start of isovolumetric relaxation, and at time t_d.

5.3.2 Three element Windkessel model

Building on the two element Windkessel model, the three element version incorporates the energy loss due to blood flowing through the aortic valve during ejection. The aortic valve area and aortic valve resistance is known to affect the flow rate of blood beyond the valve [46]. Such studies have been performed whilst analysing the contributing factors of aortic stenosis [46, 76]. The resistance through the aortic valve, given by R_a, is hence accounted for within the circuit shown in Fig.(5.23), and specifically within the main segment of the circuit due to the fact that the energy loss occurs solely within the valve. Adopting a similar approach as in the last last section, we
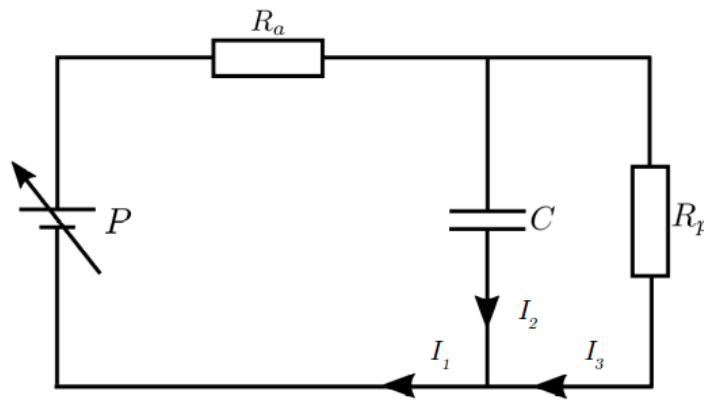
FIGURE 5.3: An illustration of a three element Windkessel model. [56]

arrive at the following differential equation:

$$\left(1 + \frac{R_a}{R_p}\right) I_1 + R_a C \frac{dI_1}{dt} = \frac{P}{R_p} + C \frac{dP}{dt} \tag{5.23}$$

It is trivial to observe that the closed solution to Eq.(5.23), for the condition during which there is no flow within the systemic circulation (during isovolumetric contraction), produces the same expression shown in Eq.(5.2).

Chapter 6

Numerical treatment

The finite element method (FEM) is used as a numerical framework to approximate the differential equations present within the triphasic TPM model. This section will lay forth the weak formulations, derived from the balance equations shown in Sec.(4.2), the initial boundary value problem, time discretization techniques, and the cardiac mechanics framework implemented within the in-house built software SESKA. Finally a numerical example will be covered in order to validate the proposed model.

6.1 Weak forms

Considering the set of unknown quantities for the triphasic model, shown by Eq.(4.20), the governing equations may be solved for in order to quantify these variables and hence close the system of equations. The displacement $\mathbf{u}_S$ will be solved using the balance equation of momentum. The pore pressure λ will be calculated through the balance equation of mass of the mixture. Lastly, the solid and nutrient volume fractions n^S and n^N, will be determined using the respective balance equations of mass. Using the Galerkin approach, which may be used to transform a system of equations into a discrete problem, allows weak forms to be generated from the aforementioned balance equations. The weak forms of the proposed triphasic model will be presented in the following sections.

6.1.1 Balance of momentum

Following from Eq.(4.11), and by applying the variation of the displacement $\delta\mathbf{u}_S$, the weak form of the balance of momentum is as follows

$$G_u = \int_{B_\alpha} \mathbf{S} : \delta\mathbf{E}\,dV - \int_{\partial B_\alpha} \mathbf{t} \cdot \delta\mathbf{u}\,dA = 0 \tag{6.1}$$

6.1.2 Balance of mass: mixture

Referring to the balance equation of mass Eq.(4.9), the weak form for the case which describes the entire mixture reads

$$G_\lambda = -\int_{B_\alpha} n^F \mathbf{w}_{FS0} \cdot \mathrm{Grad}\delta\lambda\,dV + \int_{B_\alpha} J_S\,(\mathbf{E}_S)'_S : \mathbf{C}_S^{-1}\delta\lambda\,dV+$$
$$\int_{B_\alpha} J_S\hat{\rho}^S \left(\frac{1}{\rho^{NR}} - \frac{1}{\rho^{SR}}\right)\delta\lambda\,dV - \int_{\partial B_\alpha} n^F \mathbf{w}_{FS0} \cdot \mathbf{n}_0\delta\lambda\,dA = 0 \tag{6.2}$$

Where use is made of the variation of the pore pressure $\delta\lambda$. It is apparent that in addition to the Dirichlet boundary condition which needs to be applied to the system

of equations, a Neumann boundary condition may be used in relation to the final term shown in Eq.(6.2).

6.1.3 Balance of mass: solid

Making use of the local form of the balance of mass for the solid constituent Eq.$(4.10)_1$, and by weighting it using the variation of the solid volume fraction δn^S, the following weak form is produced:

$$G_{n^S} = \int_{B_\alpha} \left[J \left(n^S\right)'_S + Jn^S \left(\mathbf{E}\right)' : \mathbf{C}^{-1} - J \frac{\hat{\rho}^S}{\rho^{SR}} \right] \delta n^S \, dV = 0 \tag{6.3}$$

Due to the fact that the solid particles are not physically able to diffuse out from the system, there contains no flux term [80].

6.1.4 Balance of mass: nutrient

Starting with Eq.$(4.10)_3$, the weak form of the balance of mass for the nutrient constituent is postulated as

$$G_{n^N} = \int_{B_\alpha} J_S \left[\left(n^N\right)'_S + n^N \left(\mathbf{E}_S\right)'_S : \mathbf{C}_S^{-1} + \frac{\hat{\rho}^S}{\rho^{NR}} \right] \delta n^N \, dV$$

$$- \int_{B_\alpha} \left(\frac{n^N}{1 - n^S} \right) n^F \mathbf{w}_{FS0} \cdot \mathrm{Grad}\delta n^N \, dV + \int_{\partial B_\alpha} \left(\frac{n^N}{1 - n^S} \right) n^F \mathbf{w}_{FS0} \cdot \mathbf{n}_0 \delta n^N \, dA = 0 \tag{6.4}$$

which makes use of the variation of the respective quantity. As the nutrients are contained within the bulk fluid phase, they may either leave or enter the system domain through application of the flux boundary condition, shown by the final term in Eq.(6.4). Hence, this may act as a source for the provision of nutrients.

6.2 Initial boundary value problem

The boundary value problem considered comprises of the quantities found from the list of unknown variables, shown in Eq.(4.20). The boundary values are generally given with respect to two forms, namely, Dirichlet boundary conditions, and Neumann boundary conditions. Dirichlet boundary conditions ∂B_D, dictate the approximation by explicitly imposing the solution of the given quantity, and are needed in order to solve the system of equations. Neumann boundary conditions ∂B_N refers to when the derivative of a solution of a quantity is applied along the boundary, and is prescribed using the surface integral terms in the weak forms, shown in Sec.(6.1). A critical aspect of the two boundary conditions, in relation to a specific unknown variable $\mathcal{U}$, is that they may not be prescribed over the same domain, such that

$$\partial B_D^{\mathcal{U}} \cup \partial B_N^{\mathcal{U}} = \partial B^{\mathcal{U}}, \quad \partial B_D^{\mathcal{U}} \cap \partial B_N^{\mathcal{U}} = 0 \tag{6.5}$$

However, concurrent positioning of boundary conditions between different quantities is valid. In terms of the Dirichlet boundary conditions, the prescribed unknown variables used to define these are; displacement $\bar{\mathbf{u}}_S$, pore pressure $\bar{\lambda}$, solid volume fraction $\bar{n}^S$, and the nutrient volume fraction $\bar{n}^N$. In terms of the Neumann boundary conditions, the quantities are; traction $\mathbf{t}$, fluid flux $\bar{\mathbf{w}}_F$, and the nutrient flux $\bar{\mathbf{w}}_N$.

6.3 Temporal discretization

The time discretization scheme which is adopted within this research is the *Newmark-β* method. This method provides a flexible and stable time integration scheme. Starting from the finite difference approximation of the quantity $(\bullet)$, the Newmark equations of motion may be written as follows:

$$\ddot{(\bullet)}_k^{n+1} = \frac{1}{\Delta t^2 \beta}\left[(\bullet)_k^{n+1} - (\bullet)^n - \Delta t \dot{(\bullet)}^n - \Delta t^2 \left(\frac{1}{2} - \beta\right)\ddot{(\bullet)}^n\right] \tag{6.6}$$

$$\dot{(\bullet)}_k^{n+1} = (\bullet)^n + \Delta t\left[(1-\gamma)\ddot{(\bullet)}^n + \gamma \ddot{(\bullet)}_k^{n+1}\right] \tag{6.7}$$

With $n+1$ and k being the current time and iteration step, respectively. β and γ represent the Newmark parameters. The constant acceleration method is employed in this study, which results in the parameters $\beta = 1/4$ and $\gamma = 1/2$, being used. Using that combination of parameters renders the time scheme as unconditionally stable.

Using the increment of the quantity $\Delta(\bullet)$, which will be elaborated on in the following sections, the quantity in the current iteration and time step may be updated such that

$$(\bullet)_k^{n+1} = (\bullet)_{k-1}^{n+1} + \Delta(\bullet) \tag{6.8}$$

Using $(\bullet)_k^{n+1}$ and the Newmark equations of motion, the acceleration and velocity may be explicitly determined. In addition, the increment of the velocity field for the various primary variables may be formulated by first substituting Eq.(6.8) and Eq.(6.6) into Eq.(6.7). By computing the change with respect to $(\bullet)$, the following expression is yielded:

$$\Delta \dot{(\bullet)}_k^{n+1} = \frac{\gamma}{\Delta t \beta}\Delta(\bullet)_k^{n+1} \tag{6.9}$$

6.4 Cardiac modelling

This section will elaborate on the implementation of the various cardiac mechanics models discussed in Chapter 5, of which includes those formulated for the passive filling phase, the isovolumetric phases and ejection. These models will be presented in context of the Galerkin approach.

6.4.1 Iterative solution of non-linear algebraic equations

This section will illustrate the procedures behind solving non-linear problems in relation to the solid displacement field $\mathbf{u}$. It may however be extended to the rest of the primary variables $\mathcal{U}$. The discrete equation system generally takes the following form:

$$\mathbf{K}\Delta\mathbf{u} - [\mathbf{f}_{\text{ext}} - \mathbf{f}_{\text{int}}] = \mathbf{0} \tag{6.10}$$

with $\mathbf{K}$ being the stiffness matrix, $\Delta\mathbf{u}$ representing the displacement field increment, $\mathbf{f}_{\text{ext}}$, the external force vector, and $\mathbf{f}_{\text{int}}$, the internal force vector. Solving Eq.(6.10) for linear problems may be done explicitly, however with respect to non-linear problems, iteration schemes generally need to be employed. As such, the iteration procedure used within this study is the *Newton-Raphson* method.

The Newton-Raphson method is a fast and effective iterative solving procedure, provided that the initial solution lies within close proximity of the final solution. Convergence rates of up to quadratic order may be achieved, of which is a significant advantage in terms of solution processing efficiency. A disadvantage however lies

within the fact that the for every iteration step, the stiffness matrix $\mathbf{K}$ needs to be re-computed and inverted.

The Newton-Raphson method may be explained by firstly considering the linearisation of the weak forms presented in Sec.(6.1). The weak form of the balance of momentum will be considered in relation to the displacement field $\mathbf{u}$, for simplicity. The weak form may be linearised using a first order Taylor series expansion:

$$\delta \mathrm{G}_{\mathbf{u}} \left(\mathbf{u}_n^k \right) = \delta \mathrm{G}_{\mathbf{u}} \left(\mathbf{u}_n^{k-1} + \Delta \mathbf{u} \right) = \delta \mathrm{G}_{\mathbf{u}} \left(\mathbf{u}_n^{k-1} \right) + \frac{\partial \delta \mathrm{G}_{\mathbf{u}} \left(\mathbf{u}_n^k \right)}{\partial \mathbf{u}_n^k} \mid_{\mathbf{u}_n^{k-1}} \cdot \Delta \mathbf{u} \approx 0 \quad (6.11)$$

with k and n being the current iteration and loading or time step, respectively. The unknown displacement field in the current iteration step is found using:

$$\mathbf{u}_n^k = \mathbf{u}_n^{k-1} + \Delta \mathbf{u} \tag{6.12}$$

The discrete equation system shown in Eq.(6.10), in terms of the current iteration and loading or time step, is postulated as

$$\mathbf{K}_n^k \Delta \mathbf{u} = [\mathbf{f}_{\mathrm{ext}}]_n^k - [\mathbf{f}_{\mathrm{int}}]_n^k = \mathbf{R}_n^k \tag{6.13}$$

with $\mathbf{R}_k^n$ being the residual. As mentioned, the stiffness matrix and similarly, the residual, need to be solved at every iteration step. Hence, these quantities are calculated using the displacement field from the previous iteration step $\mathbf{u}_{k-1}^n$, such that; $\mathbf{R}_k^n = \mathbf{R}(\mathbf{u}_{k-1}^n)$ and $\mathbf{K}_k^n = \mathbf{K}(\mathbf{u}_{k-1}^n)$. This allows $\Delta \mathbf{u}_k^n$ to be solved using

$$\Delta \mathbf{u} = \left[\mathbf{K}_n^k \right]^{-1} \mathbf{R}_n^k \tag{6.14}$$

As such, $\mathbf{u}_k^n$ may be updated using Eq.(6.12), of which is then used as the initial starting point in the $(k+1)$ iterartion step. The solution is reached once the external and internal forces are balanced. Hence the iteration scheme is terminated based on the magnitude of the residual $\left| \mathbf{R}_n^k \right|$. Once $\left| \mathbf{R}_n^k \right|$ falls below a certain threshold, the system of equations is seen to have converged.

Following from the non-linear problem solving scheme, shown by the Newton-Raphson method, the proceeding sections will delve further into the numerical methods used to simulate a heart beat. There are generally two methods of computing the mechanisms related to the phases in the cardiac cycle, namely; the *pressure driven* method, where a pressure load is prescribed and the displacement is solved for, and the *volume driven* method, where a volume is specified and the solution is found in the form of the load.

6.4.2 Diastolic filling

As implemented in SESKA, the diastolic filling stage is simulated using a pressure driven algorithm. This is used to model the hydrostatic pressure that the blood exerts on the myocardial walls as it enters the left ventricular cavity. The diastolic filling is modelled through an incrementally applied traction load on the inner surface of the endocardium, which ranges from zero, when the cavity is empty, to P^{ED}, at the point of end diastolic volume (EDV). In order to apply the load in increments, such that the final solution stays within close vicinity and is easily approximated, a *Neumann loading factor* ζ, is applied on the total pressure load P^{ED}. The pressure

load P, in the current loading step n, is determined such that

$$P = \zeta_n P^{ED}, \quad 0 \leq \zeta \leq 1 \tag{6.15}$$

At the end of every loading step, the loading factor is updated for the next step:

$$\zeta_{n+1} = \zeta_n + \Delta\zeta \tag{6.16}$$

where $\Delta\zeta$ is the incremental loading factor, of which may be set to constant or to vary throughout the simulation. Referring to Eq.(6.1.1), the traction load is formulated to be independent of deformation. However, during diastolic filling, it is compulsory that the loading remain perpendicular to the myocardial walls. Hence, in order to adapt the surface traction load in terms of being dependent on deformation, the following equation is used:

$$\int_{\partial B_\alpha} PJ\mathbf{F}^{-T}\mathbf{n}_0 \cdot \delta\mathbf{u} \, dA \tag{6.17}$$

with all quantities being previously defined. Hence, by considering Eq.(6.15), Eq.(6.17) may be rewritten as

$$\zeta_n \int_{\partial B_\alpha} P^{ED}J\mathbf{F}^{-T}\mathbf{n}_0 \cdot \delta\mathbf{u} \, dA \tag{6.18}$$

Similarly, the external force vector $\mathbf{f}_{ext}$, may be redefined as follows:

$$[\mathbf{f}_{ext}]_n^k = \zeta_n [\mathbf{f}_{ext,0}] \tag{6.19}$$

with $\mathbf{f}_{ext,0}$ being the total external load. Hence, Eq.(6.13) may be expanded in the following form:

$$\mathbf{K}_n^k \Delta\mathbf{u} = \zeta_n [\mathbf{f}_{ext,0}] - [\mathbf{f}_{int}]_n^k = \mathbf{R}_n^k \tag{6.20}$$

6.4.3 Isovolumetric modelling

At the end of ventricular filling, when the cavity has reached its capacity, the valves close and the start of systole is then initiated with the isovolumetric contraction (IVC) phase. With the valves closed, and with the aspect of material incompressibility for the blood and tissue, the cavity volume remains unchanged during IVC. Consequently, this results in a pressure increase within the cavity. Similarly, at the beginning of diastole, when the muscle fibres relax, the ventricular cavity volume is seen to remain constant. In order to mathematically model this feature, a volume driven algorithm is employed. In this approach it is assumed that the change in volume is negligible, hence $\Delta V = 0$. With the displacement $\mathbf{u}$ considered a known quantity, only the blood pressure, represented through the loading factor ζ_n^k in the current loading (n) and iteration (k) step, needs to be solved for, as per Eq.(6.20). The loading factor may be determined upon calculation of $\Delta\zeta$, through the additive update

$$\zeta_n^k = \zeta_n^{k-1} + \Delta\zeta \tag{6.21}$$

with ζ_n^{k-1} being the loading factor of the previous iteration step. During the IVC, the valves are reopened once the pressure within the ventricle exceeds the pressure in the aorta. Therefore, parallel to this feature, the simulation of the IVC is terminated once ζ_n^k is greater than the parameter of the aortic valve pressure threshold ζ_{aorta}; $\zeta \geq \zeta_{aorta}$. For a more comprehensive layout of the implementation of the isovolumetric phases, refer to the work of Skatulla and Sansour [65].

6.4.4   Ejection

To model the ejection phase, a similar approach to Sec.(6.4.3) is adopted. In contrast however, the volume of the cavity does not stay constant and deforms as blood is ejected out the cavity, resulting in the condition: $\Delta V \neq 0$. Consequently, in order to find the solution for the pressure, or loading factor ζ, and the displacement field, represented through the volume V, the three element Windkessel model, shown in Sec.(5.3.2), is utilised. This furthermore involves setting up an iterative procedure using the Newton-Raphson scheme. With the iteration and loading step being k and n, respectively, the three element Windkessel may be restated as

$$\left(1 + \frac{R_a}{R_p}\right) [I_a]_n^k + R_a C \left[\frac{dI_a}{dt}\right]_n^k = \frac{1}{R_p} [P_a]_n^k + C \left[\frac{dP_a}{dt}\right]_n^k \tag{6.22}$$

with R_a and R_p being the aortic and peripheral resistance, respectively, and C representing the arterial compliance. In addition, the aortic flow rate, I_a, and aortic pressure, P_a, are defined and may be related directly to the unknown increments ΔV and $\Delta \zeta$. A descriptive overview behind the implementation of the three element Windkessel model may be viewed in the work of Essack [19].

6.5   Numerical example

Investigation of the proposed triphasic TPM model will be addressed through a simple cantilever beam example. Results attaining to the deformation, pore pressure, volume fractions, and the growth evolution, will be analysed and discussed. The cantilever beam under study, is 10m in length with a square cross-section of 1m edge length. The beam is fully restricted from translational deformation on one end, in all directions, and is loaded on the free face with transverse traction load of 50Pa, in the negative z direction. In addition, the beam is comprised of a neo-hookean material, with material constants specified in Fig.(6.1), which summarises the beam properties.

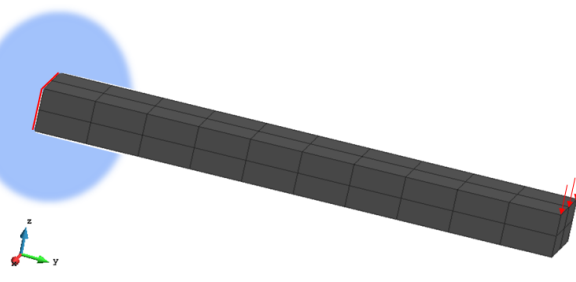| Material parameter	Value	Unit
μ^S	10000	Pa
λ^S	10000	Pa
ρ_{0S}^{SR}	100	kg/m^3
$\rho_{0L}^{LR}, \rho_{0N}^{NR}$	1000	kg/m^3
n_{0S}^S	0.5	-
n_{0L}^L	0.2	-
n_{0N}^N	0.3	-
K^F	$1 \cdot 10^{-6}$	m^4/N·s

FIGURE 6.1: Properties of the cantilever beam example.

Starting off with the condition that $\hat{\rho}^S = 0$, Fig.(6.2) illustrates the deformation behaviour of the beam with respect to the applied traction load, of which complies with expected deformation patterns. Furthermore, the deformation results are identical to

those produced by the existing biphasic model, implemented within SESKA, with convergence rates of up to quadratic order also being observed [25]. Hence, to certain degree, this validates the implementation of the proposed triphasic model.
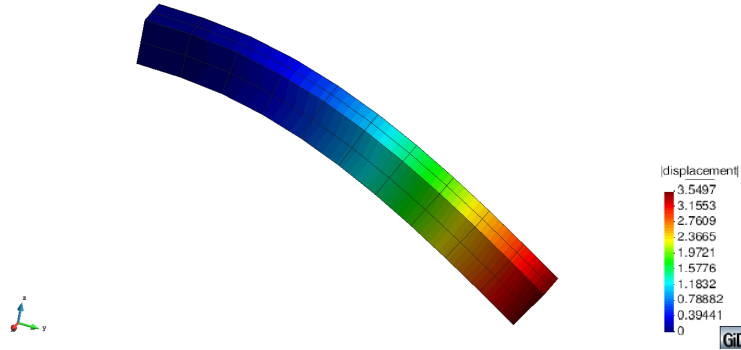

FIGURE 6.2: Deformation of the beam under the applied traction load.

From the geometrical and loading description of the beam, it is common understanding that the the fixed end of the beam will experience the greatest degree of stress. Additionally, it is valid to presume that the stress distribution across the height of the cross-section of the beam, will be anti-symmetric, with the top edge being in a state of tension, and the bottom edge being in compression. Understanding the stress distribution may provide significant insight into the analysis of the pore pressure results. The distribution of the pore pressure results may be viewed in the contour plot, shown in Fig.(6.3). Following the description of the stress distribution, it is clear that the pore pressure manifests in a similar manner. Firstly, the most extreme pore pressure values may be found at the support, showing an almost symmetrical distribution, with the top edge showing the highest values, and the bottom showing the lowest values. This may be understood through visualisation of the pore space structure in relation to different states of stress. Under tension, the pore spaces would be pulled apart, of which would result in an overall expansion of the pore space area. Consequently, an increased pore space size would result in reduced pore pressures. In contrast, under compression, the pore spaces would be pushed inwards, of which would cause the pore pressures to elevate.
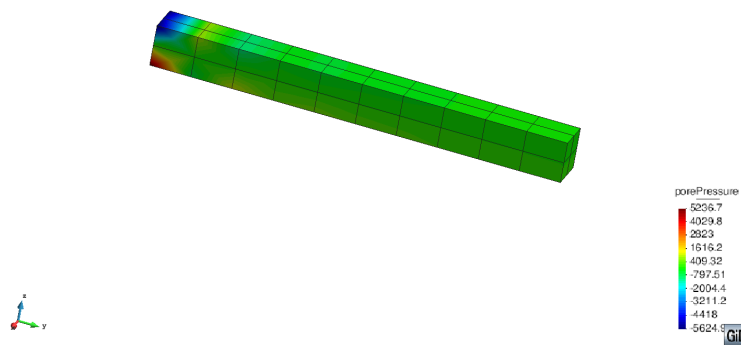

FIGURE 6.3: Contour plot of the pore pressure distribution.

With the pore pressure results discussed, a study into the aspect of growth will now

be conducted, of which will provide details regarding the nature of the volume fraction quantities and the description of growth proliferation. By inducing growth, such that $\hat{\rho}^S \neq 0$, the following graph is produced in conjunction with the case simulated without the inclusion of growth. It is apparent from Fig.(6.4), that with the addition of growth, a more elastic response is realised, as seen by the decrease in stiffness. This property is analogous to that found in the work of Hopkins [25], whereby it was motivated through the idea that with growth, an elongation of the beam occurs, of which results in a more slender beam profile.
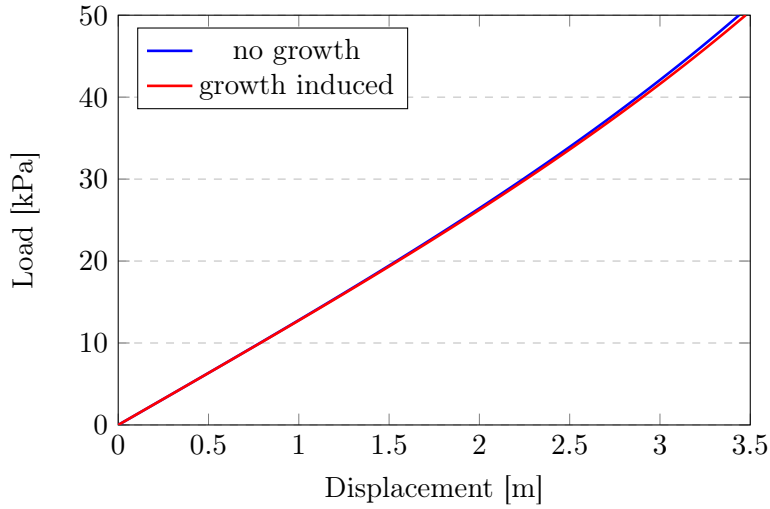

FIGURE 6.4: Displacement results with respect to the case of no-
growth and growth induced.

The effect of the growth induced model on the volume fractions will now be analysed. Specifically, the solid volume fraction, n^S, and nutrient volume fraction, n^N, will be focused on, as they are directly related to the mass supply function $\hat{\rho}^S$. Fig.(6.5) illustrates the solid and nutrient volume fractions with respect to simulations run with growth and without growth. In terms of the pore pressure degree of freedom, a close relation may be made with respect to the volume fraction quantities. In TPM, and in relation to the proposed triphasic framework, the control system is defined as a solid porous skeleton, saturated with a fluid that fills the pore spaces. Even though TPM works on the macroscale, due to application of the volume fraction concept (see Chapter 3), the pore structure has a great influence on the perfusion of fluid through the control system. A sudden contraction or enlargement of the pore spaces, which translates into changes in pore pressure, may result in fluid entering or exiting the system, respectively, due to a pore pressure differential. With comparison to the pore pressure distribution, shown in Fig(6.3), the idea of the presence of the fluid being dependent on the pore pressure is evident, as illustrated in Fig.(6.5)(c). At the support, n^N is observed to increase above and decrease below the reference value n_{0N}^N, at the top and bottom edge, respectively, of which correlates well with the pore pressure distribution. Consequently, changes in fluid volume would cause contrasting changes in the volume of the solid constituent, of which is apparent in Fig.(6.5)(a).

By inducing growth, the strain driven growth function, covered in Sec.(4.4.3), may be activated. The inclusion of growth would result in the deposition of solid mass, at the expense of the available nutrients in the system. From Fig.(6.5)(b), it may be observed that the entire beam comprises of n^S values greater than the reference value. Similarly, Fig.(6.5)(d) conveys a reduction of n^N below n_{0N}^N over the entire beam,
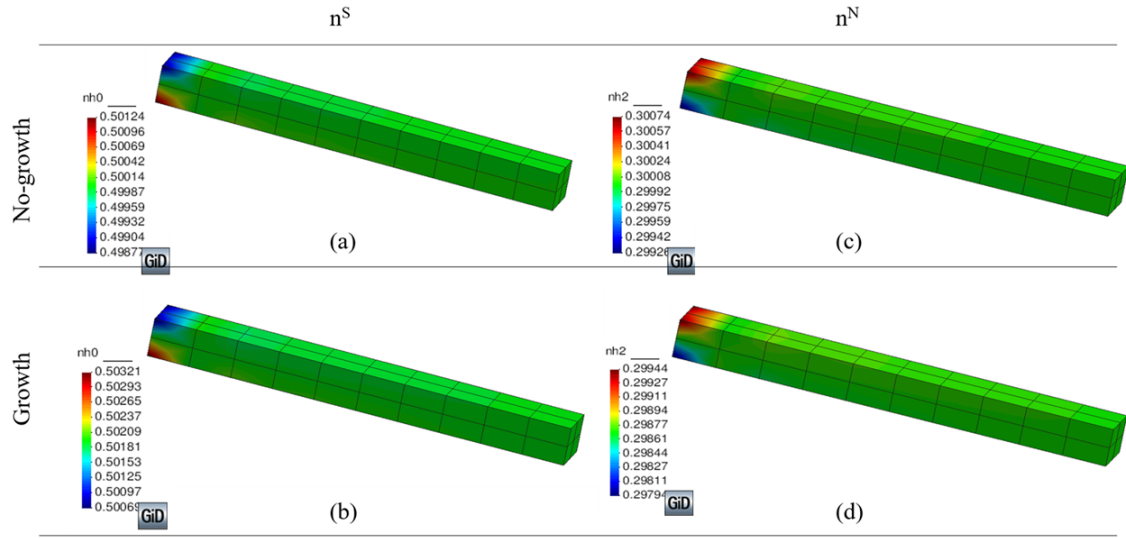
FIGURE 6.5: Contour plot of the volume fraction distribution. (a): Solid volume fraction simulated without growth. (b): Solid volume fraction simulated with growth. (c): Nutrient volume fraction simulated without growth. (d): Nutrient volume fraction simulated with growth

of which is in contrast to the examples simulated without growth, where the volume fraction terms fluctuated between the reference values. The effect of growth is evident, with reasonable results being obtained. In addition, the results with respect to the pore pressure and it's connection to the volume fraction degrees of freedom, proves that the triphasic model has been implemented in a manner which may correctly describe the mechanical and thermodynamic behaviour of porous systems.

Chapter 7

Case study of an RHD affected heart

The previous chapters have set a platform for the establishment of the mathematical framework needed for a triphasic TPM model, and additionally with application to cardiac systems which include growth and remodelling proliferation. This chapter will continue with an analysis of a patient specific heart, which has been diagnosed with rheumatic heart disease. Investigation into the behavioural changes of the heart will be conducted and will be furthermore used to validate the adequacy of the proposed TPM model in relation to modelling an RHD infected heart.

The patient under study was diagnosed with rheumatic heart disease in 2014 after CMR scanning, at the Groote Schuur Hospital. From the assessment, it was found that the patient had severely stenosed mitral valve with moderate regurgitation. The patient was admitted for a valve replacement in 2015 whereby subsequent follow-up scans were taken in 2016. This investigation will encapsulate an analysis of the two scans taken in 2014 and 2016.

7.1 Geometry and mesh generation

In order to computationally analyse a patients heart, a model needs to be generated from a cardiac geometry. One method of doing this is through segmentation of MRI/CMR scans. CMR scans usually includes a series of intermediate images through the short axis of the heart, from apex to the base, as shown in the Fig.(7.1). Within this study, images taken at the onset of diastolic filling are considered. Using that as a reference hence allows for the end systolic volume (ESV) to be quantified, which is an important parameter that may be used for calibration purposes. In order to build a 3D computational model, from the discrete set of image slices, Synopsys software package, Simpleware, is used, which incorporates interpolation and curve-fitting algorithms. A more descriptive overview of the methods pertaining to segmentation of CMR scans, and subsequent mesh generation, may be viewed in the work of Hopkins [25].
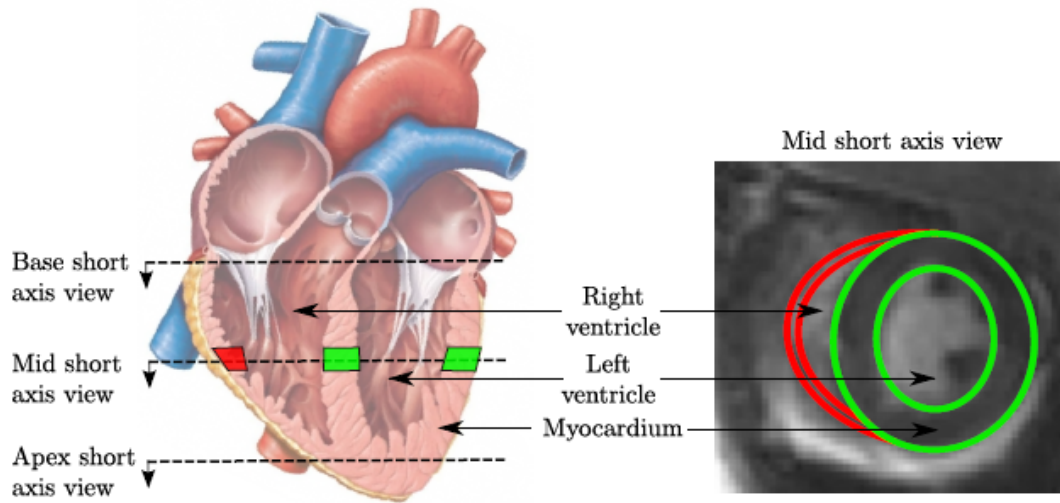
FIGURE 7.1: CMR images through short axis of a biventricle, from
the base to the apex. [25]

Two models were developed, which coincided with the set of scans taken in 2014 and
with the follow-up scans, from 2016. The models were meshed using 2068 and 2318
tetrahedral elements, for the 2014 and 2016 scans, respectively, as shown in Fig.(7.2).
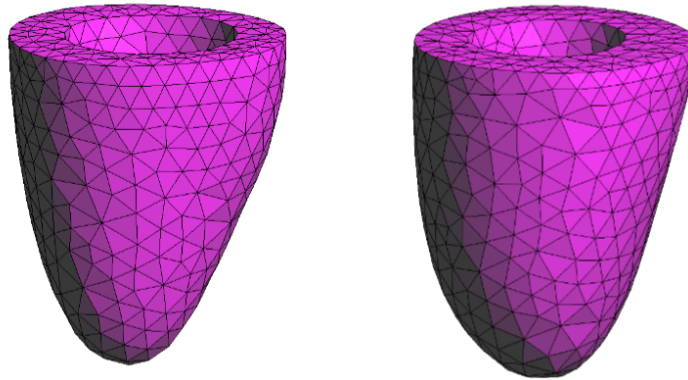[25]

FIGURE 7.2: Final meshed left ventricle models, corresponding to the
2014 and 2016 patient-specific scans. [25]

7.2   Applied boundary conditions

In order to build the boundary value problem needed for the geometry of the left
ventricle, Dirichlet and Neumann boundary conditions need to be prescribed, as men-
tioned in Chapter 6. As was discussed in Chapter 2 in relation to the physiology of
the heart, the base of the ventricle is attached to the rest of the heart through muscle
tissue and is also bound by the pericardium, of which prevents rigid body motion.
Hence, in terms of the Dirichlet boundary conditions, the base of the heart is firstly
fixed at the base, from moving in the vertical direction. During muscular contraction,

the heart experiences a degree of twist, which is a result of the muscle fibre orientation, see Sec.(2.1.1). With respect to the base, this torsional movement is limited to a small degree. In order to allow this torsional behaviour but still restrict the deformation to a level which is physiologically normal, a Dirichlet boundary condition is weakly imposed through application of an elastic line force k, around the epicardial base, as done in [56]. This additionally allows for thickening and thinning of the base during contraction [56]. Lastly, in order to restrict motion in the xy axis, bust still allow for torsional motion about the short axis, zero displacement is enforced in the xy direction at the point of the apex. The Dirichlet boundary conditions applied to the patient-specific left ventricle geometry are illustrated in Fig.(7.3).

The Neumann boundary conditions are considered next. The inflow of blood into the ventricular cavity, during the diastolic filling stage of the cardiac cycle, imparts a hydrostatic pressure on the myocardial walls. To model this, an incremental surface pressure load is prescribed on the inner surface of the endocardium. As specified in the work of Rama [56], and the citations therein, the surface pressure is assigned a value of 0 kPa and 1.5 kPa, at the start and end of diastolic filling, respectively. Due to blood not being able to seep out from the ventricles, it is assumed that the seepage flux for the entire domain of the heart is zero. With respect to the base region, it is understood that there would be blood flow generated through this section, as part of the coronary circulatory system (see Chapter 2). However, due to this being a property associated with the hemodynamics (blood would enter and leave the base at different times during the ejection phase), it is not within the scope of this study and will be left for future consideration [25].
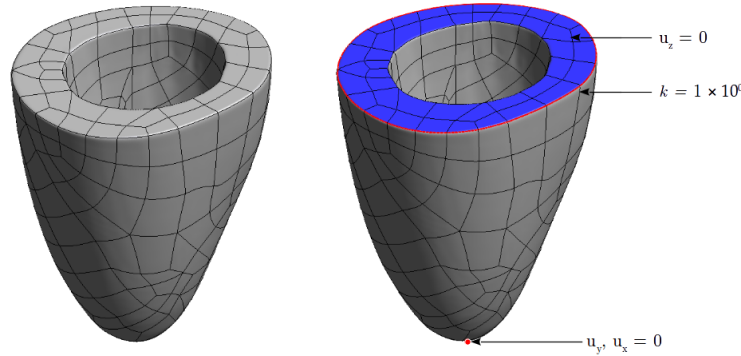

FIGURE 7.3: Dirichlet boundary conditions applied to the left ventricle models.

7.3   Material properties

With respect to cardiac modelling, there contains a variety of parameters which influence the overall characteristics of the simulated model. Briefly noting, the parameters of concern include those associated with the strain energy function ψ^S during the diastolic filling stage, the active tension model during ejection, and the Windkessel model. In addition, the orientation of the muscle fibres in the endocardium and epicardium are also of great importance. Incorporating the theory of porous media comes an array of additional parameters linked to the various constituent phases and those needed to characterize the constitutive equations formulated for the seepage velocity and mass exchange function.

Starting with the fibre orientations and the associated orthogonal cross-fibre directions of the epicardium and endocardium, the angles are approximated using an algorithm developed by Wong and Kuhl [84]. In this approach, use is made of a Poisson interpolation scheme in order to generate the fibre orientation map of the human heart. However, as described in the works of Skatulla and Sansour [65], numerically solving a Poisson problem can require a significant amount of time as compared to alternative interpolation schemes, such as the moving least square (MLS) based approximation [39]. Hence, within this work, MLS interpolation is adopted, and is used to produce the fibre directions illustrated in Fig. (7.4).
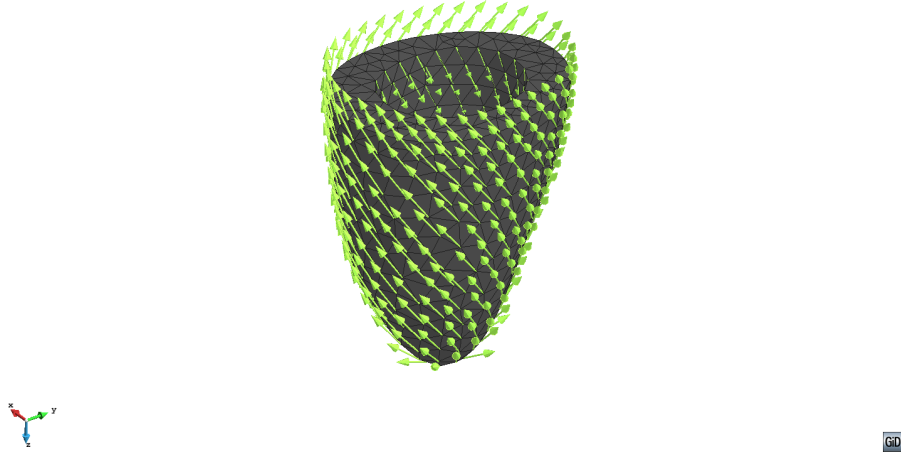

FIGURE 7.4: Myocardial fibre orientation for a left ventricle.

The fibre orientation shown in Fig. (7.4), corresponds to heart in a state of rest. The rest sarcomere lengths l_0 may also be specified individually for the endocardium and epicardium. The prescribed fibre direction angles and the rest-sarcomere lengths for the endocardium and epicardium, as specified by Skatulla and Sansour [65], are given in Table (7.1).

TABLE 7.1: Prescribed fibre directions and rest sarcomere lengths for the endocardium and epicardium. [65]

Quantity	Endocardium	Epicardium	Unit
θ_0	66	-51	°
l_0	1.78	1.91	μm

The input parameters relating to the solid tissue phase, and the liquid and nutrient phases, which are contained within the blood saturating the solid skeleton, consists of the real densities $\rho_{0\alpha}^{\alpha R}$ and the reference volume fractions $n_{0\alpha}^{\alpha}$ when the heart is in a state of rest. The parameters are given in Table (7.2)

The growth and remodelling processes which occur in people suffering from RHD generally occur over periods of months and years. Within this study, simulation of a single heart beat is used to model the growth induced over a two year period. In terms of selecting an appropriate value for the nutrient volume fraction, consideration was given to the fact that, realistically, nutrients would always be available in context of the intake through diet, or oxygen supply, etc. Hence, a greater value of 0.15 was chosen, of which still complies with expected solid tissue to blood ratios.

TABLE 7.2: Prescribed TPM parameters associated with the constituents in the reference configuration, and the seepage velocity constitutive law.

Material parameter	Value	Unit	Source
Tissue density ρ_{0S}^{SR}	220	kg/m^3	[75, 25]
Blood density ρ_{0L}^{LR}, ρ_{0N}^{NR}	1060	kg/m^3	[12]
Solid r.v.f. n$_{0S}^{S}$	0.75	-	[28]
Liquid r.v.f. n$_{0L}^{L}$	0.1	-	-
Nutrient r.v.f. n$_{0N}^{N}$	0.15	-	-
Anisotropy parameter α_{F1}	0	-	[58]
Darcy permeability K^F	$2 \cdot 10^{-9}$	m^4/N$\cdot$s	[78]

7.3.1 Calibration of passive material parameters

In order to calibrate the parameters related to the strain energy function given in Eq.(5.2), to the 2014 and 2016 patient-specific cardiac models, a comparison of the end diastolic volume (EDV) and end systolic volume (ESV) was performed. The EDV and ESV values were measured from experimental data accessed from the CMR scans. The measured EDV and ESV values for the 2014 and 2016 models may be be viewed in Table (7.3).

TABLE 7.3: Experimental values for the EDV and ESV, in relation to the 2014 and 2016 models. [25]

Quantity	2014	2016	Unit
EDV	146	147	ml
ESV	72	80	ml

Due to the geometry of the cardiac models being generated for the resting state, see Sec.(7.1), the reference volume at the beginning of the simulation is equivalent to the ESV value of the experimental data. As such, only calibration of the model in relation to the EDV had to be considered. The incremental pressure load, applied to the ventricular cavity, ranges form 0 kPa to 1.5 kPa as specified in Sec. (7.2), which correlates to the start and end of diastolic filling. Using the pressure load at the end of diastolic filling and the EDV as a target point, the stiffness factor A was calibrated, as shown in Fig.(7.5).

After calibration the target value was achieved using stiffness factor values of 0.45 and 0.57, for the 2014 and 2016 models, respectively. Consequently, the rest of the passive parameters are specified in Table.(7.4)

TABLE 7.4: Passive material parameters. [72]

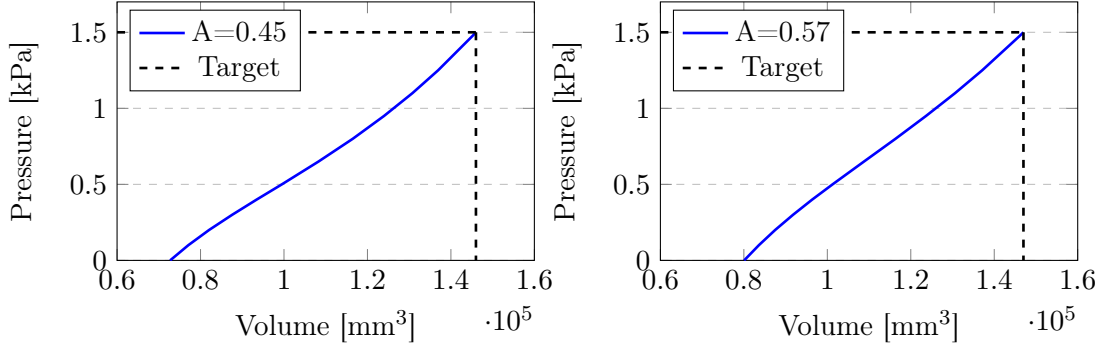| A$_{comp}$ (kPa)	a$_1$	a$_2$	a$_3$	a$_4$	a$_5$	a$_6$
100	-6.0	-5.0	9.0	12.0	12.0	-6.0

FIGURE 7.5: Calibration of 2014 (left) and 2016 (right) models, with
respect to various values of the stiffness factor A.

7.3.2 Calibration of active material parameters

Within the work of Hopkins [25], the biphasic model was calibrated using the arterial compliance C, maximum tension T_{max}, peripheral resistance R_p, and the aortic resistance R_a. These parameters comprise those found in the active tension model, shown in Sec.(5.2.1), and the three element Windkessel model Eq.(5.23). Consequently, these parameters were calibrated to meet the target ESV value at the end of the isovolumetric relaxation stage. C was found to be especially sensitive. With respect to this study, and due to minor changes in the biphasic model, and the addition of the triphasic model, T_{max}, R_P and R_a, were kept from the previous investigation of Hopkins [25]. This was done due to the fact that changes in these parameters were found to be far less significant compared to C. The calibration was hence carried forth using C. Referring to the target ESV value for the 2014 and 2016 models, as shown in Table (7.3), calibration of C was performed and may be viewed in Fig.(7.6).
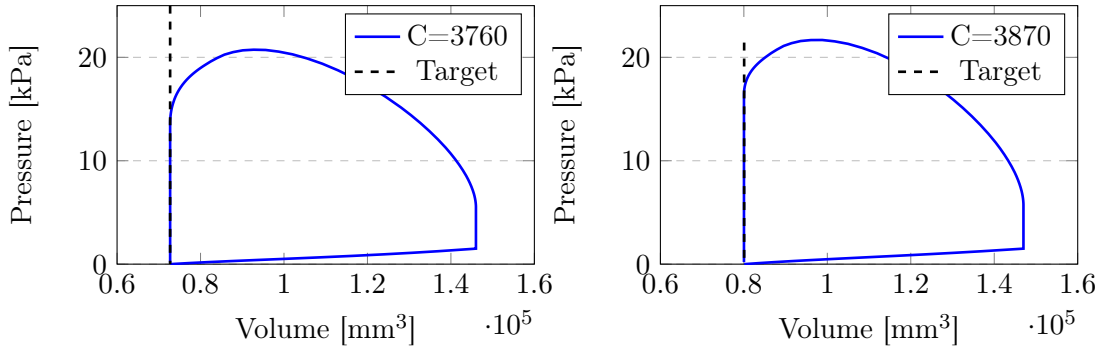

FIGURE 7.6: Calibration of 2014 (left) and 2016 (right) models, with
respect to various values of the arterial compliance C.

Consequently, the final calibrated values of C for the 2014 and 2016 models are 3760 and 3870, respectively. The final list of parameters for the active tension and Windkessel models may be viewed in Table.(7.5)

TABLE 7.5: Active tension and Windkessel maetrial parameters for the 2014 and 2016 cardiac models.

Material parameter	2014 Value	2016 value	Unit	Source
T_{max}	120	120	kPa	[25]
Ca_0	4.35	4.35	μm	[22]
$(Ca_0)_{max}$	4.35	4.35	μm	[22]
B	1048.9	1048.9	mm	[22]
l_0	-1.429	-1.429	μm	[22]
t_0	2400	2400	s	[25]
m	1.58	1.58	s/mm	[22]
b	0.22	0.22	ms	[22]
C	3760	3870	mm^3/kPa	-
R_a	$1.0 \cdot 10^{-4}$	$1.5 \cdot 10^{-4}$	$(kPa \cdot s)/mm^3$	[25]
R_p	$1.28 \cdot 10^{-5}$	$1.47 \cdot 10^{-5}$	$(kPa \cdot s)/mm^3$	[25]

7.3.3 Calibration of the growth model

Calibration of the cardiac models have so far been conducted with the condition of $\hat{\rho}^S = 0$. In order to create a model which may predict the effect of growth over the two year period between 2014 and 2016, the stretch driven growth function will be activated, hence allowing for the increase in length of the sarcomeres within the myocardium. It is expected that this inclusion will provide insight into the mechanical and thermodynamic changes of the heart, in a manner which is physiologically accurate. The method for demonstrating this was proposed by Hopkins [25], whereby the 2014 scan is used as an initial starting point. With the addition of growth, this model is then calibrated against the EDV and ESV values of the 2016 model. The parameter which will be calibrated comprises solely of the maximum mass exchange rate $\hat{\rho}^{max}$. Due to the fact that only $\hat{\rho}^{max}$ is used, calibration against the EDV and ESV will be done concurrently. Reaching target values which satisfy both terms is challenging, which is the reason why target points which agree to both points as much as possible will be accepted. By adopting the growth function parameters in accordance with Göktepe et al. [20], of which were selected specifically to model a dilated heart, the following list of values are proposed.

TABLE 7.6: Growth function parameters. [20]

J_{Sg}^{max}	ϵ_{max}	γ
1.5	1.001	1

Finally, the results yielded from the calibration of $\hat{\rho}^{max}$, may be viewed in Fig.(7.7).

As observed from Fig.(7.7), the ESV was far better calibrated against as compared to the EDV. However, the EDV was predicted within close range of the target value, attaining a value of 146.5 ml, with 0.34% error. As such, the final calibrated value of $\hat{\rho}^{max}$ was found to be $3.3 \cdot 10^{-5}$ kg/(mm$^3 \cdot$s).
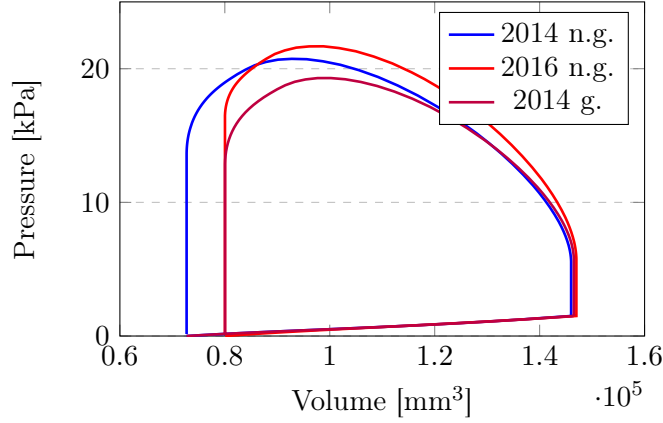
FIGURE 7.7: Calibration of the 2014 growth induced model (2014 g.)
with respect to the 2016 model simulated without growth (2016 n.g.),
and compared against the 2014 no-growth model (2014 n.g.)

7.4 Benchmarking

In order to investigate the proposed triphasic model, for the case of no growth $\hat{\rho}^{S} = 0$,
results will be compared to the existing cardiac mechanics toolbox within the in-house
built software SESKA. This will comprise of a comparison against the mechanical
aspect of the model. With respect to the newly proposed growth induced model and
the pore pressure results, benchmarking against the existing biphasic TPM model
within SESKA, will be carried out. Further comparisons will be made using results
accessed from literature attaining to cardiac modelling.

The results obtained from the 2014 and 2016 models, using the triphasic TPM
model and the classical continuum mechanics model, developed by Skatulla and San-
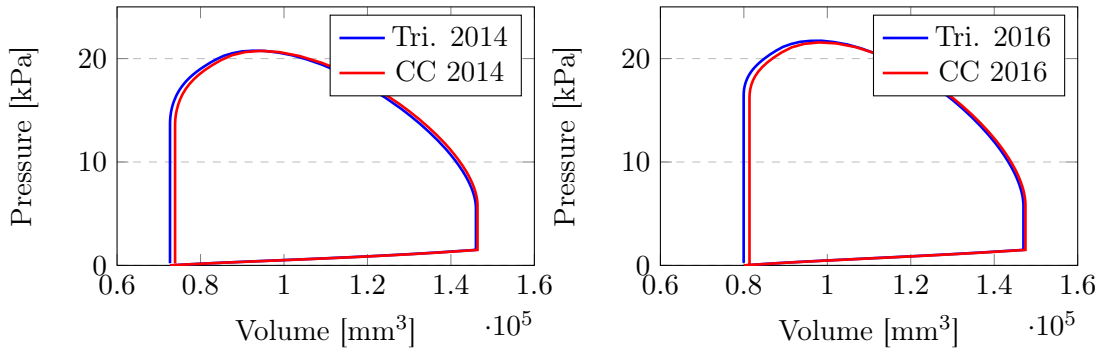sour [65], are shown in Fig.(7.8).

FIGURE 7.8: Benchmarking of the triphasic model, simulated without
the addition of growth (Tri.), against the standard cardiac mechan-
ics toolbox implemented within SESKA, which makes use of a classic
continuum mechanics framework (CC).

As observed in Fig.(7.8), the triphasic model matches closely to that of the classical
continuum model in terms of the pressure volume loop. The triphasic model appears
to have reduced ESV and EDV values. In addition, higher peak pressures are present
with the triphasic model. Due to the fact that, with the inclusion of the fluid phases,
and the condition that blood is constrained within the bounds of the heart, an increase
in stiffness could potentially be a result of this. However, the peak pressures are still

within close range, noting differences of 0.096 kPa and 0.251 kPa, for the 2014 and 2016 models, respectively.

In terms of the pore pressure results, comparisons are made with the existing biphasic model, of which was benchmarked against the work of Wall et al. [78]. With equivalent parameters, such that the fluid phase in the biphasic model is equal to the fluid (nutrient and liquid) in the triphasic model and the densities of the nutrient and liquid phase are also equal, it is expected that identical results be produced. This feature is noticed within the contour plot of the pore pressure at the end of the ejection phase, of which may be viewed in Fig.(7.9). For further evaluation of the pore pressure in relation to Wall et al. [78], refer to the work of Hopkins [25].
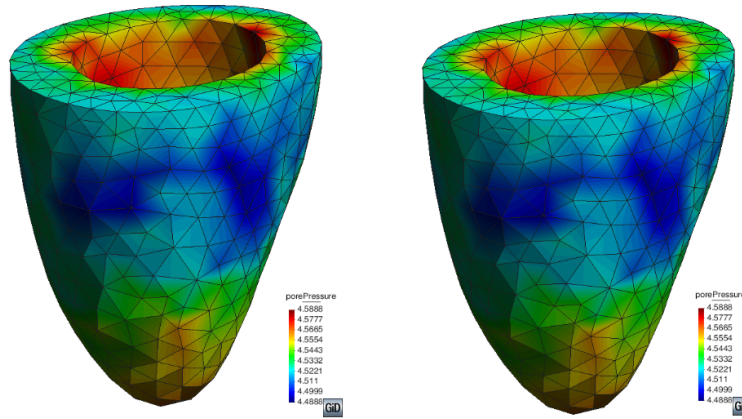

FIGURE 7.9: Comparison of the pore pressure contour plot results of the triphasic TPM model (left), with the existing biphasic TPM model (right).

Finally, benchmarking of the growth model will be done. The new growth function that was implemented was adapted from that of Goktepe et al. [20]. As such, the growth model will be firstly compared to the results published in the aforementioned journal article, of which may be seen by the contour plot of the growth Jacobian J_g at the end of diastolic filling in Fig.(7.10).
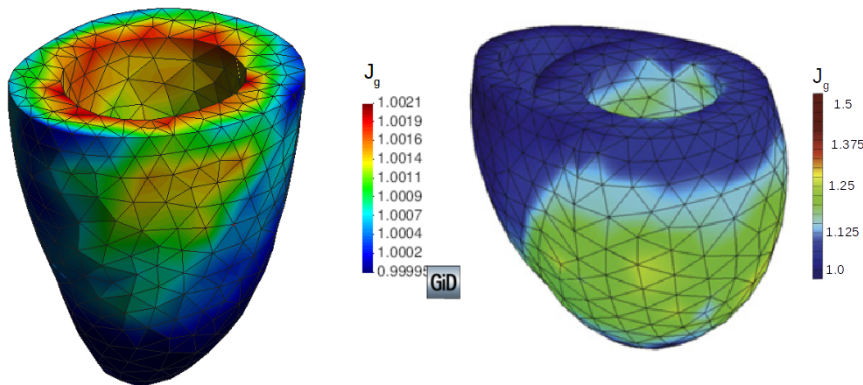

FIGURE 7.10: Benchmarking of the growth model (left), simulated to the point of EDV, and compared against results presented by Goktepe et al. [20] (right).

Overall, the pattern of the growth jacobian J_g results comply with those obtained by Goktepe et al. [20], especially within the middle section of the heart, where higher levels of growth are observed. This feature is expected during diastolic filling, as the fibres would elongate during myocardial expansion. It should be noted that, within the work of Goktepe et al. [20], a generic bi-ventricle model is used, as oppose to the patient-specific left ventricle model used within this study. As such, it is expected that differences will arise, such as, smoother and more ideal results, for example. Additionally, the base and free walls regions, where the right ventricle would be positioned, will be constrained less and will therefore experience greater levels of deformation, in its absence. Consequently, higher levels of growth are apparent along the edges of the base of the proposed 2014 growth model. The growth model was calibrated to the amount of growth that had occurred, with the heart of the patient under study, over the two year period between 2014 and 2016. As such, the levels growth are expected to be different.

Lastly, in order to study the effects that the growth induced model has on the pressure volume curve in relation to a TPM model, a comparison is done with the growth activated biphasic model [25]. As mentioned in the previous section regarding the calibration of the growth model and by referring to Fig.(7.7), an increase in ESV and EDV was noted. In addition, the SV appeared to decrease in a manner which complied with the pressure volume curve of the 2016 model. In terms of the biphasic model, implemented by Hopkins [25], the method of calculating the growth evolution and constitutive law for the mass supply function differed from those used in this study. However, for qualitative purposes, it should be noted that the exact relationship between the changes in ESV, EDV and SV, are found in the work of Hopkins [25]. Hence a direct comparison will not be shown, and one may rather refer to the aforementioned work.

7.5 Limitations relating to the patient-specific cardiac models

From the data shown in Table (7.3), it is apparent that an increase in EDV and ESV have occurred over the two year time interval. In addition, a reduction of the SV is observed. This information gathered from the two models correlates well with literature regarding the evolution of cardiac behaviour related to the condition of dilated cardiomyopathy, DCM, (or eccentric hypertrophy). It should be noted that, even though the patient was diagnosed as having sever mitral stenosis and regurgitation, both of which are understood to decrease ejection output. From the 2016 data, an increase in peak pressure is seen, as oppose to the decrease in pressure from the simulated growth model, of which is in accordance to the pressures developed in patients with DCM. In addition, from the cardiac models, it is apparent that an increase in thickness of the myocardium had occurred between 2014 and 2016, which indicates that a degree of concentric hypertrophy had developed. Due to surgical intervention in 2015, which involved replacement of the mitral valve, certain conditions might have been altered. As such, due to the fact that the proposed growth model is designed to simulate the condition of DCM, it should be understood that there are limitations in relation to the comparison of results between the growth model, and the 2016 model simulated without growth.

With respect to the condition of mitral regurgitation, as discussed in Chapter 2, at the onset of systole, during which pressures develop during the contraction stage, blood is able flow across the mitral valve due to the impairment. Hence, this results

in there being no true isovolumetric contraction stage. It should be noted that the proposed TPM model is not able to simulate this feature, and hence lies outside the scope of this investigation. [34]

From Chapter 2, it was discussed that cardiac dilation could be a maladaptive response to mitral or aortic regurgitation, in relation to valve impairment [34] . However, as highlighted, these two valve impairments result in different physiological changes, of which is apparent in the shape of the pressure-volume curves of the respective conditions, see Sec.(2.3). As such, it should be noted that the proposed growth model corresponds to the general case of DCM, shown by Fig.(2.10), and can therefore not differentiate between aortic and mitral regurgitation.

7.6   Analysis of the growth induced model

So far within this investigation, two model geometries have been simulated, corresponding to two different time periods, namely in the years of 2014 and 2016. These difference in results attaining to these models are meant to signify how the condition has worsened over the two year time period. The growth model discussed in the last section was implemented such that it would be able to predict the physiological changes that occurred between the interval, in terms of the mechanical and thermodynamic behaviour. As discussed in Sec.(7.5), the 2016 geometrical model poses some issues in relation to the comparison with the growth induced triphasic model. Even though the growth model was calibrated to meet the target values of the EDV, ESV and SV of the 2016 model (of which is in agreement with the changes expected in DCM diagnosed patients), the peak pressure of the 2016 model does not correspond to the typical case of DCM in terms of the pressures developed within the ejection phase. Hence, a direct comparison of the growth model and 2016 model is not entirely meaningful. As such, this section will continue with a comparison of the initial state of the 2014 model, simulated without growth, and the growth induced model.

7.6.1   Analysis of the pressure-volume curves

After simulating the 2014 model with and without mass supply, over one heart beat, the following results were produced, as shown in Table (7.7)

TABLE 7.7: Cardiac results pertaining to the 2014 model, simulated with and without growth.

Parameter	2014 no growth	2014 growth induced	Unit
EDV	146	146.5	ml
ESV	72	80.0	ml
SV	74	66.5	ml
EDPVR gradient	28.0	26.4	Pa/ml
Peak pressure	20.8	19.4	kPa

From the data shown in the table above, it is apparent that a deterioration in the condition of the patient has occurred. The increase in EDV and ESV, with respect to the growth induced model, is an indication of the increase in volume which has occurred as a result of growth. In addition, the growth induced model appears to have reduced in peak pressure by 1.4 kPa, which denotes that the hearts ejection capacity

has reduced, of which is analogous to the condition of DCM. The enlargement of the heart due to DCM has an effect on the mechanical function, whereby weakening of the muscles is generally observed [34]. This deficiency may also be noted by the reduction in SV, which correlates with the amount of blood ejected out the cavity into the various circulatory systems. Another feature which highlights the presence of DCM is the end diastolic pressure volume relationship EDPVR, given in terms of the slope at the point of EDV. In the case of DCM, the EDPVR gradient is generally observed to decrease, which signifies a decrease in vascular stiffness and hence a debilitation of the cardiac tissue [34, 1]. This is in agreement to the results shown in Table (7.7), whereby the EDPVR is seen to reduce by 2.4 Pa/ml with the addition of growth. [34]

7.6.2   Changes in mechanical behaviour

Dilated cardiomyopathy results in mechanical and functional changes in the left ventricle. Understanding the abnormalities which occur may be found in analyzing the stresses and strains that the heart experiences within the myocardial tissue during its activity. This section will comprise an observation of the fibre stresses and strains of the initial state of the heart, simulated using the 2014 geometrical model with no mass supply, and compared against that using the growth induced model. For the purpose of illustrating this, the fibre stress and strain within the mid section of the heart, and along the outer surface of the epicardium, will be focused on. This data is shown in Fig.(7.11).

From the depiction of the pressure-volume curve in Fig.(7.7), of which is represented quantitatively in Table (7.7), the growth induced model indicated that the ejection capacity had been compromised as a result of weakened muscle fibres due to dilation of the heart. It is expected that this reduction in mechanical load will coincide with the stresses and strains of the myocardium, of which is confirmed through analysis of Fig.(7.11). From Fig.(7.11), it may be seen that during diastolic filling, at a point where minimal growth has developed, the fibre stress and strain of the two models, occur in tandem. However, as the amount of growth increases due to stretching of the sarcomeres, the stress and strain of the growth induced model is seen to reduce. The pattern and values of the strains, shown in Fig.(7.11), is analogous to that presented in the work of Yu et al. [87], where a reduction of strains were documented in relation to an evaluation of left ventricular behaviour in patients with dilated cardiomyopathy.
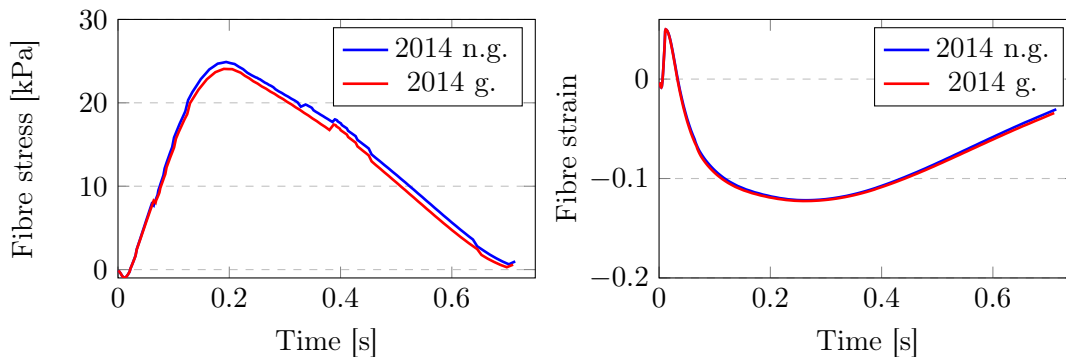

FIGURE 7.11: Fibre stress (left), and fibre strain (right), results generated from the growth induced and standard 2014 model.

In terms of the theory of porous media, the perfusion effects are greatly influenced by the mechanical action that the heart is subjected to. As such, following the description of the stresses and strains, the pore pressure is a feature which is important in describing the physiological changes which occur as a result of growth, as it has direct influence on the fluid interaction of the system. It may be understood that with a decrease in stress and strain, as a result of the inclusion of growth and remodelling, the pore pressure is expected to behave in a synchronous manner. This relationship may be viewed in the graph which denotes the evolution of the pore pressure against time over one cardiac cycle, as shown by Fig.(7.12). After an initial increase, the pore pressure is observed to decrease during diastolic filling. This reduction may be attributed to the stretching of the muscle fibres, of which would translate into expanded pore spaces. As the ejection phase is initiated, and the heart contracts, the pore spaces would similarly shrink in size, of which would therefore increase the pore pressure until the relaxation phase begins, whereby a stabilization of the pore pressure towards the initial state would then take place.
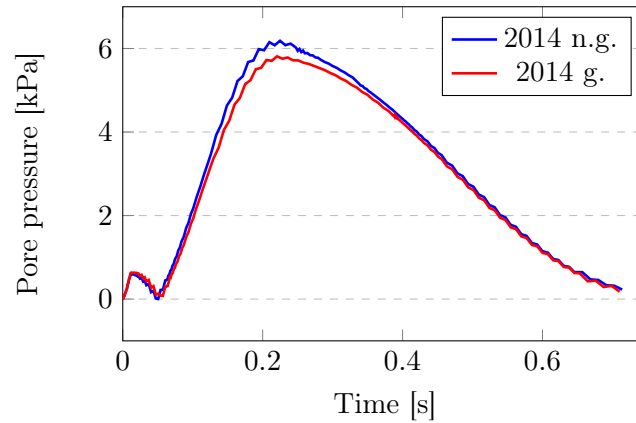

FIGURE 7.12: Pore pressure evolution, over a full cardiac cycle, which displays the relationship between the growth induced and standard 2014 model.

7.6.3 Changes in the volume fraction quantities

Predicting how the densities of the various constituents change within the myocardium of the heart in relation to conditions which result in growth and remodelling is an important aspect. Left ventricular dilation may be characterized by a weakening or destruction of tissue within the myocardium [30]. This degradation or infarction of the myocardium, may occur regionally across the heart and usually correlates to abnormalities associated with a starvation of nutrients (such as oxygen supply). In addition, it is understood that with hypertrophy of cardiomyocites related to growth, an increase in the density of the solid tissue occurs, of which results in a reduced relative blood-tissue ratio [9, 28]. Consequently, a stiffening of the cardiac tissue may arise in these infarcted areas, from the increase in tissue density, of which may furthermore lead to impaired ventricular function and heart failure [30].

A therapeutic method of treating infarcted hearts is through region-specific injection of hydrogels, which act to mitigate the effects of growth proliferation, as demonstrated in the works of Wu et al. [85] and Waters et al. [79]. Using this method allows direct targeting of specific diseased areas of the heart, of which is seen as an efficient form of therapy [79]. With respect to the theory of porous media, a study comprising

of the evolution of the solid and nutrient volume fractions, may provide strong indication to how the condition of rheumatic heart disease may physiologically effect certain patients. Hence, through this study, insight into the regions of the heart which may potentially be at risk of myocardial infarction may be uncovered, of which may allow for early treatment in patients suffering with conditions associated with growth and remodelling of the heart.

Fig.(7.13) illustrates the relationship between the the sarcomere length, growth Jacobian J_g and the solid volume fraction n^S. For the case of DCM, a stretch induced growth function is employed. Hence, the degree of growth may be closely related to the sarcomere length, of which also then has influence in relation to n^S. This relation is apparent through observation of Fig.(7.13), whereby high values across all three parameters are viewed to occur at the top portion of the myocardium, in particular, at the end of diastolic filling. As the ventricular cavity fills, the region near the base will experience greater levels of deformation, which hence translates into higher strains exerted on the sarcomeres. In addition to growth, the volume
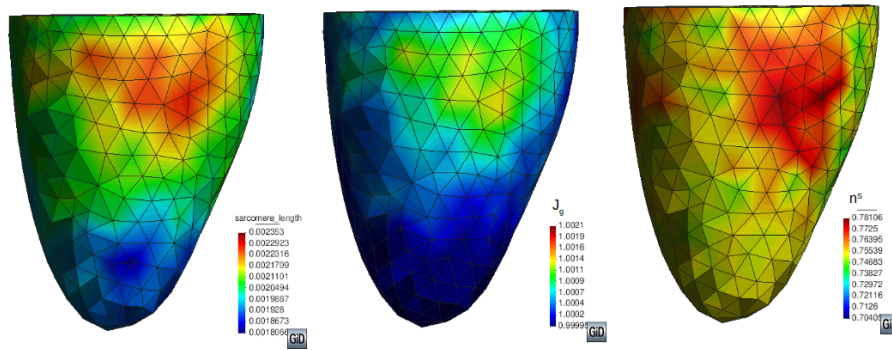

FIGURE 7.13: Illustration of the sarcomere length, growth Jacobian and solid volume fraction, at EDV.

fraction quantities are controlled by mechanical and fluid action (as may be seen by the weak forms in Chapter 6). However, in regions which experience greater levels growth, the effect of the mass supply on the volume fraction quantities may be made more apparent. Hence, to demonstrate the effect of the inclusion of growth on the solid and nutrient volume fractions, an evolution of these parameters over an entire cardiac cycle, measured at the point which displayed the greatest level of growth, was conducted and is presented graphically in Fig.(7.14). In addition, the point evolution of the growth Jacobian J_g, is shown in Fig.(7.15).

From Fig.(7.14) and Fig.(7.15), it may be observed that with an increase in growth, an overall reduction in the blood-tissue ratio occurs. During diastolic filling and early parts of the IVC, during which the amount of growth is still minimal, the blood-tissue ratio is seen to increase. This feature is influenced by the mechanical loads exerted on the heart within that phase of the cardiac cycle, whereby the heart expands due to diastolic filling and an overall stretching of the muscle fibres occurs. This expansion of tissue, in context of TPM, would thus result in the increase in size of the pore spaces and fluid volume. This would therefore translate into an increased fluid density and a reduced tissue density, within that region of the heart. As the contraction stage is initiated however, and with an increase in J_g, the tissue density increases at a decreasing rate that is analogous to the rate of change of J_g. A similar increase in n^S during contraction is noted with the simulated 2014 model without the inclusion of growth. As the pore spaces contract, the pore pressure would increase, causing the
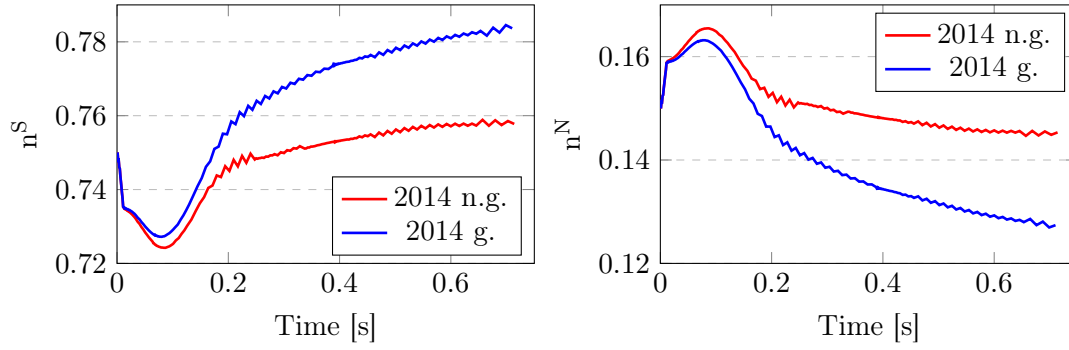
FIGURE 7.14: Evolution of the solid and nutrient volume fraction quantities, over a complete cardiac cycle, for the case of growth and no-growth.
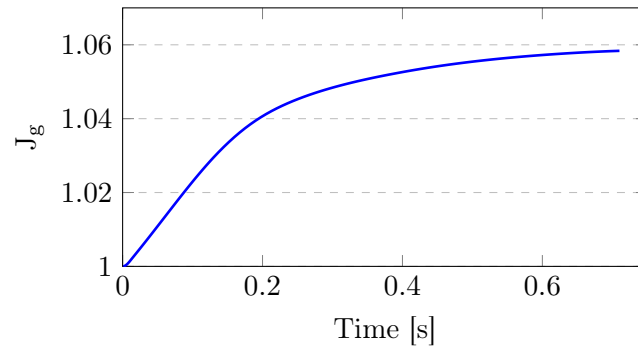

FIGURE 7.15: Progression of the growth Jacobian J_g, over a full cycle, at the point which displayed maximum growth.

fluid to be dispelled. This would hence result in an increased relative tissue density. It may be observed that the magnitude of the increase in n^S, for the standard model, as compared to the growth induced model, is far less. It is hence apparent that the relative magnitude of the increase in tissue density, between the standard and growth induced models, is influenced greatly by the mass supply function. In addition, with the standard model, the volume fractions are observed to stabilize, once the heartbeat is complete, of which conveys a return to the reference state. In contrast, with respect to the growth induced model, higher values of n^S are noted at the end of the heartbeat, compared to those at the beginning of the simulation, of which signifies permanent tissue growth.

It should be noted that the newly implemented growth law performed adequately and efficiently throughout the simulation of one heart beat. In addition, there seemed to be no issues in relation to the evolution of growth during the IVC and IVR phases of the heart beat, of which was experienced in the work of Hopkins [25]. This may hence suggest that the new growth function is an improved one.

Inclusion of the nutrient phase was motivated on the basis that more control over the depletion of the total fluid volume, as a result of growth, would be realised. This was done by coupling the mass supply function solely between the solid tissue phase and the nutrient phase. As such, during simulation of the growth induced model, it is expected that the liquid volume will be consumed less as compared to the nutrient quantity. Table (7.8) displays the final volume fraction values, obtained at the end of the simulation, between the growth induced and standard triphasic models.

From Table (7.8), it may be observed that the contribution towards growth of

TABLE 7.8: Volume fraction values at the end of the cardiac cycle, using the standard and growth TPM models. Changes in the volume fraction quantities and the percent contribution of the fluid phases towards the solid volume are also presented

Parameter	n^S	n^N	n^L
Standard model v.f.	0.758	0.146	0.096
Growth model v.f.	0.784	0.127	0.089
Change in v.f.	0.026	-0.019	-0.007
% fluid contribution	-	73%	27%

the tissue phase, is greater with respect to the nutrient phase as compared to the liquid phase. The nutrient phase was found to add 73% to the tissue volume fraction increase, whilst the liquid phase only added 27%. This result agrees with the expected assumption that the nutrient phase will deplete more during growth. However, the reason that n^L decreases with growth may be described mathematically from the mass supply terms shown in the strong forms. From Table (7.2), it may be noted that the fluid constituents have a higher density in comparison with the solid tissue constituent. In terms of the strong forms related to the solid and nutrient phases, as shown by Eq.$(4.10)_1$ and Eq.$(4.10)_3$, respectively, the effect of the mass supply function on the volume fractions is dependent on the corresponding densities. This is motivated by the concept that the nutrient phase would contain more mass per unit volume as compared to the solid tissue phase. As such, a decrease in n^N would result in a greater increase in n^S. Therefore, in order to satisfy the saturation condition, a reduction in n^L must also take place. Although a reduction in n^L is unexpected, it is still observed to be significantly less compared to the percent change in n^N, of which satisfies the main purpose of adding the third phase. A solution to making the growth fully dependent on the solid and nutrient volume fractions may lie in adapting the balance equations, and the term containing the mass supply function specifically.

Chapter 8

Conclusions and recommendations

This chapter will highlight the conclusions drawn in relation to the implementation of the triphasic TPM model, and its application to the example of a patient specific heart model. Following this, a list of recommendations will be discussed with respect to future work application.

This research consisted of implementing a triphasic framework, based on the Theory of Porous Media. This was firstly achieved by extending the current biphasic model present within the in-house built solid mechanics software SESKA. An additional degree of freedom was included, in the form of a nutrient volume fraction, of which allowed for mass exchange in context of growth and remodelling proliferation. Mass supply was induced through a stretch driven growth function and was implemented using an adapted method developed by Werner [80]. Furthermore, the triphasic model was coupled with the cardiac mechanics model present within SESKA and was hence used to simulate patient specific models in relation to Rheumatic Heart Disease.

From the results shown in Sec.(6.5), of which were successfully compared against the biphasic TPM model and the work of Hopkins [25], it may be concluded that the triphasic model, with the inclusion of the newly implemented mass supply function, has been successfully implemented, whereby qualitatively reasonable results were observed between the pore pressure, displacement and volume fraction, degrees of freedom.

With respect to the results attained in relation to the patient specific heart models, the triphasic model performed adequately, and produced results which were in agreement to the biphasic model and various other results attained from literature. Two models were initially studied, pertaining to CMR scans taken in 2014 and 2016. Calibration of these models were firstly conducted using parameters obtained from the work of Hopkins [25], and by using experimental end diastolic and end systolic volume data (of which was accessed through [25]). Calibration of the growth model was achieved by simulating the 2014 heart model, with the inclusion of mass supply, and by varying the maximum growth factor $\hat{\rho}^{\mathrm{max}}$, till the EDV and ESV results coincided with those from the 2016 model. Furthermore, benchmarking of the triphasic model was conducted against the biphasic model and the classical continuum mechanics model, with respect to the pore pressure and pressure volume curves, respectively. Additionally, the growth function was benchmarked against the work of Goktepe et al. [20], as shown in Sec.(7.4). Even though the problem type differed in the work Goktepe et al. [20], reasonable comparisons were observed.

It was observed that, while the patient under study was diagnosed with dilated cardiomyopathy and, mitral stenosis and regurgitation, the results of the 2016 model did not correlate entirely with the given set of conditions. Surgical intervention was performed on the patient prior to CMR scanning in 2015. Hence, it was deduced

that physiological changes within the heart must have taken place in the in the post-surgery interval. As such, a continuation of the analysis of the growth model was done in absence of the 2016 model.

The results produced by the 2014 model, simulated with growth, matched up closely to those expected in dilated hearts. This was seen by the increase in ESV and EDV results, of which indicated an increase in cavity volume in states of rest and at maximum capacity, respectively. In addition, reductions in the SV, peak pressure, and the EDPVR gradient, were observed in the 2014 growth model, of which conveyed a reduced pumping capacity and weakening of the heart tissue, and are typical characteristics related to DCM. Reductions in pore pressures, and fibre stresses and strains were additionally noted, of which correlated with observations documented in the work of Yu et al. [87]. As such, it may hence be concluded that the triphasic growth induced model may be sufficiently used to model hearts associated with DCM.

One of the key objectives of this research was to implement the third phase, such that it would contribute to the mass exchange process and would therefore control the volume levels of the liquid constituent. In Sec.(7.6.3) it was found that with growth, a slight reduction in n^L occurred, of which was found to stem from the mathematical construct of the balance equations. However, the reduction in n^L was observed to be minute in relation to the reduction in n^N, whereby the overall objective was still satisfied.

Various aspects need to be addressed in terms of continuing research into modelling rheumatic hearts using TPM as a mathematical framework. To avoid repetition, one may firstly refer to the recommendations suggested by Hopkins [25]. The recommendations to be put forth in this work consist of the following.

Firstly, the CMR scans that the CCM have access to usually consist of an initial scan of the patient's heart, generally taken at a point where the condition is at an advanced level, and a follow-up scan after valve replacement surgery, taken to assess if conditions are improving. Hence, an area of research could be presented in developing constitutive growth laws which act to reverse the effects of growth. This would hence make use of the follow-up scan as a benchmark model, after which predictions into how the condition might evolve in subsequent time periods may then be conducted.

The second suggestion, which relates to the first, focuses on treating myocardial infarction using hydrogels, as was discussed in Sec.(7.6.3). The third phase could be substituted as a hydrogel, which acts to mitigate and reduce the effects of myocardial infarction. In terms of volume fraction quantities the solid and hydrogel quantities would need to be consumed, resulting in an increased fluid volume, in order to restore a more sufficient blood-tissue ratio. In addition, using prescribed flux boundary conditions, certain areas may be targeted specifically. This method would therefore also involve the concept of reverse growth modelling.

In order to address the issue related to the decreasing liquid volume fraction during growth, an adaptation of the balance equation may be conducted in order to fully couple the growth between the solid and nutrient volume fractions. This may be achieved by removing the weighting components that comprise of the respective densities in the terms containing the mass supply function in equations $(4.10)_1$ and $(4.10)_3$.

Finally, the model was found to comply specifically with the general case of DCM, and not with those associated with valvular dysfunction. This may be attributed to the fact that with the latter condition, true isovolumetric relaxation and contraction stages do not exist. One method of overcoming this limitation would entail modifying the volume driven algorithm related to the isovolumetric phases, such that $\Delta V \neq 0$.

Furthermore, conditions would need to be developed to differentiate dilation caused by aortic or mitral regurgitation.

Appendix A

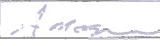# Ethics approval

APPLICATION FORM

Please Note:
Any person planning to undertake research in the Faculty of Engineering and the Built Environment (EBE) at the University of Cape Town is required to complete this form before collecting or analysing data. The objective of submitting this application *prior* to embarking on research is to ensure that the highest ethical standards in research, conducted under the auspices of the EBE Faculty, are met. Please ensure that you have read, and understood the **EBE Ethics in Research Handbook** (available from the UCT EBE, Research Ethics website) prior to completing this application form: http://www.ebe.uct.ac.za/ebe/research/ethics1

APPLICANT'S DETAILS		
Name of principal researcher, student or external applicant		ADAM MOSAM
Department		CIVIL ENGINEERING
Preferred email address of applicant:		MSMADA002@MYUCT.AC.ZA
If Student	Your Degree: e.g., MSc, PhD, etc.	MSc
	Credit Value of Research: e.g., 60/120/180/360 etc.	120
	Name of Supervisor (if supervised):	A/PROF. SEBASTIAN SKATULLA
If this is a research contract, indicate the source of funding/sponsorship		NRF FUNDING
Project Title		A tri-phasic continuum model for the numerical analysis of biological tissue proliferation using the Theory of Porous Media. Application to cardiac remodelling in rheumatic heart disease

I hereby undertake to carry out my research in such a way that:

- there is no apparent legal objection to the nature or the method of research; and
- the research will not compromise staff or students or the other responsibilities of the University;
- the stated objective will be achieved, and the findings will have a high degree of validity;
- limitations and alternative interpretations will be considered;
- the findings could be subject to peer review and publicly available; and
- I will comply with the conventions of copyright and avoid any practice that would constitute plagiarism.

SIGNED BY	Full name	Signature	Date
Principal Researcher/ Student/External applicant	ADAM MOSAM		26/09/2018

APPLICATION APPROVED BY	Full name	Signature	Date
Supervisor (where applicable)	A/PROF. SEBASTIAN SKATULLA		26/09/2018
HOD (or delegated nominee) Final authority for all applicants who have answered NO to all questions in Section 1; and for all Undergraduate research (including Honours).	DG RANDALL		2 OCT 2018
Chair : Faculty EIR Committee For applicants other than undergraduate students who have answered YES to any of the above questions.			

Bibliography

[1] ADInstruments. *How is a dilated cardiomyopathy characterized by left ventricle pressure volume loops?* URL: https://www.adinstruments.com/support/knowledge-base/how-dilated-cardiomyopathy-characterized-left-ventricle-pressure-volume-loops.

[2] Hugh D Allen et al. *Moss & Adams' Heart Disease in Infants, Children, and Adolescents: Including the Fetus and Young Adult.* Lippincott Williams & Wilkins, 2013.

[3] D Ambrosi et al. "Perspectives on biological growth and remodeling". In: *Journal of the Mechanics and Physics of Solids* 59.4 (2011), pp. 863–883.

[4] Tiia Anmann et al. "Calcium-induced contraction of sarcomeres changes the regulation of mitochondrial respiration in permeabilized cardiac cells". In: *FEBS Journal* 272.12 (2005), pp. 3145–3161. ISSN: 1742464X.

[5] George Francis Atkinson. *Lessons in botany.* H. Holt, 1900.

[6] O Bernus, M Wellner, and A M Pertsov. "Intramural wave propagation in cardiac tissue: Asymptotic solutions and cusp waves". In: *Physical Review E - Statistical Physics, Plasmas, Fluids, and Related Interdisciplinary Topics* 70.6 (2004), p. 7. ISSN: 1063651X.

[7] Roberto Burattini, Grant G Knowlen, and Kenneth B Campbell. "Two arterial effective reflecting sites may appear as one to the heart". In: *Circ Res* 68.1 (1991), pp. 85–99.

[8] Rudolf Clausius. "Über eine veränderte Form des zweiten Hauptsatzes der mechanischen Wärmetheorie". In: *Annalen der Physik* 169.12 (1854), pp. 481–506.

[9] Jack P.M. Cleutjens et al. *The infarcted myocardium: Simply dead tissue, or a lively target for therapeutic interventions.* 1999.

[10] Bernard D. Coleman and Walter Noll. "The thermodynamics of elastic materials with heat conduction and viscosity". In: *Archive for Rational Mechanics and Analysis* 13.1 (1963), pp. 167–178. ISSN: 00039527.

[11] Vincent Creigen et al. "Modeling a heart pump". In: *European Study Group Mathematics with Industry* (2007), p. 7.

[12] J.D. Cutnell et al. *Physics, 10th Edition.* Wiley, 2015. ISBN: 9781118899205.

[13] Reint De Boer. *Theory of porous media: highlights in historical development and current state.* Springer Science & Business Media, 2012.

[14] Socrates Dokos et al. "Shear properties of passive ventricular myocardium". In: *American Journal of Physiology-Heart and Circulatory Physiology* 283.6 (2002), H2650–H2659. ISSN: 0363-6135.

[15] W Ehlers et al. "Continuum biomechanics applied to the human intervertebral disc". In: *PAMM* 5.1 (2005), pp. 27–30.

[16] Wolfgang Ehlers and Joachim Bluhm. *Porous media: theory, experiments and numerical applications.* Springer Science & Business Media, 2013.

[17] Wolfgang Ehlers and Joachim Bluhm. *Porous media: theory, experiments and numerical applications*. Springer Science & Business Media, 2013.

[18] Gernot Eipper. "Theorie und Numerik finiter elastischer Deformationen in fluidgesättigten porösen Festkörpern". PhD thesis. Inst. für Mechanik (Bauwesen), 1998.

[19] Mohammed Asaad Essack. "Material Parameter Identification for Modelling the Left Ventricle in the Healthy State". PhD thesis. 2014, p. 1.

[20] Serdar Göktepe, Oscar John Abilez, and Ellen Kuhl. "A generic approach towards finite growth with examples of athlete's heart, cardiac dilation, and cardiac wall thickening". In: *Journal of the Mechanics and Physics of Solids* 58 (2010), pp. 1661–1680.

[21] Alain Goriely and Martine Ben Amar. "On the definition and modeling of incremental, cumulative, and continuous growth laws in morphoelasticity". In: *Biomechanics and Modeling in Mechanobiology* 6.5 (2007), pp. 289–296.

[22] J M Guccione and A. D. McCulloch. "Mechanics of active contraction in cardiac muscle: Part I–Constitutive relations for fiber stress that describe deactivation." In: *Journal of biomechanical engineering* 115.1 (1993), pp. 72–81. ISSN: 01480731. arXiv: arXiv:1011.1669v3.

[23] John E Hall. *Guyton and Hall textbook of medical physiology e-Book*. Elsevier Health Sciences, 2015.

[24] G Himpel et al. "Computational modelling of isotropic multiplicative growth". In: *Comp Mod Eng Sci* 8 (2005), pp. 119–134.

[25] Gary Hopkins. "Department of Civil Engineering Growth , Modelling and Remodelling of Cardiac Tissue : A Multiphase Approach". In: (2017).

[26] Human Anatomy System. *Microscopic Anatomy Of Cardiac Muscle Microscopic Anatomy Of Cardiac Muscle Ocr A Level Biology - Human Anatomy System*. URL: https://www.anatomylibrary.us/microscopic-anatomy-of-cardiac-muscle/microscopic-anatomy-of-cardiac-muscle-microscopic-anatomy-of-cardiac-muscle-ocr-a-level-biology/ (visited on 07/10/2018).

[27] Paul A. Iaizzo. *Handbook of cardiac anatomy, physiology, and devices, third edition*. 2015, pp. 1–817. ISBN: 9783319194646. arXiv: arXiv:1011.1669v3.

[28] Andreas Indermühle et al. "The relative myocardial blood volume differentiates between hypertensive heart disease and athlete's heart in humans". In: *European Heart Journal* 27.13 (2006), pp. 1571–1578. ISSN: 0195668X.

[29] Lihua Jin, Shengqiang Cai, and Zhigang Suo. "Creases in soft tissues generated by growth". In: *EPL (Europhysics Letters)* 95.6 (2011), p. 64002.

[30] Arnold M. Katz. *Physiology of the Heart: 4th Edition*. 2001, p. 576. ISBN: 1608311716.

[31] R. C.P. Kerckhoffs et al. "Homogeneity of cardiac contraction despite physiological asynchrony of depolarization: A model study". In: *Annals of Biomedical Engineering* 31.5 (2003), pp. 536–547. ISSN: 00906964.

[32] Roy C P Kerckhoffs, Jeffrey H Omens, and Andrew D Mcculloch. "A single strain-based growth law predicts concentric and eccentric cardiac growth during pressure and volume overload". In: *Mechanics Research Communications* 42 (2011), pp. 40–50.

[33] Roy C.P. Kerckhoffs et al. "Computational methods for cardiac electromechanics". In: *Proceedings of the IEEE* 94.4 (2006), pp. 769–782. ISSN: 00189219.

[34] Richard E Klabunde. "Cardiovascular Physiology Concepts". In: *Lippincott Williams & Wilkins* (2004), p. 256. ISSN: 14337851. arXiv: arXiv:1011.1669v3.

[35] Robert Friedrich Krause. "Growth, modelling and remodelling of biological tissue". In: (2014).

[36] E Kuhl et al. "Computational modeling of arterial wall growth". In: *Biomechanics and modeling in mechanobiology* 6.5 (2007), pp. 321–331.

[37] Ellen Kuhl. "Growing matter: A review of growth in living systems". In: *Journal of the Mechanical Behavior of Biomedical Materials* 29 (2014), pp. 529–543. ISSN: 17516161.

[38] Vinay Kumar et al. *Robbins and Cotran pathologic basis of disease.* 2005.

[39] Peter Lancaster and Kes Salkauskas. *Surface generated by moving least square methods.* 1981.

[40] Erastus H Lee. "Elastic-plastic deformation at finite strains". In: *Journal of applied mechanics* 36.1 (1969), pp. 1–6.

[41] D. Legner et al. "Studying the influence of hydrogel injections into the infarcted left ventricle using the element-free Galerkin method". In: *International Journal for Numerical Methods in Biomedical Engineering* 30.3 (2014), pp. 416–429. ISSN: 20407939.

[42] Bo Li et al. "Mechanics of morphological instabilities and surface wrinkling in soft materials: a review". In: *Soft Matter* 8.21 (2012), pp. 5728–5745.

[43] Lumen Learning. *Mammalian Heart and Blood Vessels / Boundless Biology.* URL: https://courses.lumenlearning.com/boundless-biology/chapter/mammalian-heart-and-blood-vessels/ (visited on 06/25/2018).

[44] Marjorie Maillet, Jop H Van Berlo, and Jeffery D Molkentin. "HHS Public Access". In: 14.1 (2015), pp. 38–48.

[45] Eloi Marijon et al. "Rheumatic heart disease". In: *The Lancet* 379.9819 (2012), pp. 953–964. ISSN: 0140-6736.

[46] Julia Mascherbauer et al. "Value and limitations of aortic valve resistance with particular consideration of low flow–low gradient aortic stenosis: an in vitro study". In: *European heart journal* 25.9 (2004), pp. 787–793.

[47] Andreas Menzel and Ellen Kuhl. "Frontiers in growth and remodeling". In: *Mechanics Research Communications* 42 (2012), pp. 1–14.

[48] Derek E Moulton and Alain Goriely. "Possible role of differential growth in airway wall remodeling in asthma". In: *Journal of applied physiology* 110.4 (2011), pp. 1003–1012.

[49] Van C Mow, Mark H Holmes, and W Michael Lai. "Fluid transport and mechanical properties of articular cartilage: a review". In: *Journal of biomechanics* 17.5 (1984), pp. 377–394.

[50] H Narayanan et al. "In silico estimates of the free energy rates in growing tumor spheroids". In: *Journal of Physics: Condensed Matter* 22.19 (2010), p. 194122.

[51] Martyn P Nash and Alexander V Panfilov. "Electromechanical model of excitable tissue to study reentrant cardiac arrhythmias". In: *Progress in biophysics and molecular biology* 85.2-3 (2004), pp. 501–522.

[52] Serdar Oktepe et al. "A multiscale model for eccentric and concentric cardiac growth through sarcomerogenesis ARTICLE IN PRESS". In: *Journal of Theoretical Biology* 265 (2010), pp. 433–442.

[53]   Lionel H Opie et al. *Controversies in ventricular remodelling.* 2006.

[54]   MICHAEL F O'Rourke. "Pressure and flow waves in systemic arteries and the anatomical design of the arterial system." In: *Journal of applied physiology* 23.2 (1967), pp. 139–149.

[55]   Frank Otto. "Die grundform des arteriellen pulses". In: *Zeitung fur Biologie* 37 (1899), pp. 483–586.

[56]   Ritesh Rama. "Proper Orthogonal Decomposition with Interpolation-based Real-time Modelling of the Heart". PhD thesis. University of Cape Town, 2017.

[57]   M K Rausch et al. "Computational modeling of growth: systemic and pulmonary hypertension in the heart". In: *Biomech Model Mechanobiol* 10 (2011), pp. 799–811.

[58]   Tim Ricken and Joachim Bluhm. "Remodeling and growth of living tissue: A multiphase theory". In: *Archive of Applied Mechanics* 80.5 (2010), pp. 453–465. ISSN: 09391533.

[59]   Tim Ricken, Alexander Schwarz, and Joachim Bluhm. "A triphasic model of transversely isotropic biological tissue with applications to stress and biologically induced growth". In: *Computational Materials Science* 39.1 SPEC. ISS. (2007), pp. 124–136. ISSN: 09270256.

[60]   Edward K Rodriguez, Anne Hoger, and Andrew D McCulloch. "Stress-dependent finite growth in soft elastic tissues". In: *Journal of biomechanics* 27.4 (1994), pp. 455–467.

[61]   Damien Rohmer, Arkadiusz Sitek, and Grant T Gullberg. "Reconstruction and visualization of fiber and laminar structure in the normal human heart from ex vivo diffusion tensor magnetic resonance imaging (DTMRI) data". In: *Investigative Radiology* 42.11 (2007), pp. 777–789. ISSN: 0020-9996.

[62]   Wayne Rosamond et al. "21. Glossary". In: *Circulation* 115.5 (2007), e69–e171.

[63]   Frank B Sachse et al. "Quantitative reconstruction of cardiac electromechanics in human myocardium: assembly of electrophysiologic and tension generation models". In: *Journal of cardiovascular electrophysiology* 14 (2003), S210–S218.

[64]   R Skalak et al. "Analytical description of growth". In: *Journal of theoretical biology* 94.3 (1982), pp. 555–577.

[65]   S. Skatulla and C. Sansour. "On a path-following method for non-linear solid mechanics with applications to structural and cardiac mechanics subject to arbitrary loading scenarios". In: *International Journal of Solids and Structures* 96 (2016), pp. 181–191. ISSN: 00207683.

[66]   Nicolas P Smith, Martin L Buist, and Andrew J Pullan. "Altered T wave dynamics in a contracting cardiac model". In: *Journal of cardiovascular electrophysiology* 14 (2003), S203–S209.

[67]   L Socci et al. "An axisymmetric computational model of skin expansion and growth". In: *Biomechanics and modeling in mechanobiology* 6.3 (2007), pp. 177–188.

[68]   Olga Solovyova et al. "Mechanical interaction of heterogeneous cardiac muscle segments in silico: effects on Ca 2+ handling and action potential". In: *International Journal of Bifurcation and Chaos* 13.12 (2003), pp. 3757–3782.

[69]   Gerhard Sommer et al. "Biomechanical properties and microstructure of human ventricular myocardium". In: *Acta biomaterialia* 24 (2015), pp. 172–192.

[70] Adrián Buganza Tepole et al. "Growing skin: a computational model for skin expansion in reconstructive surgery". In: *Journal of the Mechanics and Physics of Solids* 59.10 (2011), pp. 2177–2190.

[71] Thoracic Key. *Cardiac Anatomy and Electrophysiology | Thoracic Key*. URL: https://thoracickey.com/cardiac-anatomy-and-electrophysiology/ (visited on 07/05/2018).

[72] T P Usyk, R Mazhari, and A D Mcculloch. *Effect of Laminar Orthotropic Myofiber Architecture on Regional Stress and Strain in the Canine Left Ventricle*. Tech. rep. 2000, pp. 143–164.

[73] Taras P. Usyk, Ian J. LeGrice, and Andrew D. McCulloch. "Computational model of three-dimensional cardiac electromechanics". In: *Computing and Visualization in Science* 4.4 (2002), pp. 249–257. ISSN: 14330369.

[74] Rebecca Vandiver and Alain Goriely. "Differential growth and residual stress in cylindrical elastic structures". In: *Philosophical Transactions of the Royal Society of London A: Mathematical, Physical and Engineering Sciences* 367.1902 (2009), pp. 3607–3630.

[75] K. C. Vinnakota. "Myocardial density and composition: a basis for calculating intracellular metabolite concentrations". In: *AJP: Heart and Circulatory Physiology* 286.5 (2004), H1742–H1749. ISSN: 0363-6135.

[76] Wolfram Voelker et al. "Comparison of valvular resistance, stroke work loss, and Gorlin valve area for quantification of aortic stenosis: an in vitro study in a pulsatile aortic flow model". In: *Circulation* 91.4 (1995), pp. 1196–1204.

[77] R. N. Vossoughi J. Vaishnav and D. J. Patel. In: *Advances in Bioengineering* (1980). ISSN: 14330369.

[78] Wolfgang A. Wall et al. "Towards a comprehensive computational model for the respiratory system". In: *International Journal for Numerical Methods in Biomedical Engineering* 26.7 (2010), pp. 807–827. ISSN: 20407939. arXiv: NIHMS150003.

[79] Renae Waters et al. "Stem cell-inspired secretome-rich injectable hydrogel to repair injured cardiac tissue". In: *Acta Biomaterialia* 69 (2018), pp. 95–106. ISSN: 18787568.

[80] Daniel Werner. " Dortmund Technische Universit, At Two Scale Multi-component and Multi-phase Model for the Numerical Simulation of Biological Growth Processes in Saturated Porous Media - at the Example of Fatty Liver in Human". In: (2013).

[81] Daniel Werner, Tim Ricken, and Anne Ferreira Pfeiffer. "On a FEM model for isotropic and transversely isotropic growth in biphasic materials". In: *PAMM* 13.1 (2013), pp. 63–64. ISSN: 16177061.

[82] Nico Westerhof, Jan-Willem Lankhaar, and Berend E Westerhof. "The arterial windkessel". In: *Medical & biological engineering & computing* 47.2 (2009), pp. 131–141.

[83] Nicolaas Westerhof, GIJS Elzinga, and Pieter Sipkema. "An artificial arterial system for pumping hearts." In: *Journal of applied physiology* 31.5 (1971), pp. 776–781.

[84] Jonathan Wong and Ellen Kuhl. "Generating fibre orientation maps in human heart models using Poisson interpolation". In: *Computer Methods in Biomechanics and Biomedical Engineering* 17.11 (2014), pp. 1217–1226. ISSN: 1025-5842.

[85] Zhiye Wu et al. "Treatment of Myocardial Infarction with Gene-modified Mesenchymal Stem Cells in a Small Molecular Hydrogel". In: *Scientific Reports* 7.1 (2017), p. 15826. ISSN: 20452322.

[86] F. C. Yin, C. C. Chan, and R. M. Judd. "Compressibility of perfused passive myocardium". In: *American Journal of Physiology-Heart and Circulatory Physiology* 271.5 (1996), H1864–H1870. ISSN: 0363-6135.

[87] Yaohan Yu et al. "Evaluation of left ventricular strain in patients with dilated cardiomyopathy". In: *Journal of International Medical Research* 45.6 (2017), pp. 2092–2100. ISSN: 14732300.

[88] Douglas P Zipes et al. *Braunwald's Heart Disease E-Book: A Textbook of Cardiovascular Medicine*. Elsevier Health Sciences, 2018.

[89] Alexander M Zöllner et al. "Stretching skeletal muscle: chronic muscle lengthening through sarcomerogenesis". In: *PloS one* 7.10 (2012), e45661.